ABSTRACT

Nonlinear Responses in Dusty Plasmas

Zhiyue Ding, Ph.D.

Advisor: Truell W. Hyde, Ph.D.

Dusty plasma as a system containing both plasmas and dust particles. Dusty plasma systems are found throught out the industy and the space, for example, dust are found in plasma etching and in TOKAMAKs, as well as Saturn rings. Thus, the study of dusty plasma helps to understand many systems in reality. In this dissertation, the interaction of dust particles in a plasma sheath has been studied to determined the nature of the non-linear interaction. Theoretical model for describing the nonlinear dust interaction has been established and used to explain experimental observations. This dissertation is arranged in the following way. In chapter one, a background introduction of dusty plasmas is provided. In chapter two, a theoretical model describing the motion of two coupled dust particles considering nonlinear particle-particle interaction is established, and a perturbation method is used to analytically solve this model. In chapter three, experiments measuring amplitude-frequency responses are introduced and the nonlinear interaction is studied based on the model established in chapter two. In chapter four, the model established in chapter two is extended to a higher degree of freedom, which explains the 'internal resonance' that is observed for the first time in dusty plasma. In chapter five,

a Bayesian optimization-based automatic method for response analysis of a single dust particle is proposed. In chapter six, a quick estimation method is proposed for measuring the charge of dust particles in the plasma sheath.

Nonlinear Responses in Dusty Plasmas

by

Zhiyue Ding, B.S.

A Dissertation

Approved by the Department of Physics

Dwight P. Russell, Ph.D., Interim Chairperson

Submitted to the Graduate Faculty of
Baylor University in Partial Fulfillment of the
Requirements for the Degree
of
Doctor of Philosophy

Approved by the Dissertation Committee

Truell W. Hyde, Ph.D., Chairperson

Lorin S. Matthews, Ph.D.

Anzhong Wang, Ph.D.

Gerald B. Cleaver, Ph.D.

Tim Sheng, Ph.D.

Accepted by the Graduate School
December 2020

J. Larry Lyon, Ph.D., Dean

Page bearing signatures is kept on file in the Graduate School.

TABLE OF CONTENTS

LIST OF FIGURES

ACKNOWLEDGMENTS

First of all, I would like to thank my mentor Dr. Truell W. Hyde. I am grateful for his constant guidance and encouragement. I appreciate the flexible reasearch environment he provided and all his support during my stay at Baylor.

Next, I would like thank Dr. Ke Qiao, Dr. Jay Kong, Dr. Lorin S. Matthews and Dr. Truell W. Hyde for kind discussions and comments on my research.

I am also very grateful to Dr. Truell W. Hyde, Dr. Lorin S. Matthews, Dr. Anzhong Wang, Dr. Gerald B. Cleaver and Dr. Tim Sheng for serving on my committee.

Thanks to the faculty and staff in the physics department at Baylor who create such a convenient and friendly environment for the graduate students pursuing their PhDs.

Thanks to my friends: Yadan(Grace) Zheng, Yanbin Deng, Winwen Wang, Baofei Li, Mudi Chen, Jorge Carmona Reyes, Jens Schmidt, Graeson Griffin, Bo Zhang, Xiang Zhao and Bowen Li. I appreciate them for their company (even though many of them have already left Baylor) and I really had a very enjoyable time at Baylor with all my friends (we did a lot of funny and stupid things together).

Special thanks to Ke Qiao and Jay Kong. Ke Qiao always brings me to Penland for lunch. Jay Kong always invites me to his home offering his delicious homemade foods. Special thanks to Yanbin Deng and Xinwen Wang. They helped me a lot adapting to a new city the first year I came to Baylor. Special thanks to Yadan (Grace) Zheng for her support on my way to pursue my PhD. During the past years, we have travelled and visited a lot of different places together, and I really enjoy my time with her.

Support from NSF 1740203 is also acknowledged.

To My Parents

I would like to thank you for your love and support through all my life. You were the one who enlightened me on scienctific topics during my childhood and provided me with good educational support and guidance when I grew up. Also, I appreciate that you respected my decision of pursuing a PhD from Baylor University. In spite of the huge difference in time zones, we were continously Skyping over the past seven years. Our communication constantly encouraged me. It is your support and encouragment that allowed me to achieve what I have achieved so far. Lastly, I'm sorry that I let you worry during the this pandemic period. I promise that I'll cook at home as much as possible and avoid eating out.

CHAPTER ONE

Introduction to Dusty Plasmas

Complex plasmas are systems that contain both weakly ionized gas (plasma) and charged micron-sized particles (dust). The name 'complex plasmas' comes from analogy to 'complex liquids', i.e., the class of soft matter systems in liquid form. Complex plasmas have received significant attention since the 1990's when the crystallization of micron-sized particles was observed in a weakly ionized plasma. Thomas *et al.* [5] observed a hexagonal crystal structure of 7 μm melamine formaldehyde (MF) dust particles levitating in a weakly ionized radio frequency (RF) discharged argon plasma. At the same time, Chu *et al.* [6] reported the observation of face centered cubic (FCC), body centered cubic (BCC), as well as hexagonal structures of SiO_2 particles of 10 μm diameter in a similar RF argon discharge, with stable structure achieved by controlling the plasma conditions such as the rf power.

As the dominant component in the system of a complex plasma in terms of the energy and momentum transport, micron-sized dust particles can self-assemble to form gaseous, liquid and solid states, analogous to the properties of matter. As such, complex plasmas are sometimes regarded as a 'soft matter', a term that was first introduced by Pierre-Gilles de Gennes [7] to refer to a class of systems that can be structurally altered by thermal or mechanical stress. Complex plasmas satisfy all the criteria of a 'soft matter' in that they exhibit macroscopic softness, have metastable states, and have an equilibrium structure depending on external conditions [8]. In this case, complex plasmas are good platforms to study the behaviors of soft matter, due to the fact that the size of the dust particles are in the optically visible region and characteristic dynamical time scales are on the order of milliseconds. Such long time scales allow the study of dust particles in a complex plasma to be carried out to the fully resolved kinetic level. This makes complex plasma also suitable for research on fundamental dynamic phenomena, e.g., linear and nonlinear dynamics, and self-assembling dynamics, since micron-sized dust particles are strongly coupled to each other.

1.1 Charging Process

Micron-sized dust particles immersed in plasmas will become negatively charged (in the absence of emission processes). This is an important and fundamental process in complex plasmas since the interaction of the dust particles is mainly determined by the charge of the dust particles. In a gaseous discharge plasma, electrons have a larger thermal velocity than the ions. In a typical laboratory complex plasma environment (e.g., in a Gaseous Electronics Conference (GEC) RF reference cell) the electron temperature T_e is in a range between 3 eV to 6 eV, which is two orders of magnitude larger than the ion temperature T_i. As such, when an initially uncharged micron-sized particle is placed into a plasma, there will be more electrons than ions colliding with the surface of the dust particle, resulting in an excessive electron flux to the particle surface. As such, negative charges start to be accumulated on the surface of the dust particle and as the dust particle becomes negatively charged, electrons tend to be repelled while ions are attracted to the particle surface. This will finally lead to a stochastic balance between the electron flux and ion flux, in which case the charge on the dust particle reaches an equilibrium state.

One of the most widely used theoretical models to describe and calculate the charge of dust particles in plasmas is the Orbit Motion Limited (OML) approximation [9,10]. In OML theory, there is a pre-assumption that the dust particle size is much smaller than the Debye length (i.e., the scale over which mobile charge carriers screen out electric fields), and the Debye length is much smaller than both the collisional mean free path between the neutral atoms and the electrons, and the collisional mean free path between the neutral atom and the ions, i.e., $a \ll \lambda_D \ll \lambda_{mean}$ [11] where a is the radius of the dust particles, λ_D is the Debye length and λ_{mean} is the collisional mean free path. This assumption indicates two facts. The first is that each dust particle can be considered as isolated such that the electron and ion fluxes near the particle's surface are not disturbed by the other dust particles. The second fact is that the plasma considered in the OML theory is a collisionless plasma where the electrons and ions do not experience any collisions before they collide with the dust particle surface. Another assumption is that any possible effective potential barrier existing for ions in a negative central potential field is ignored to simplify the model [3]. Even though this potential barrier for ions exists in most dusty plasma situations, it has a small effect (or is negligible) when the dust particle size is small compared to the Debye length, i.e., $\frac{a}{\lambda_D} \to 0$.

Consider an electron moving in the central potential field $\phi(r)$ ($\phi(r) < 0$) of a dust particle with an initial velocity v (the velocity infinitely far away from the dust particle). The energy of the electron is conserved, which can be expanded by

$$E = \frac{1}{2} m_e v^2 = \frac{1}{2} m_e (v_r^2 + v_\theta^2) - e\phi(r), \tag{1.1}$$

where m_e is the mass of the electron, v_r is the radial velocity and v_θ is the angular velocity, r is the radial distance of electron away from the dust particle and e is the positive elementary charge. The conservation of angular momentum requires $m_e v_\theta r = m_e v p$ where p is the impact parameter. As such, Eq. 1.1 becomes

$$\frac{1}{2} m_e v^2 = \frac{1}{2} m_e [v_r^2 + \frac{(pv)^2}{r^2}] - e\phi(r), \tag{1.2}$$

By dividing both sides of Eq. 1.2 by $\frac{1}{2} m_e v^2$, Eq. 1.2 becomes

$$1 = \frac{v_r^2}{v^2} + \frac{p^2}{r^2} - \frac{2e\phi(r)}{m_e v^2}. \tag{1.3}$$

From Eq. 1.3, an electron's motion is restricted to an area where the effective potential

$$\phi_{eff} = \frac{p^2}{r^2} - \frac{2e\phi(r)}{m_e v^2} \tag{1.4}$$

is less than or equal to 1, i.e., $\phi_{eff} \leq 1$. Electrons which have a radial distance less than or equal to the radius of the dust particle where they have zero radial velocity, can be collected by the dust particle and contribute to the accumulated charge. As such, the cross section for electron collection is

$$\sigma(v) = \pi p_{max}^2 = \pi a^2[1 + \frac{2e\phi(a)}{m_e v^2}], \tag{1.5}$$

where p_{max} is the maximum distance (maximum impact factor) from which electrons can be collected by the dust particle. With the cross section determined, the electron flux to the dust particle can be derived as

$$I_e = -en_e \int \sigma(v) v f(v) d^3v, \tag{1.6}$$

where n_e is the electron number density, and $f(v)$ is the electron velocity distribution function. Considering a Maxwellian velocity distribution for electrons in plasma, Eq. 1.6 becomes

$$I_e = -en_e \int \pi a^2[1 + \frac{2e\phi(a)}{m_e v^2}] \frac{v e^{-\frac{v^2}{2v_{T_e}^2}}}{\sqrt{(2\pi v_{T_e}^2)^3}} d^3v, \tag{1.7}$$

where $v_{T_e} = \sqrt{\frac{T_e}{m_e}}$ is the electron thermal velocity. By integrating Eq. 1.7, the electron flux colliding onto the dust particle can be approximated as

$$I_e = -e\sqrt{8\pi} n_e v_{T_e} e^{\frac{e\phi(a)}{T_e}}. \tag{1.8}$$

On the other hand, ions moving in the central field potential $\phi(r)$ of a dust particle experience an attractive potential energy $e\phi(r)$. For an attractive potential (i.e., $e\phi(r) < 0$), there is the possibility that there could be a potential barrier that reflects the ions. For a repulsive potential, the potential energy has the constraint $\frac{2e\phi(a)}{m_e v^2} \geq -1$ (see Eq. 1.5) to ensure a positive impact parameter. However, this constraint is not necessary for an attractive potential in that the impact factor is always positive, independent of the value of the dust particle surface potential $\phi(a)$. In this case, it is possible that the surface potential $\phi(a)$ can take values making the effective potential $\phi_{effect} > 1$ which results in a potential barrier, reflecting some ions. Lampe et al [12] studied the effect of this potential barrier for ions in a central Yukawa potential field and pointed out that the OML assumption of the absence of a potential barrier is valid for small dust particles $\frac{a}{\lambda_D} << 1$. In this case, the cross section for ions collected by the dust particle is

$$\sigma(v) = \pi p_{max}^2 = \pi a^2 (1 - \frac{2Ze\phi(a)}{m_i v^2}), \tag{1.9}$$

where Z is the ion charge number and m_i is the mass of ion. Correspondingly, the ion flux to the dust particle assuming a Maxwellian velocity distribution for the ions yields

$$I_i = Zen_i \int \pi a^2 (1 - \frac{2Ze\phi(a)}{m_i v^2}) \frac{ve^{(-\frac{v^2}{2v_{T_i}^2})}}{\sqrt{(2\pi v_{T_i}^2)^3}} d^3v, \tag{1.10}$$

where n_i is the ion number density and $v_{T_i} = \sqrt{\frac{T_i}{m_i}}$ is the ion thermal velocity. By integrating Eq. 1.10 and keeping the first two terms in the Taylor expansion of the surface potential, the ion flux can be approximated as

$$I_i = Ze\sqrt{8\pi} a^2 n_i v_{T_i} (1 - \frac{Ze\phi(a)}{T_i}). \tag{1.11}$$

The total charge accumulated on the dust particle can be estimated at a stationary state where the total electron and ion flux colliding onto the dust particle is zero,

$$I_i + I_e = 0, \tag{1.12}$$

allowing the surface potential of the dust particle $\phi(a)$ to be calculated. The dust particle charge can be estimated (assuming the dust is a spherical capacitor) as $Q_0 = a\phi(a)$. Meanwhile, the charge fluctuation on the dust particle is governed by

$$\dot{Q} = I_i + I_e. \tag{1.13}$$

By defining the charging frequency $\Omega_{ch} = -\frac{d(I_i+I_e)}{dQ}|_{Q_0}$ as the relaxation frequency for small deviations of the charge from the stationary value [8], this inverse charging time can be calculated as

$$\Omega_{ch} = \frac{(1 + \frac{Qe}{aT_e})a}{\sqrt{2\pi}\lambda_{Di}}\Omega_{pi}, \tag{1.14}$$

where $\lambda_{Di} = \sqrt{\frac{T_i}{4\pi e^2 n_i}}$ is the Debye length for ions and $\Omega_{pi} = \frac{v_{T_i}}{\lambda_{Di}}$ is the ion plasma frequency. The charging process (i.e., the accumulated charge on the dust particle surface as a function of charging time) can be characterized by the solution to Eq. 1.13. As an example, the charging process in an argon discharge with an electron-ion temperature ratio $\frac{T_e}{T_i} = 50$ is plotted in Fig. 1.1 [1], where the y-axis is the

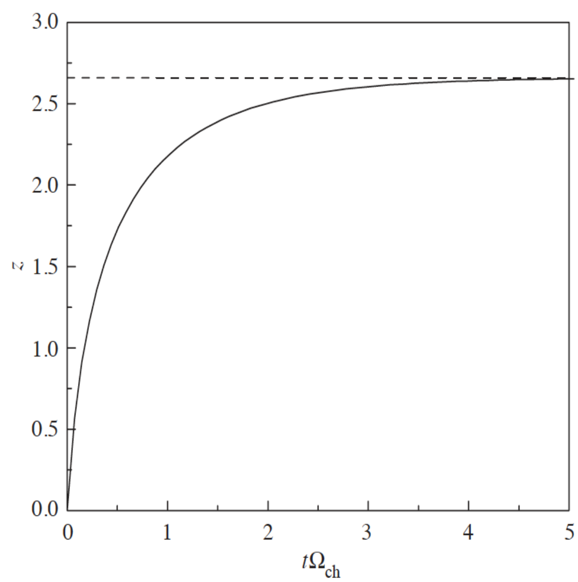

Figure 1.1: The particle is initially uncharged. The horizontal dashed line corresponds to the stationary value of the charge [1].

dimensionless charge $z = \frac{|Qe|}{aT_e}$ and the x-axis is the dimensionless time $t\Omega_{ch}$.

In the OML approximation, the surface potential of the dust particle is found to be determined by two main factors. The first is the electron-ion temperature ratio $\frac{T_e}{T_i}$. Usually this electron-ion temperature ratio in a laboratory GEC rf reference cell is on the order of 10^2. The second factor is the electron-ion mass ratio $\frac{m_e}{m_i}$. This factor is determined by the type of gas and has a magnitude on the order of 10^{-4}. Fig. 1.2 [1] shows the dimensionless stationary charge on dust particles $z = \frac{|Qe|}{aT_e}$ as a function of

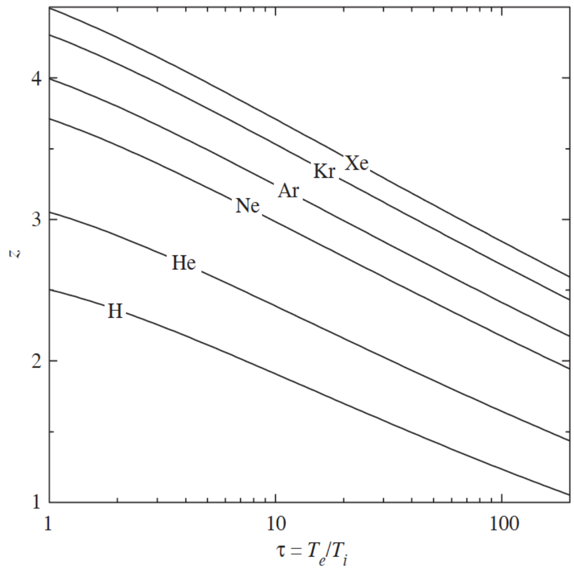

Figure 1.2: Dimensionless charge $z = \frac{|Qe|}{aT_e}$ of an isolated spherical particle as a function of electron-to-ion temperature ratio for isotropic plasmas of different gases. [1].

the electron-ion temperature ratio $\frac{T_e}{T_i}$ for different types of gas discharge. As shown, the dust charge has a negative correlation to the electron-ion temperature ratio $\frac{T_e}{T_i}$ but a positive correlation to the ion-electron mass ratio $\frac{m_i}{m_e}$.

In addition to the collection of electrons and ions from a plasma, there are also other possible charging mechanisms for dust grains. For example, excessive electrons can be emitted from the dust particle surface due to thermionic, photoelectric, and secondary electron emission processes. There processes can result in positively charged grains. Studies of these charging mechanisms can be found in [11, 13–19].

In anisotropic plasmas, the motion of electrons and ions are subject to forces due to other electromagnetic fields. For example, in a plasma generated in a laboratory GEC RF reference cell, the electrons and ions are accelerated in the sheath electric field. This will change the charging mechanism since electrons and ions are now drifting relative to the dust particles. Usually, due to the electrons' high thermal speed, the electron drift relative to the dust particles is negligible. However, the ion drift cannot be ignored. To account for the effect of the ion drift, an appropriate ion velocity distribution is required to be used in Eq. 1.10 to find the total ion flux, for example, a shifted Maxwellian velocity distribution $\frac{1}{\sqrt{(2\pi v_{T_i}^2)^3}} e^{-\frac{(\mathbf{v}-\mathbf{v}')^2}{2v_{T_i}^2}}$ where **v**' is the drift speed for ions. In a GEC RF reference cell, the charge on dust particles levitated in the plasma sheath is estimated to be $Q \approx 10^3 e - 10^4 e$, depending on the plasma pressure and power. A simple method to experimentally estimate the charge on a dust particle levitated in the sheath of a GEC RF reference cell is described in chapter five.

1.2 Plasma Sheath

In a laboratory GEC RF reference cell, the operating gas is discharged between two electrodes. Similar charging effects cause any plasma facing surface to be negatively charged, thus electrodes in a GEC RF reference cell will also be negatively charged due to excessive electron collisions. As the electron density decreases when approaching an electrode (or absorbing wall), a positive space charge region is generated in front of each electrode. This positive space charge region connecting the plasma bulk and an electrode (or absorbing wall) is known as the plasma sheath.

To investigate the formation of the plasma sheath (assuming a one dimensional sheath), the following dimensionless quantities are introduced [2]

$$\begin{aligned} y &= \frac{m_i v_z^2}{2kT_e}, \\ \chi &= -\frac{e\phi}{kT_e}, \\ n_{e,i} &= \frac{N_{e,i}}{N_0}, \\ \xi &= \frac{z}{\lambda_D}, \end{aligned} \tag{1.15}$$

where y represents the kinetic energy of an ion $\frac{m_i v_z^2}{2}$ at a distance z from the absorbing wall, normalized to the electron thermal energy kT_e, χ is the ion potential energy $e\phi$ normalized to the electron thermal energy, N_e and N_i are respectively the electron and ion densities inside the plasma sheath normalized by the density of the plasma bulk N_0, and ξ is the distance z from the absorbing wall normalized by the Debye length. With these quantities defined, the plasma sheath can be described by the following four conditions:

1) conservation of ion number

$$n_i\sqrt{y} = \sqrt{y_0}, \tag{1.16}$$

where y_0 is the normalized ion kinetic energy at the sheath edge (the interface between the plasma bulk region and the plasma sheath region).

2) conservation of energy for ions

$$y = y_0 + \chi, \tag{1.17}$$

3) electrons are assumed to follow the Maxwellian-Boltzmann distribution

$$n_e = e^{-\chi}, \tag{1.18}$$

and 4) Poisson's equation

$$\frac{d^2\chi}{d\xi^2} = n_i - n_e. \tag{1.19}$$

Combining Eq. 1.16 and Eq. 1.17, the ion density in the plasma sheath can be expressed as

$$n_i = (1 + \frac{\chi}{y_0})^{-\frac{1}{2}}. \tag{1.20}$$

Substituting Eq. 1.18 and Eq. 1.20 into Eq. 1.19, Poisson's equation now becomes

$$\frac{d^2\chi}{d\xi^2} = (1 + \frac{\chi}{y_0})^{-\frac{1}{2}} - e^{-\chi}. \tag{1.21}$$

This second order ODE can be reduced to a first order ODE by multiplying by $\frac{d\chi}{d\xi}$ and then integrating

$$\int_{-\infty}^{0} \frac{d\chi}{d\xi}\frac{d^2\chi}{d\xi^2}d\xi = \int_{-\infty}^{0}[(1 + \frac{\chi}{y_0})^{-\frac{1}{2}} - e^{-\chi}]\frac{d\chi}{d\xi}d\xi. \tag{1.22}$$

which yields

$$\frac{1}{2}(\frac{d\chi}{d\xi})^2 - \frac{1}{2}(\frac{d\chi}{d\xi})^2|_{-\infty} = 2y_0\sqrt{1+\frac{\chi}{y_0}} - 2y_0\sqrt{1+\frac{\chi}{y_0}}|_{-\infty} + e^{-\chi} - e^{-\chi}|_{-\infty}. \quad (1.23)$$

Considering the boundary conditions $\chi = 0$ and $\frac{d\chi}{d\xi} = 0$ in the plasma bulk where $\xi = -\infty$, Poisson's equation Eq. 1.19 can now be reduced to

$$(\frac{d\chi}{d\xi})^2 = 4y_0\sqrt{1+\frac{\chi}{y_0}} - 4y_0 + 2e^{-\chi} - 2, \quad (1.24)$$

which needs to be solved numerically. Using a Taylor expansion of the right hand side of Eq. 1.24 with respect to the normalized potential χ, one finds that at the sheath edge, $\chi = 0$. Eq. 1.24 can then be expanded as

$$(\frac{d\chi}{d\xi})^2 = (1 - \frac{1}{2y_0})\chi^2 + o(\chi^3), \quad (1.25)$$

which gives the criteria for the formation of the plasma sheath. The plasma sheath can only be formed if $(1 - \frac{1}{2y_0})$ is non-negative (or $y_0 \geq \frac{1}{2}$), otherwise, Eq. 1.24 will result in a potential of imaginary value which has no physical meaning. This criteria means that in order to form a plasma sheath, the ion velocity at the sheath edge has to be greater than a threshold velocity

$$v_0 \geq \sqrt{\frac{kT_e}{m_i}}, \quad (1.26)$$

known as the 'Bohm velocity' [20].

The criteria for a sheath formation Eq. 1.26 raises another point. In the plasma bulk, the thermal energy of electrons is usually much larger than the thermal energy of ions, as the electron temperature is much larger than the ion temperature $T_e \gg T_i$. In order for the ions in the bulk to be accelerated to the Bohm velocity there should exist a transition region where an electric field exists. At the same time, the transition region should conserve the property of the plasma bulk, in that this region is charge neutral, i.e., $n_e \approx n_i$, otherwise, this region would have no difference from the plasma sheath. This transition region where ions are accelerated to the Bohm velocity is called the 'pre-sheath' [21].

To study the mechanism which accelerates the ions in pre-sheath, an extension scale L is introduced according to Riemann [2] as $L \gg \lambda_D = \epsilon L$ where ϵ is a smallness parameter, and the pre-sheath mechanism will be studied at the scale of L, or $\epsilon\xi$, as

$$x = \frac{z}{L} = \epsilon\xi, \tag{1.27}$$

while the sheath mechanism is considered at the scale of ξ. As such, the potential in the pre-sheath region can be described by Poisson's equation as

$$\epsilon^2 \frac{d^2\chi}{dx^2} = n_i(\chi, x) - n_e(\chi). \tag{1.28}$$

It can be seen from Eq. 1.28 that at the asymptotic limit where $\epsilon \to 0$, the right hand side of Eq. 1.28 also goes to zero indicating the quasi-neutrality of the pre-sheath, i.e., $n_e \approx n_i$. Fig. 1.3 (from Riemann [2]) shows the potential χ as a function of distance from the absorbing wall at different length scales. As shown, for small but finite ϵ (Fig. 1.3a), the potential χ is flat at distances far away from the absorbing wall (pre-sheath region) and it becomes steeper as the distance approaches the absorbing wall (sheath region). In the asymptotic limit that ϵ goes to 0, the pre-sheath scale has to be distinguished from the sheath scale. Fig. 1.3b shows the potential χ on the pre-sheath scale where the sheath region is squeezed into an infinitely thin layer, while on the sheath scale (Fig. 1.3c), the pre-sheath is treated as infinitely remote [2]. Based on the quasi-neutral property of the plasma pre-sheath, the mechanism of the pre-sheath formation can be discussed. The quasi-neutral property $n_i = n_e$ results in the condition

$$\frac{j_i}{\sqrt{y}} = e^{\chi}, \tag{1.29}$$

where $j_i = \sqrt{(\frac{m_i}{2kT_e})}\frac{J_i}{N_0}$ is the ion current. By take the logarithm and differentiating both sides of Eq. 1.29 with respect to spacial displacement x, this yields

$$\frac{1}{2y}\frac{dy}{dx} - \frac{d\chi}{dx} = \frac{1}{j_i}\frac{dj_i}{dx}. \tag{1.30}$$

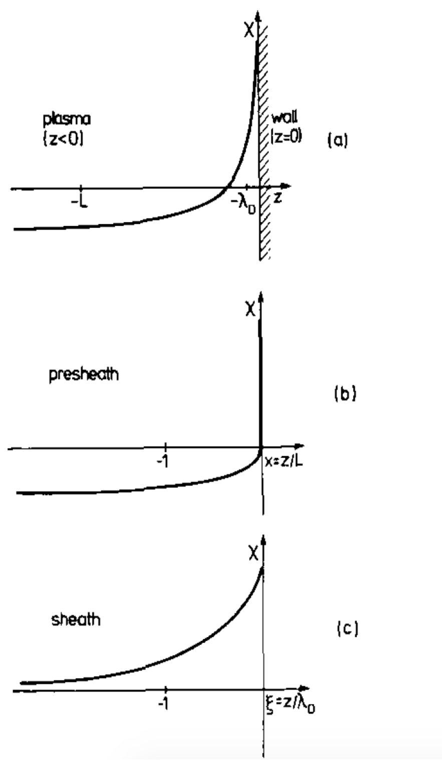

Figure 1.3: Potential variation in front of a negatively charged absorbing wall at a) small but finite ϵ; b) pre-sheath scale at asymptotic limit as ϵ goes to 0; c) sheath scale at asymptotic limit as ϵ goes to 0 [2].

Since we know that the pre-sheath is the region where ions are accelerated to the Bohm velocity, the ion velocity in the pre-sheath region must be less than the Bohm velocity, i.e., $v_0 < \sqrt{\frac{kT_e}{m_i}}$ or $y < \frac{1}{2}$. As such, Eq. 1.30 can be expressed by the following inequality

$$\frac{dy}{dx} - \frac{d\chi}{dx} < \frac{1}{j_i}\frac{dj_i}{dx}, \tag{1.31}$$

which means that the ions can be accelerated to the Bohm velocity in any of the following situations:

1) The ion current density increases approaching the absorbing wall, $\frac{dj_i}{dx} > 0$.

2) The energy of ions is dissipated in the pre-sheath $\frac{dy}{dx} < \frac{d\chi}{dx}$.

3) A combination of both of the previous conditions listed above.

Thus, according to Riemann, the pre-sheath can be divided into the follow categories based on its formation mechanisms:

a) Geometric pre-sheath with current concentration $\frac{dj_i}{dx} > 0$ where the extension scale L is the curvature radius.

b) Collisional pre-sheath with ion friction where $\frac{dy}{dx} < \frac{d\chi}{dx}$ and the extension scale L is the ion mean free path.

c) Ionizing pre-sheath with current increase $\frac{dj_i}{dx} > 0$ and mean ion retardation $\frac{dy}{dx} < \frac{d\chi}{dx}$ where the extension scale L is the ionization length.

Besides these pre-sheath mechanisms, there is another type of per-sheath mentioned by Riemann

d) The magnetic pre-sheath where kinetic energy y perpendicular to the absorbing wall is converted into parallel kinetic energy. In this case, the extension scale L is the ion gyro-radius.

Due to the difference of the electron and ion densities, the potential is not constant in the plasma sheath region, which means an electric field exists in the plasma sheath region. In a laboratory GEC RF reference cell, this electric field provides negatively charged dust particles with an upward electrostatic force to balance gravity. As such, dust particles can levitate in the plasma sheath region in GEC RF reference cells. Therefore, it is natural and necessary for us to understand how dust particles interact with each other inside the plasma sheath region.

1.3 Dust Particle Interaction

In an isotropic plasma, the potential field around an isolated spherical dust particle is known to be a screened Coulomb or Yukawa potential $\phi(r) = \frac{Q}{4\pi\epsilon_0 r}e^{-\frac{r}{\lambda_D}}$ when the particle size is much smaller than the linearized Debye length, $\lambda_D^{-2} = \lambda_{Di}^{-2} + \lambda_{De}^{-2}$, and electrons and ions around the dust particle are assumed to obey a Maxwellian-Boltzmann distribution.

On the other hand, as in an anisotropic plasma, dust particles in a GEC RF reference cell are levitated in plasma sheath region where ion flow exists. As it passes a dust particle, the ion flow is altered by the charged dust and ions are concentrated in a region downstream of the dust particle. This perturbation of the ion stream density is known as the wake effect and the region where ions re-concentrated is called the ion focus. Fig. 1.4 shows a sketch of the ion wake effect where the positive charged region downstream the dust particle is the ion focusing. Even though there is not yet a deterministic conclusion about the exact location of the ion focus, this location is found to be dependent on many parameters, such as the velocity of the ion flow, the electron to ion temperature ratio, and the size of the grain [22].

Based on linear response theory, the electrostatic potential around a dust particle in ion flow is determined by

$$\phi(\mathbf{r}) = \int \frac{Q}{8\pi^3\epsilon_0 k^2 \epsilon(\mathbf{k}, \omega - k_z v_i)} e^{i\mathbf{k}\cdot\mathbf{r}} d\mathbf{k}, \tag{1.32}$$

where $\mathbf{k}$ with $k = |\mathbf{k}|$ is the wave number vector of the ion acoustic wave, $\epsilon(\mathbf{k}, \omega - k_z v_i)$ is the anisotropic plasma permittivity with respect to a Doppler shifted frequency $\omega - k_z v_i$. Here k_z is the wave number along the direction of the ion flow and v_i is the velocity of the ion flow. With different assumptions for the permittivity of the

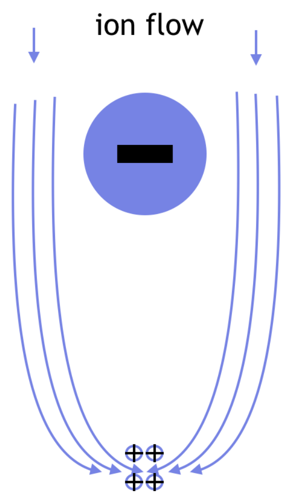

Figure 1.4. Sketch for ions streaming around a dust particle.

anisotropic plasma $\epsilon(\mathbf{k}, \omega - k_z v_i)$, the electrostatic potential yields different forms. For example, based on Vladimirov and Nambu's model [23], the anisotropic plasma permittivity takes the form

$$\frac{1}{\epsilon(\mathbf{k}, \omega - k_z v_i)} = \frac{k^2\lambda_{De}^2}{1 + k^2\lambda_{De}^2} + \frac{k^2\lambda_{De}^2\omega_s^2}{(1 + k^2\lambda_{De}^2)[(\omega - k_z V_i)^2 - \omega_s^2]}, \tag{1.33}$$

where $\omega_s = \frac{kv_B}{\sqrt{1+k^2\lambda_{De}^2}}$ is the frequency of the ion flow oscillation with v_B being the Bohm velocity. The first term in the right hand side of Eq. 1.33 corresponds to the permittivity of the Yukawa potential $\frac{1}{\epsilon(\mathbf{k},\omega)} = \frac{k^2\lambda_{De}^2}{1+k^2\lambda_{De}^2}$. By applying Eq. 1.33 into Eq. 1.32, the electrostatic potential along the direction of the ion flow behind the dust particle is approximated as [23]:

$$\phi(r) = \frac{Q}{4\pi\epsilon_0 r} + \frac{2Qcos(r\lambda_{De}\sqrt{M^2 - 1})}{4\pi\epsilon_0 r(1 - M^{-2})}, \tag{1.34}$$

where $M = \frac{v_i}{v_B}$ is the mach number. Notice that this approximation was made under the assumption of supersonic ion flow $M > 1$. One important feature of the electrostatic potential (or wake potential) is that the potential oscillates behind the dust particle. As illustrated in Eq. 1.34, the second term in the right hand side is proportional to $cos(r\lambda_{De}\sqrt{M^2 - 1})$ which yields an oscillating property and there exists an attractive potential at positions where the electrostatic potential takes positive values.

This wake potential has also been profiled numerically. For example, Lampe *et al.* [3] derived a spatially resolved wake potential based on a more complicated anisotropic plasma permittivity as

$$\epsilon(\mathbf{k}, \omega - k_z v_i) = 1 + \frac{1}{k^2 \lambda_{De}^2} - \frac{\omega_p^2}{k^2} \int \frac{\mathbf{k} \partial f_{i0}(\mathbf{v}) / \partial \mathbf{v}}{k_z v_i - \omega - i v_{in}} d\mathbf{v}, \tag{1.35}$$

where $f_{i0}(\mathbf{v})$ is the shifted Maxwellian distribution function for ions which takes the form $f_{i0}(\mathbf{v}) = n_0(\frac{m_i}{2\pi T_i}) e^{\frac{m_i(\mathbf{v}-v_i)^2}{2T_i}}$. In this model, both ion-neutral collisions (with v_{in} the collision frequency) and Landau damping (in terms of the shifted Maxwellian distribution for ions) are considered. Fig. 1.5 shows the contour plot of this wake potential with a mach number $M = 1.5$ and the electron-ion temperature ratio $\frac{T_e}{T_i} =$ 25.

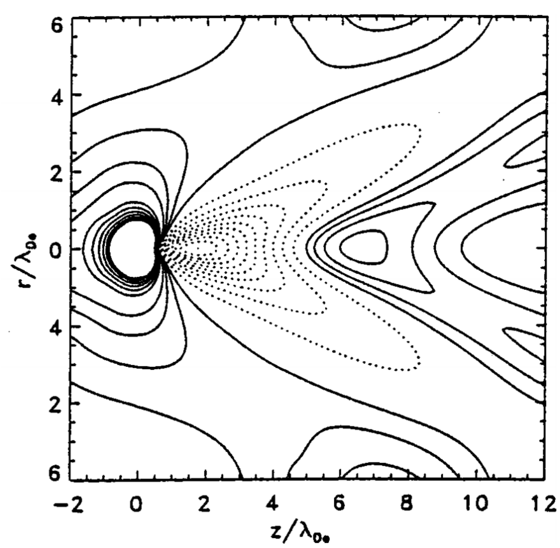

Figure 1.5: Potential contour of a negative dust grain in a plasma of flowing ion. The dust particle is at the origin. Solid and dashed curves indicate respectively negative and positive potential [3].

Again, an oscillating wake potential is predicted and a maximum attractive potential (positive potential) is observed at a position about two Debye lengths behind the dust particle.

In the situation that the ion velocity is subsonic $M < 1$, the electrostatic potential Eq. 1.32 can be derived within the Bhatnagar-Gross-Krook (BGK) approach for the ion-neutral collision integral [24, 25]. In the case of small collisionality (i.e., small ratio of the ion-neutral collision frequency to the ion plasma frequency) [8], the corresponding wake potential can be approximated as [26]

$$\phi(r,\theta) = Q[\frac{e^{-\frac{r}{\lambda_D}}}{r} - 2\sqrt{\frac{2}{\pi}}\frac{M\lambda_D^2}{r^3}cos\theta - (2-\frac{\pi}{2})\frac{M^2\lambda_D^2}{r^3}(3cos^2\theta - 1)] + o(\frac{M^2}{r^3}), \quad (1.36)$$

where θ is the angle between r and v_i. From Eq. 1.36, it can also be inferred that an attractive interaction is possible in a certain solid angle along the ion flow when the wake potential has a positive value.

Since the potential behind the dust particle in the presence of ion flow is perturbed by the wake effect, the particle-particle interaction becomes complicated when one of the dust particles is in the wake region (downstream region) of another dust particle. The particle-particle interaction also becomes non-reciprocal due to the wake effect, i.e., the interaction from the downstream particle to the upstream particle is not identical to the interaction from the upstream particle to the down stream particle. The downstream particle experiences a repulsive interaction from the upstream particle (for example, the part of the Yukawa repulsion in Eq. 1.34 and Eq. 1.36), but at the same time it also experiences a possible attractive interaction from the upstream particle (for example, at the position where the rest parts in Eq. 1.34 and Eq. 1.36 are positive). However, the upstream particle only feels the repulsion from the downstream particle, and it is hardly affected by the wake effect created by itself. This seems to be a violation of Newton's third law since the interaction is non-reciprocal when only considering the dust particles. To reconcile this contradiction, this system should be considered as an open system where the ion flow brings energy in [27]. For an open system, it is not necessary for Newton's third law to hold.

Due to this non-reciprocal interaction (mainly the attractive wake potential), dust particles can be formed into a self-aligned chain structure. The simplest example of a self-aligned chain structure is a chain that only involves two dust particles, i.e., a dust pair structure. Fig. 1.6 shows the 'Schweigert' model of the dust pair structure [4,27]. In this model, the effect of the wake potential has been modeled by a positively charged image particle located at the wake focal point (point charge model).

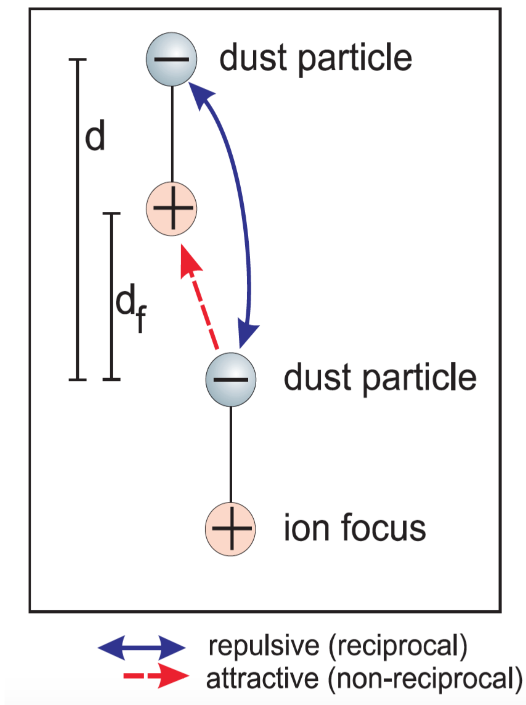

Figure 1.6: 'Schweigert' model for a dust pair with the wake effect modeled as an image positively charged point charge located downstream of a dust particle [4].

As shown, the downstream particle is repelled by the upstream particle (blue interaction) but attracted by the image point charge which represents the ion wake effect (red interaction).

The simplest way to study the particles' motion under this pair structure is to approximate the interaction linearly. Assuming that the interaction is a function of the particle-particle interspacing, the interaction along the direction of the ion flow can approximated by the linear term in the Taylor expansion of the exact interaction force which has the form of $k(x_1 - x_2)$ where x_1, x_2 are the displacements of the upstream and downstream particle away from the equilibrium position and k is the first derivative of the interaction force with respect to the inter-particle spacing. This assumption is valid in the point charge model because the position of the point charge moves with the upstream particle such that the interaction from the point charge to the downstream particle also depends on the particle-particle spacing, but only differs by a constant. The non-reciprocity in the particle-particle interaction can be illustrated by the difference in values k can take for upstream and downstream interactions. Carstensen *et al.* [28] measured the constant k for the linear interaction approximation from the resonance curves of particles' motion under small excitations and revealed the non-reciprocity through a parameter defined as the ratio of the linear constants for upstream and downstream interactions $\frac{k_{21}}{k_{12}}$. Based on the same model with a linear approximation of the interaction, Jung *et al.* [29] investigated the de-charging of the downstream particle in the ion wake by introducing a heavier downstream dust particle of a different material from the upstream dust particle. The heavier particles are made of different material so that plasma etching on these particles are different from those placed upstream, which allows a continues spacial probe of the downstream ion wake.

Even though this linear model of particle-particle interaction succeeds in revealing the non-reciprocal property of the particle-particle interaction under the influence of the ion wake, it fails to explain any phenomenon that takes place in the nonlinear regime, such as nonlinear mode coupling or internal resonance. In order to study the nonlinear behavior of dust particles in the plasma sheath, it is necessary to extend the linear interaction model to models including higher order nonlinearities.

CHAPTER TWO

Theory

As mentioned in chapter one, due to higher electron thermal velocity (resulting in a larger electron flux as compared to the ion flux to the particle surface), dust particles are in general negatively charged when located inside the plasma sheath region, or even the pre-sheath region. In both cases, ions are accelerated to the Bohm velocity ($v_B = \sqrt{\frac{kT_e}{m_i}}$, where k, T_e, m_i are the Boltzmann constant, electron temperature and ion mass respectively) satisfying the 'Bohm criterion' for the formation of the sheath [20, 30–32]. In the plasma sheath region of an absorbing wall, due to the electrostatic field produced by the accumulated electrons on the absorbing wall, the immersed dust particles will experience a repulsive electrostatic force. In a configuration where the absorbing wall is perpendicular to gravity, the electrostatic force experienced by the dust particle will then be balanced by gravity, in which case dust particles can be levitated inside the plasma sheath.

In the vicinity of the dust levitation position, the sheath potential can be approximated by a parabolic potential [33]. By ignoring the charge fluctuations induced by the variation of the particle levitation position, the dust particles can then be considered as being confined inside a parabolic potential well $\Phi = \frac{1}{2}m\omega^2 x^2$, where m, ω^2, and x are respectively the mass of the dust particle, the background confinement strength and the displacement of the dust particle from its levitation position.

For the case of two dust particles forming a pair structure aligned with the ion flow, and the particle-particle interaction becomes asymmetric due to the influence of the ion wake field formed behind the upstream dust particle [27, 34–38]. This is known as the non-reciprocal particle-particle interaction. One method for describing the dynamics of such a particle pair system is to model the paired dust particles as two coupled oscillators with non-identical coupling constants (in order to properly model the non-reciprocal particle-particle interaction) confined inside the plasma sheath.

2.1 A Linear System of Coupled Oscillators with Non-reciprocal Interaction

The simplest model of a particle pair system assumes a linear model of coupled oscillators. Considering a one dimensional situation where the coupled oscillators are restricted to move with only one degree of freedom (say in the x-direction), the linear model describing this system assuming a non-reciprocal particle-particle interaction is:

$$\begin{aligned} \ddot{x}_1 + \omega_1^2 x_1 + k_1(x_1 - x_2) = 0, \\ \ddot{x}_2 + \omega_2^2 x_2 + k_2(x_2 - x_1) = 0, \end{aligned} \tag{2.1}$$

where ω_1^2 and ω_2^2 are the background restoring confinements at the dust equilibrium levitation positions and k_1 and k_2 are the coupling constants normalized by the mass of the oscillators. Different from the case of a typical coupled oscillator, where the coupling constant is shared, k_1 and k_2 are not necessarily identical in order to properly represent the non-reciprocal particle-particle interaction. In this simplest system, damping from neutral drag is ignored and no external excitations are considered.

In order to derive the eigen-modes (as well as eigen-frequencies) of this system, one needs to calculate the determinant of the following dynamical matrix

$$\begin{bmatrix} -\omega_\pm^2 + \omega_1^2 + k_1, & -k_1 \\ -k_2, & -\omega_\pm^2 + \omega_2^2 + k_2 \end{bmatrix}.$$

By equating the determinant with zero, the eigen-frequencies are found to be

$$\begin{aligned} \omega_+^2 &= \frac{(\omega_1^2 + k_1 + \omega_2^2 + k_2) + \sqrt{(\omega_1^2 + k_1 - \omega_2^2 - k_2)^2 + 4k_1k_2}}{2}, \\ \omega_-^2 &= \frac{(\omega_1^2 + k_1 + \omega_2^2 + k_2) - \sqrt{(\omega_1^2 + k_1 - \omega_2^2 - k_2)^2 + 4k_1k_2}}{2}, \end{aligned} \tag{2.2}$$

and the ratio of the amplitude of the corresponding eigen-modes are:

$$\begin{aligned}(\frac{x_1}{x_2})_+ = \alpha_+ = \frac{k_1}{-\omega_+^2 + \omega_1^2 + k_1} = \frac{-\omega_+^2 + \omega_2^2 + k_2}{k_2},\\ (\frac{x_1}{x_2})_- = \alpha_- = \frac{k_1}{-\omega_-^2 + \omega_1^2 + k_1} = \frac{-\omega_-^2 + \omega_2^2 + k_2}{k_2}.\end{aligned} \tag{2.3}$$

Thus, the equations of motion (2.1) for this system can be decoupled as

$$\begin{aligned}\ddot{x}_+ + \omega_+^2 x_+ = 0,\\ \ddot{x}_- + \omega_-^2 x_- = 0,\end{aligned} \tag{2.4}$$

by introducing the eigen-mode basis

$$\begin{aligned}x_+ = x_1 - \alpha_- x_2,\\ x_- = x_1 - \alpha_+ x_2.\end{aligned} \tag{2.5}$$

2.2 Coupled Oscillators with Frictional Damping

Unfortunately, dust particles are rarely in a vacuum environment. As such, collisions with neutral gas particles provide an additional neutral drag force exerted on the dust particles, which makes it a damped system. Taking frictional damping (i.e., velocity dependent damping) into consideration, a system of coupled oscillators acting under a non-reciprocal interaction without external driving can be described as

$$\begin{aligned}\ddot{x}_1 + \mu\dot{x}_1 + \omega_1^2 x_1 + k_1(x_1 - x_2) = 0,\\ \ddot{x}_2 + \mu\dot{x}_2 + \omega_2^2 x_2 + k_2(x_2 - x_1) = 0,\end{aligned} \tag{2.6}$$

where μ is the damping coefficient. To solve this system, if one applying the same method used above before for the linear system (Eq. 2.1) (i.e., calculating the eigen-frequencies directly from the matrix of dynamics), a biquadratic determinant encountered and ω becomes a complex value. To avoid this complexity, the equations of motion described in Eq. 2.6 are instead approached using a linear eigen-basis. According to the transformation shown in Eq. 2.5, the equations of motion in the $x_\pm$ basis can be derived by subtracting ($\alpha_\mp\times$ Eq. 2.6b) from (Eq. 2.6a):

$$\begin{aligned}(\ddot{x}_1 - \alpha_-\ddot{x}_2) + \mu(\dot{x}_1 - \alpha_-\dot{x}_2) + (\omega_1^2 x_1 - \alpha_-\omega_2^2 x_2) + (k_1 + \alpha_- k_2)(x_1 - x_2) = 0,\\ (\ddot{x}_1 - \alpha_+\ddot{x}_2) + \mu(\dot{x}_1 - \alpha_+\dot{x}_2) + (\omega_1^2 x_1 - \alpha_+\omega_2^2 x_2) + (k_1 + \alpha_+ k_2)(x_1 - x_2) = 0.\end{aligned} \tag{2.7}$$

Allowing Eq. 2.5, the original coordinates x_1 and x_2 can now be represented by x_+ and x_- as:

$$\begin{aligned} x_1 =& \frac{\alpha_+ x_+ - \alpha_- x_-}{\alpha_+ - \alpha_-}, \\ x_2 =& \frac{x_+ - x_-}{\alpha_+ - \alpha_-}. \end{aligned} \tag{2.8}$$

Replacing x_1 and x_2 with x_+ and x_-, Eq. 2.7 now takes the form

$$\begin{aligned} &\ddot{x}_+ + \mu\dot{x}_+ + [\frac{(\omega_1^2 + k_1 + \alpha_- k_2)\alpha_+ - (\alpha_-\omega_2^2 + k_1 + \alpha_- k_2)}{\alpha_+ - \alpha_-}]x_+ \\ &+ [\frac{(\alpha_-\omega_2^2 + k_1 + \alpha_- k_2) - \alpha_-(\omega_1^2 + k_1 + \alpha_- k_2)}{\alpha_+ - \alpha_-}]x_- = 0, \\ &\ddot{x}_- + \mu\dot{x}_- + [\frac{(\alpha_+\omega_2^2 + k_1 + \alpha_+ k_2) - \alpha_-(\omega_1^2 + k_1 + \alpha_+ k_2)}{\alpha_+ - \alpha_-}]x_- \\ &+ [\frac{\alpha_+(\omega_1^2 + k_1 + \alpha_+ k_2) - (\alpha_+\omega_2^2 + k_1 + \alpha_+ k_2)}{\alpha_+ - \alpha_-}]x_+ = 0. \end{aligned} \tag{2.9}$$

Employing Eq. 2.3, it can be easily verified that

$$\begin{aligned} &[\frac{(\omega_1^2 + k_1 + \alpha_- k_2)\alpha_+ - (\alpha_-\omega_2^2 + k_1 + \alpha_- k_2)}{\alpha_+ - \alpha_-}] = \omega_+^2, \\ &[\frac{(\alpha_+\omega_2^2 + k_1 + \alpha_+ k_2) - \alpha_-(\omega_1^2 + k_1 + \alpha_+ k_2)}{\alpha_+ - \alpha_-}] = \omega_-^2, \\ &[\frac{(\alpha_-\omega_2^2 + k_1 + \alpha_- k_2) - \alpha_-(\omega_1^2 + k_1 + \alpha_- k_2)}{\alpha_+ - \alpha_-}] = 0, \\ &[\frac{\alpha_+(\omega_1^2 + k_1 + \alpha_+ k_2) - (\alpha_+\omega_2^2 + k_1 + \alpha_+ k_2)}{\alpha_+ - \alpha_-}] = 0, \end{aligned} \tag{2.10}$$

Thus, the original coupled equations of motion (Eq. 2.6) can be reduced to

$$\begin{aligned} \ddot{x}_+ + \mu\dot{x}_+ + \omega_+^2 x_+ = 0, \\ \ddot{x}_- + \mu\dot{x}_- + \omega_-^2 x_- = 0, \end{aligned} \tag{2.11}$$

where in the decoupled basis each oscillator has its own resonance frequency corresponding to one of the eigen-frequencies of the linear system without damping (Eq. 2.1). The solution to Eq. 2.11 yields the simple form (underdamping presumed)

$$\begin{aligned} x_+ = A_+ e^{(-\frac{\mu}{2} + i\sqrt{w_+^2 - \frac{\mu^2}{4}})t} + C.C., \\ x_- = A_- e^{(-\frac{\mu}{2} + i\sqrt{w_-^2 - \frac{\mu^2}{4}})t} + C.C., \end{aligned} \tag{2.12}$$

where A_+ and A_- are constants determined by the initial conditions and C.C. stands for complex conjugate. Due to frictional damping, the solutions now yield a decaying oscillation with the oscillation resonance frequencies modified by the damping coefficient $\sqrt{\omega_\pm^2 - \frac{\mu^2}{4}}$. In cases where the damping is small compared to the linear resonance frequencies (i.e., $\frac{\mu^2}{4} << \omega_\pm^2$), this modification of the resonance frequencies can be ignored.

2.3 Coupled Oscillators with Frictional Damping and External Driving

To this point, the equations of motion describing the coupled oscillators have all been assumed to be homogenous, i.e., no external driving force is applied to the oscillators. Provided an initial perturbation, the oscillators respond freely. However, in the presence of a continuous external driving mechanism, the overall oscillator behavior will be dominated by the external driving force. As a representative example, we will assume a sinusoidal driving force. For an external sinusoidal driving force applied to both oscillators simultaneously and synchronized at time $t = 0$, i.e., there is no phase difference between the driving signal applied to either oscillator, the equations of motion are

$$\begin{aligned} \ddot{x}_1 + \mu\dot{x}_1 + \omega_1^2 x_1 + k_1(x_1 - x_2) &= F_1 e^{i\Omega t} + C.C., \\ \ddot{x}_2 + \mu\dot{x}_2 + \omega_2^2 x_2 + k_2(x_2 - x_1) &= F_2 e^{i\Omega t} + C.C., \end{aligned} \tag{2.13}$$

where F_1, F_2 are the amplitudes of the sinusoidal driving signal normalized by the mass (having units of acceleration) and Ω is the frequency of the driving signal. Following the same approach as in Eq. 2.7, Eq. 2.13 can be decoupled into the x_+ and x_- basis as

$$\begin{aligned} \ddot{x}_+ + \mu\dot{x}_+ + \omega_+^2 x_+ &= F_+ e^{i\Omega t} + C.C., \\ \ddot{x}_- + \mu\dot{x}_- + \omega_-^2 x_- &= F_- e^{i\Omega t} + C.C., \end{aligned} \tag{2.14}$$

where F_+ and F_- are driving amplitudes appearing in decoupled coordinates as $F_+ = F_1 - \alpha_- F_2$ and $F_- = F_1 - \alpha_+ F_2$. The solution to Eq. 2.14 has the following form:

$$\begin{aligned} x_+ &= \frac{F_+}{[(\omega_+^2 - \Omega^2)^2 + (\mu\Omega)^2]^{\frac{1}{2}}} e^{i[\Omega t + arctg(\frac{-\mu\Omega}{\omega_+^2 - \Omega^2})]} + A_+ e^{(-\frac{\mu}{2} + i\sqrt{w_+^2 - \frac{\mu^2}{4}})t} + C.C., \\ x_- &= \frac{F_-}{[(\omega_-^2 - \Omega^2)^2 + (\mu\Omega)^2]^{\frac{1}{2}}} e^{i[\Omega t + arctg(\frac{-\mu\Omega}{\omega_-^2 - \Omega^2})]} + A_- e^{(-\frac{\mu}{2} + i\sqrt{w_-^2 - \frac{\mu^2}{4}})t} + C.C. \end{aligned} \tag{2.15}$$

This solution has two parts. The first represents the response to the external driving signal and has identical oscillation frequencies but shifted phases (i.e., $\phi = arctg(\frac{-\mu\Omega}{\omega_+^2 - \Omega^2})$) with respect to the external driving signal. The relationship between the amplitude of this response and the driving frequency, i.e., $\frac{F_+}{[(\omega_\pm^2 - \Omega^2)^2 + (\mu\Omega)^2]^{\frac{1}{2}}}$ and $\frac{F_-}{[(\omega_\pm^2 - \Omega^2)^2 + (\mu\Omega)^2]^{\frac{1}{2}}}$ quantifies the response of the system to a stimulus and is known as the theoretical amplitude-frequency response. The second part of this solution is the general solution corresponding to homogenous equations of motion (Eq. 2.11) which decay at large times, t.

2.4 Coupled Oscillators with Nonlinear and Non-reciprocal Interaction

So far, all of the systems discussed have been limited to the linear regime, i.e., all the forces (except the neutral drag force) have been linear in displacement (x_1 or x_2). However, forces are not always linear in nature. For example, if the particle position is dependent on the charge fluctuation or the sheath potential deviates from a parabolic profile, the background restoring force will no longer necessarily be linear in displacement [39–41]. This is of particular importance for the non-reciprocal particle-particle interaction created by the ion wake, since a linear approximation of the resulting particle-particle interaction force does not precisely describe the essence of the fundamental physics involved.

Therefore, the non-reciprocal particle-particle interaction will be studied in the nonlinear regime and considered to second order in displacement in the equations of motion for coupled oscillators. By considering the interaction forces to second order in displacement, the equations of motion for the coupled oscillators under external excitations are

$$\begin{aligned} \ddot{x}_1 + \mu\dot{x}_1 + \omega_1^2 x_1 + k_1(x_1 - x_2) + k_1'(x_1 - x_2)^2 &= F_1 e^{i\Omega t} + C.C., \\ \ddot{x}_2 + \mu\dot{x}_2 + \omega_2^2 x_2 + k_2(x_2 - x_1) + k_2'(x_2 - x_1)^2 &= F_2 e^{i\Omega t} + C.C., \end{aligned} \tag{2.16}$$

where k_1' and k_2' are the coefficients for the nonlinear parts of the particle-particle interaction. Following the same approach as in Eq. 2.7, Eq. 2.16 can be decoupled into the x_+ and x_- basis as

$$\begin{aligned} \ddot{x}_+ + \mu\dot{x}_+ + \omega_+^2 x_+ + g_1(C_1 x_+ - C_2 x_-)^2 &= F_+ e^{i\Omega t} + C.C., \\ \ddot{x}_- + \mu\dot{x}_- + \omega_-^2 x_- + g_2(C_1 x_+ - C_2 x_-)^2 &= F_- e^{i\Omega t} + C.C., \end{aligned} \tag{2.17}$$

where g_1, g_2, C_1 ,C_2, F_+ and F_- are now transformed in the following manner,

$$\begin{aligned} g_1 &= \frac{k_1' - (\alpha_-)k_2'}{[(\alpha_+) - (\alpha_-)]^2}, \\ g_2 &= \frac{k_1' - (\alpha_+)k_2'}{[(\alpha_+) - (\alpha_-)]^2}, \end{aligned} \tag{2.18}$$

$$\begin{aligned} C_1 &= \alpha_+ - 1, \\ C_2 &= \alpha_- - 1, \end{aligned} \tag{2.19}$$

$$\begin{aligned} F_+ &= F_1 - (\alpha_-)F_2, \\ F_- &= F_1 - (\alpha_+)F_2. \end{aligned} \tag{2.20}$$

As shown in Eq. 2.17, even though the decoupling process successfully eliminates coupling in the linear regime, it fails to decouple the nonlinear terms. Since Eq. 2.17 involves nonlinear (quadratic) terms and these nonlinear terms are coupled, it is unfeasible (if not impossible) to derive a set of analytical solutions. However, these nonlinear equations of motion can still be attacked by applying the multiple-scale perturbation method.

2.5 Multiple-Scale Perturbation Theory

The multiple-scale perturbation method seeks to determine uniformly valid approximation solutions to a perturbed system by introducing new fast scale and slow scale variables which can be solved independently within their own scale domain. These newly introduced fast and slow scale variables lead to secular terms that must be eliminated in order to compensate for the extra degree of freedom introduced and to remain self-consistent. This is known as determining the solvability conditions. As a type of perturbation method, the multiple-scale method benefits from wide application and is mathematically supported by both coordinate transforms and invariant manifolds.

Returning to the problem of coupled oscillators with nonlinear and non-reciprocal interaction, Eq. 2.17 must now be rewritten in terms of a small dimensionless parameter ϵ determining perturbations of the system under which the multiple-scale method is applicable. Since the system in question is driven by an external excitation, it must be attacked across different regions in terms of the frequency of external excitation so that resonances can be treated in a reasonable manner.

We first consider the situation where the external excitation frequency is close to the resonance frequency of the 'plus' eigen-mode, i.e., $\Omega \approx \omega_+$. In this case, the 'plus' eigen-mode resonates in phase with the external excitation, while the 'minus' eigen-mode does not (assuming ω_+ is far away from ω_-, thus $\Omega \not\approx \omega_-$). Eq. 2.17 may be rewritten in this region as

$$\begin{aligned} \ddot{x}_+ + \epsilon\mu\dot{x}_+ + \omega_+^2 x_+ + g_1(C_1 x_+ - C_2 x_-)^2 &= (\epsilon^2 F_+)e^{i\Omega t} + C.C., \\ \ddot{x}_- + \epsilon\mu\dot{x}_- + \omega_-^2 x_- + g_2(C_1 x_+ - C_2 x_-)^2 &= (\epsilon F_-)e^{i\Omega t} + C.C.. \end{aligned} \tag{2.21}$$

The basic guideline for determining ϵ is to ensure that both damping and nonlinearities appear on the same order of ϵ [42]. Moreover, for oscillators resonating to external excitation, the external drive should also be on the same order of ϵ (as the damping and nonlinearities) ensuring that the resonant oscillator will have a bounded oscillation amplitude. (For off-resonant oscillators, this is not necessary.) As we shall show, the selection of $\epsilon\mu$, $(\epsilon^2 F_+)$ and (ϵF_-) employed here meets all the afore mentioned requirements for an external excitation resonating with the 'plus' eigen-mode when suitable test solutions are considered.

We introduce our test solutions as

$$\begin{aligned} x_+(t_0, t_1; \epsilon) &= \epsilon x_{+1}(t_0, t_1) + \epsilon^2 x_{+2}(t_0, t_1) + ..., \\ x_-(t_0, t_1; \epsilon) &= \epsilon x_{-1}(t_0, t_1) + \epsilon^2 x_{-2}(t_0, t_1) + ..., \end{aligned} \tag{2.22}$$

where $t_0 = t$ is the 'fast' time (linear) and $t_1 = \epsilon t$ is the 'slow' time (nonlinear). In this case, test solutions only need to be retained to second order in ϵ since this system contains only quadratic nonlinearities. Since t_0 (the fast time) is independent of the slow time (t_1), the time derivative operator now yields $\frac{\partial}{\partial t} = \frac{\partial}{\partial t_0} + \epsilon \frac{\partial}{\partial t_1}$, and the second derivative operator yields $\frac{\partial^2}{\partial t^2} = \frac{\partial^2}{\partial t_0^2} + 2\epsilon \frac{\partial^2}{\partial t_0 \partial t_1} + \epsilon^2 \frac{\partial^2}{\partial t_1^2}$. Employing the test solutions shown in Eq. 2.22 in Eq. 2.21 and applying the new derivative operators, we come up with the following equations

$$\begin{aligned} &\epsilon \frac{\partial^2 x_{+1}}{\partial t_0^2} + \epsilon^2 \frac{\partial^2 x_{+2}}{\partial t_0^2} + 2\epsilon^2 \frac{\partial^2 x_{+1}}{\partial t_0 \partial t_1} + 2\epsilon^3 \frac{\partial^2 x_{+2}}{\partial t_0 \partial t_1} + \epsilon^3 \frac{\partial^2 x_{+1}}{\partial t_1^2} + \epsilon^4 \frac{\partial^2 x_{+2}}{\partial t_1^2} \\ &+ \epsilon^2 \mu \frac{\partial x_{+1}}{\partial t_0} + \epsilon^3 \mu \frac{\partial x_{+2}}{\partial t_0} + \epsilon^3 \mu \frac{\partial x_{+1}}{\partial t_1} + \epsilon^4 \mu \frac{\partial x_{+2}}{\partial t_1} + \epsilon \omega_+^2 x_{+1} + \epsilon^2 \omega_+^2 x_{+2} \\ &+ g_1(\epsilon C_1 x_{+1} + \epsilon^2 C_1 x_{+2} - \epsilon C_2 x_{-1} - \epsilon^2 C_2 x_{-2})^2 = \epsilon^2 F_+ e^{i\Omega t} + C.C., \end{aligned} \tag{2.23}$$

$$\begin{aligned} &\epsilon \frac{\partial^2 x_{-1}}{\partial t_0^2} + \epsilon^2 \frac{\partial^2 x_{-2}}{\partial t_0^2} + 2\epsilon^2 \frac{\partial^2 x_{-1}}{\partial t_0 \partial t_1} + 2\epsilon^3 \frac{\partial^2 x_{-2}}{\partial t_0 \partial t_1} + \epsilon^3 \frac{\partial^2 x_{-1}}{\partial t_1^2} + \epsilon^4 \frac{\partial^2 x_{-2}}{\partial t_1^2} \\ &+ \epsilon^2 \mu \frac{\partial x_{-1}}{\partial t_0} + \epsilon^3 \mu \frac{\partial x_{-2}}{\partial t_0} + \epsilon^3 \mu \frac{\partial x_{-1}}{\partial t_1} + \epsilon^4 \mu \frac{\partial x_{-2}}{\partial t_1} + \epsilon \omega_-^2 x_{-1} + \epsilon^2 \omega_-^2 x_{-2} \\ &+ g_2(\epsilon C_1 x_{+1} + \epsilon^2 C_1 x_{+2} - \epsilon C_2 x_{-1} - \epsilon^2 C_2 x_{-2})^2 = \epsilon F_- e^{i\Omega t} + C.C.. \end{aligned} \tag{2.24}$$

Eqs. 2.23 and 2.24 can be simplified by dropping higher order approximations and only keeping terms to $O(\epsilon^2)$ as

$$\begin{aligned}&\epsilon(\frac{\partial^2 x_{+1}}{\partial t_0^2}+\omega_+^2 x_{+1})+\epsilon^2[2\frac{\partial^2 x_{+1}}{\partial t_0 \partial t_1}+\frac{\partial^2 x_{+1}}{\partial t_1^2}+\frac{\partial^2 x_{+2}}{\partial t_0^2}+\mu\frac{\partial^2 x_{+1}}{\partial t_0^2}\\&+\omega_+^2 x_{+2}+g_1(C_1 x_{+1}-C_2 x_{-1})^2-F_+e^{i\Omega t}]=0,\end{aligned} \tag{2.25}$$

$$\begin{aligned}&\epsilon(\frac{\partial^2 x_{-1}}{\partial t_0^2}+\omega_-^2 x_{-1}-F_-e^{i\Omega t})+\epsilon^2[2\frac{\partial^2 x_{-1}}{\partial t_0 \partial t_1}+\frac{\partial^2 x_{-1}}{\partial t_1^2}+\frac{\partial^2 x_{-2}}{\partial t_0^2}\\&+\mu\frac{\partial^2 x_{-1}}{\partial t_0^2}+\omega_-^2 x_{-2}+g_2(C_1 x_{+1}-C_2 x_{-1})^2]=0.\end{aligned} \tag{2.26}$$

(From now on, the complex conjugate C.C. will be ignored for simplicity. However, the external excitation forces as well as the test solutions x_+ and x_- will always be understood to be accompanied by their complex conjugate components unless specifically clarified.) Eq. 2.25 and Eq. 2.26 are valid for any ϵ if and only if the terms associated with ϵ and ϵ^2 are respectively zero, which results in equations of motion to different scales (or to different orders of ϵ).

The equations of motion to first order in ϵ now take the form,

$$\frac{\partial^2 x_{+1}}{\partial t_0^2}+\omega_+^2 x_{+1}=0, \tag{2.27}$$

$$\frac{\partial^2 x_{-1}}{\partial t_0^2}+\omega_-^2 x_{-1}=F_-e^{i\Omega t}, \tag{2.28}$$

where it is important to note that $t_0=t$, thus $F_-e^{i\Omega t}=F_-e^{i\Omega t_0}$. It is now clear from Eq. 2.27 why F_+ is accompanied by ϵ^2. If F_+ has the same order as F_- (i.e., $\epsilon F_+e^{i\Omega t}$), $F_+e^{i\Omega t}$ would appear in the right hand side of Eq. 2.27. However, since the external excitation frequency Ω is close to the resonance frequency ω_+ of the 'plus' mode, x_{+1} yields a resonant solution as $x_{+1}(t_0,t_1)\propto t_0e^{i\Omega t_0}$ which is unbounded when time t_0 becomes large. Since this is not the case for off-resonant cases, the solution of Eq. 2.28 yields $x_{-1}(t_0,t_1)\propto e^{i\Omega t_0}$ which is bounded in time t_0.

The solutions to the equations of motion to first order in ϵ are

$$x_{+1}(t_0, t_1) = A(t_1)e^{i\omega_+ t_0}, \tag{2.29}$$

$$x_{-1}(t_0, t_1) = \frac{F_-}{-\Omega^2 + \omega_-^2}e^{i\Omega t_0} + B(t_1)e^{i\omega_- t_0}, \tag{2.30}$$

where $A(t_1)$ and $B(t_1)$ are functions of the slow time t_1 which must be solved using the solvability conditions.

The equations of motion to second order in ϵ take the form,

$$\frac{\partial^2 x_{+2}}{\partial t_0^2} + \omega_+^2 x_{+2} = -2\frac{\partial^2 x_{+1}}{\partial t_0 \partial t_1} - \mu\frac{\partial x_{+1}}{\partial t_0} - g_1(C_1 x_{+1} - C_2 x_{-1})^2 + F_+ e^{i\Omega t}, \tag{2.31}$$

$$\frac{\partial^2 x_{-2}}{\partial t_0^2} + \omega_-^2 x_{-2} = -2\frac{\partial^2 x_{-1}}{\partial t_0 \partial t_1} - \mu\frac{\partial x_{-1}}{\partial t_0} - g_2(C_1 x_{+1} - C_2 x_{-1})^2. \tag{2.32}$$

It is in this order that the damping and nonlinearities (as well as the external excitation term for the 'plus' mode) exist. By inserting the first order approximation solutions Eq. 2.29 and Eq. 2.30 into the right hand side of Eq. 2.31 and Eq. 2.32, we achieve

$$\begin{aligned}
\frac{\partial^2 x_{+2}}{\partial t_0^2} + \omega_+^2 x_{+2} =& - 2i\omega_+\frac{\partial A}{\partial t_1}e^{i\omega_+ t_0} - \mu i\omega_+ A e^{i\omega_+ t_0} + F_+ e^{i(\omega_+ t_0 + \delta t_1)} \\
& - g_1[C_1^2 A^2 e^{i2\omega_+ t_0} + C_2^2 B^2 e^{i2\omega_- t_0} + C_2^2(\frac{F_-}{-\Omega^2 + \omega_-^2})^2 e^{i2(\omega_+ t_0 + \delta t_1)} \\
& - 2C_1 C_2 A B e^{i(\omega_+ - \omega_-)t_0} - 2C_1 C_2 A(\frac{F_-}{-\Omega^2 + \omega_-^2})e^{i(2\omega_+ t_0 + \delta t_1)} \\
& + 2C_2^2 B(\frac{F_-}{-\Omega^2 + \omega_-^2})e^{i(\omega_+ t_0 + \omega_- t_0 + \delta t_1)} - 2C_1 C_2 A B^* e^{i(\omega_+ t_0 - \omega_- t_0)} \\
& - 2C_1 C_2 A(\frac{F_-}{-\Omega^2 + \omega_-^2})e^{-i\delta t_1} + 2C_2^2 B^*(\frac{F_-}{-\Omega^2 + \omega_-^2})e^{i(\omega_+ t_0 - \omega_- t_0 + \delta t_1)} \\
& + C_1^2 A A^* + C_2^2 B B^* + C_2^2(\frac{F_-}{-\Omega^2 + \omega_-^2})^2] + C.C.,
\end{aligned} \tag{2.33}$$

$$
\begin{aligned}
\frac{\partial^2 x_{-2}}{\partial t_0^2} + \omega_-^2 x_{-2} = &-2i\omega_- \frac{\partial B}{\partial t_1} e^{i\omega_- t_0} - \mu i\omega_- B e^{i\omega_- t_0} + i\Omega(\frac{F_-}{-\Omega^2+\omega_-^2}) e^{i(\omega_+ t_0 + \delta t_1)} \\
&- g_2[C_1^2 A^2 e^{i2\omega_+ t_0} + C_2^2 B^2 e^{i2\omega_- t_0} + C_2^2(\frac{F_-}{-\Omega^2+\omega_-^2})^2 e^{i2(\omega_+ t_0 + \delta t_1)} \\
&- 2C_1C_2ABe^{i(\omega_+ - \omega_-)t_0} - 2C_1C_2A(\frac{F_-}{-\Omega^2+\omega_-^2}) e^{i(2\omega_+ t_0 + \delta t_1)} \\
&+ 2C_2^2 B(\frac{F_-}{-\Omega^2+\omega_-^2}) e^{i(\omega_+ t_0 + \omega_- t_0 + \delta t_1)} - 2C_1C_2AB^* e^{i(\omega_+ t_0 - \omega_- t_0)} \\
&- 2C_1C_2A(\frac{F_-}{-\Omega^2+\omega_-^2}) e^{-i\delta t_1} + 2C_2^2 B^*(\frac{F_-}{-\Omega^2+\omega_-^2}) e^{i(\omega_+ t_0 - \omega_- t_0 + \delta t_1)} \\
&+ C_1^2 AA^* + C_2^2 BB^* + C_2^2(\frac{F_-}{-\Omega^2+\omega_-^2})^2] + C.C.,
\end{aligned}
\tag{2.34}
$$

where A^* and B^* are the complex conjugates of A and B. By writing the external excitation frequency explicitly as $\Omega = \omega_+ + \epsilon\delta$, the corresponding exponential term $e^{i\Omega t_0}$ yields $e^{i\Omega t_0} = e^{i(\omega_+ + \epsilon\delta)t_0} = e^{i(\omega_+ t_0 + \delta t_1)}$ (notice that $t_1 = \epsilon t = \epsilon t_0$), which allows us to find and eliminate the secular terms.

In this case, these secular terms lead to unbounded growth in solutions (in a similar manner as the external excitation terms for a resonating oscillator). In Eq. 2.33, the secular term is the term associated with $e^{i\omega_+ t_0}$, while in Eq. 2.34, it is the term associated with $e^{i\omega_- t_0}$. Eliminating both (by forcing them to zero) in Eq. 2.33 and Eq. 2.34, the solvability conditions are identified as

$$
-2i\omega_+ \frac{\partial A}{\partial t_1} - \mu i\omega_+ A + F_+ e^{i\delta t_1} = 0, \tag{2.35}
$$

$$
-2i\omega_- \frac{\partial B}{\partial t_1} - \mu i\omega_- B = 0, \tag{2.36}
$$

which can be easily solved for A and B as

$$
A(t_1) = \frac{F_+}{i\omega_+(\mu + i2\delta)} e^{i\delta t_1} + Ce^{-\frac{\mu}{2}t_1}, \tag{2.37}
$$

$$
B(t_1) = C' e^{-\frac{\mu}{2}t_1}, \tag{2.38}
$$

where C and C' are constants that can be determined using the initial conditions.

Inserting $A(t_1)$ and $B(t_1)$ into $x_{+1}(t_0, t_1)$ and $x_{-1}(t_0, t_1)$ and deriving the solutions $x_+(t_0, t_1; \epsilon)$ and $x_-(t_0, t_1; \epsilon)$ to first order of approximation yields:

$$\begin{aligned} x_+(t_0, t_1; \epsilon) =& \epsilon \frac{-F_+}{\omega_+(\mu^2 + 4\delta^2)^{\frac{1}{2}}} e^{iarctg(\frac{\mu}{2\delta})} e^{i(\delta t_1 + \omega_+ t_0)} + \epsilon C e^{(-\frac{\mu}{2}t_1 + i\omega_+ t_0)} \\ =& \frac{-(\epsilon^2 F_+)}{\omega_+[(\epsilon\mu)^2 + 4(\epsilon\delta)^2)]^{\frac{1}{2}}} e^{iarctg(\frac{\epsilon\mu}{2\epsilon\delta})} e^{i(\delta t_1 + \omega_+ t_0)} + \epsilon C e^{(-\frac{\mu}{2}t_1 + i\omega_+ t_0)}, \end{aligned} \tag{2.39}$$

$$\begin{aligned} x_-(t_0, t_1; \epsilon) =& \epsilon(\frac{F_-}{-\Omega^2 + \omega_-^2}) e^{i\Omega t_0} + \epsilon C' e^{(-\frac{\mu}{2}t_1 + i\omega_- t_0)} \\ =& \frac{(\epsilon F_-)}{-\Omega^2 + \omega_-^2} e^{i\Omega t_0} + \epsilon C' e^{(-\frac{\mu}{2}t_1 + i\omega_- t_0)}. \end{aligned} \tag{2.40}$$

Noting that $\Omega = \omega_+ + \epsilon\delta$, $t_1 = \epsilon t$ and $t_0 = t$, Eq. 2.39 and Eq. 2.40 can now be written in the time t scale as

$$x_+(t) = \frac{-(\epsilon^2 F_+)}{\omega_+[(\epsilon\mu)^2 + 4(\Omega - \omega_+)^2)]^{\frac{1}{2}}} e^{i[\Omega t + arctg(\frac{\epsilon\mu}{2(\Omega - \omega_+)})]} + \epsilon C e^{(-\frac{\epsilon\mu}{2}t + i\omega_+ t)}, \tag{2.41}$$

$$x_-(t) = \frac{(\epsilon F_-)}{-\Omega^2 + \omega_-^2} e^{i\Omega t} + \epsilon C' e^{(-\frac{\epsilon\mu}{2}t + i\omega_- t)}. \tag{2.42}$$

Hence, we have now derived the solutions to the equations of motion Eq. 2.17 to first order of approximation. This is adequate for describing the motion of coupled oscillators when the 'plus' mode is in resonance with the external excitation. It is important, however, to mention that the parameters μ, F_+ and F_- in Eq. 2.17 are now represented respectively by $\epsilon\mu$, $\epsilon^2 F_+$ and ϵF_- in the solutions given by Eq. 2.41 and Eq. 2.42. In other words, $\epsilon\mu$ is now understood to be the damping (neutral drag) coefficient, and $\epsilon^2 F_+$, ϵF_- are understood to be the external excitation amplitudes transferred into the decoupled 'plus' and 'minus' basis. Also, after a long time (i.e., for large t) $\epsilon C e^{(-\frac{\epsilon\mu}{2}t + i\omega_+ t)}$ and $\epsilon C' e^{(-\frac{\epsilon\mu}{2}t + i\omega_- t)}$ in the right hand side of Eq. 2.41 and Eq. 2.42 will finally decay completely. Therefore, only those parts responding to the external excitation will be left.

The situation for an external excitation resonating in the 'minus' mode is similar. In this case, the equations of motion become

$$\begin{aligned} \ddot{x}_+ + \epsilon\mu\dot{x}_+ + \omega_+^2 x_+ + g_1(C_1x_+ - C_2x_-)^2 &= (\epsilon F_+)e^{i\Omega t}, \\ \ddot{x}_- + \epsilon\mu\dot{x}_- + \omega_-^2 x_- + g_2(C_1x_+ - C_2x_-)^2 &= (\epsilon^2 F_-)e^{i\Omega t}, \end{aligned} \tag{2.43}$$

where F_- is connected to ϵ^2, since it is now the 'minus' mode resonating with the external excitation. Following the same approach as before and considering excitation frequencies close to the 'minus' mode resonance frequency (i.e., $\Omega = \omega_- + \epsilon\delta$), the solutions to first order of approximation are

$$x_+(t) = \frac{(\epsilon F_+)}{-\Omega^2 + \omega_+^2}e^{i\Omega t} + \epsilon C e^{(-\frac{\epsilon\mu}{2}t + i\omega_+ t)}, \tag{2.44}$$

$$x_-(t) = \frac{-(\epsilon^2 F_-)}{\omega_-[(\epsilon\mu)^2 + 4(\Omega - \omega_-)^2)]^{\frac{1}{2}}}e^{i[\Omega t + arctg(\frac{\epsilon\mu}{2(\Omega-\omega_+)})]} + \epsilon C' e^{(-\frac{\epsilon\mu}{2}t + i\omega_- t)}, \tag{2.45}$$

where $\epsilon\mu$, ϵF_+ and $\epsilon^2 F_-$ are understood to be the damping (neutral drag) coefficient, and the excitation amplitudes have been transferred into the decoupled basis.

It is also interesting to explore the equations of motion Eq. 2.17 when neither mode is resonating with the external excitation. In this case, particular emphasis will be placed on situations where the excitation frequency is not close to either the 'plus' mode or 'minus' mode resonance frequency, but is instead close to half of the 'plus' mode resonance frequency or half of the 'minus' mode resonance frequency.

We first discuss the case where the excitation frequency is close to half of the 'plus' mode resonance frequency, i.e., $\Omega \approx \frac{1}{2}\omega_+$. The equations of motion for this case (ordered in ϵ) are

$$\begin{aligned} \ddot{x}_+ + \epsilon\mu\dot{x}_+ + \omega_+^2 x_+ + g_1(C_1x_+ - C_2x_-)^2 &= (\epsilon F_+)e^{i\Omega t}, \\ \ddot{x}_- + \epsilon\mu\dot{x}_- + \omega_-^2 x_- + g_2(C_1x_+ - C_2x_-)^2 &= (\epsilon F_-)e^{i\Omega t}. \end{aligned} \tag{2.46}$$

In Eq. 2.46, both of the external excitation terms $(\epsilon F_+)e^{i\Omega t}$ and $(\epsilon F_-)e^{i\Omega t}$ are ordered in such a way that they do not appear at the same order of ϵ as do the damping and nonlinearities when considering possible test solutions. (This will be shown below.) It is important to note that since none of the modes now resonate with the external excitation, it is not necessary to order the excitation terms to the same order of ϵ as damping and nonlinearities.

Following a similar approach as above, we introduce Eq. 2.22 as test solutions and insert them into Eq. 2.46. Keeping terms up to $O(\epsilon^2)$, we have

$$\begin{aligned}&\epsilon(\frac{\partial^2 x_{+1}}{\partial t_0^2} + \omega_+^2 x_{+1} - F_+ e^{i\Omega t}) + \epsilon^2[2\frac{\partial^2 x_{+1}}{\partial t_0 \partial t_1} + \frac{\partial^2 x_{+1}}{\partial t_1^2} + \frac{\partial^2 x_{+2}}{\partial t_0^2} + \mu\frac{\partial^2 x_{+1}}{\partial t_0^2} \\ &+ \omega_+^2 x_{+2} + g_1(C_1 x_{+1} - C_2 x_{-1})^2 = 0,\end{aligned} \tag{2.47}$$

$$\begin{aligned}&\epsilon(\frac{\partial^2 x_{-1}}{\partial t_0^2} + \omega_-^2 x_{-1} - F_- e^{i\Omega t}) + \epsilon^2[2\frac{\partial^2 x_{-1}}{\partial t_0 \partial t_1} + \frac{\partial^2 x_{-1}}{\partial t_1^2} + \frac{\partial^2 x_{-2}}{\partial t_0^2} + \mu\frac{\partial^2 x_{-1}}{\partial t_0^2} \\ &+ \omega_-^2 x_{-2} + g_2(C_1 x_{+1} - C_2 x_{-1})^2] = 0.\end{aligned} \tag{2.48}$$

Equating all terms associated with ϵ and ϵ^2 to zero, we obtain equations of motion to first and second order of ϵ.

The equations of motion to the first order of ϵ yield

$$\frac{\partial^2 x_{+1}}{\partial t_0^2} + \omega_+^2 x_{+1} = F_+ e^{i\Omega t}, \tag{2.49}$$

$$\frac{\partial^2 x_{-1}}{\partial t_0^2} + \omega_-^2 x_{-1} = F_- e^{i\Omega t}, \tag{2.50}$$

which have the solution

$$x_{+1}(t_0, t_1) = \frac{F_+}{-\Omega^2 + \omega_+^2} e^{i\Omega t_0} + A(t_1) e^{i\omega_+ t_0}, \tag{2.51}$$

$$x_{-1}(t_0, t_1) = \frac{F_-}{-\Omega^2 + \omega_-^2} e^{i\Omega t_0} + B(t_1) e^{i\omega_- t_0}, \tag{2.52}$$

where again $A(t_1)$ and $B(t_1)$ are functions of slow time t_1 that can be determined by eliminating the secular terms. Solutions to the first order of approximation inserted into the equations of motion to the second order of ϵ yield

$$\frac{\partial^2 x_{+2}}{\partial t_0^2} + \omega_+^2 x_{+2} = -2\frac{\partial^2 x_{+1}}{\partial t_0 \partial t_1} - \mu \frac{\partial x_{+1}}{\partial t_0} - g_1 (C_1 x_{+1} - C_2 x_{-1})^2, \tag{2.53}$$

$$\frac{\partial^2 x_{-2}}{\partial t_0^2} + \omega_-^2 x_{-2} = -2\frac{\partial^2 x_{-1}}{\partial t_0 \partial t_1} - \mu \frac{\partial x_{-1}}{\partial t_0} - g_2 (C_1 x_{+1} - C_2 x_{-1})^2, \tag{2.54}$$

identifying the secular terms. Substituting Eq. 2.51 and Eq. 2.52 into Eq. 2.53 and Eq. 2.54, we achieve

$$\begin{aligned}
\frac{\partial^2 x_{+2}}{\partial t_0^2} + \omega_+^2 x_{+2} =& -2i\omega_+ \frac{\partial A}{\partial t_1} e^{i\omega_+ t_0} - \mu i \omega_+ A e^{i\omega_+ t_0} - \mu i \frac{\Omega F_+}{-\Omega^2 + \omega_+^2} e^{i(\frac{1}{2}\omega_+ t_0 + \frac{1}{2}\delta t_1)} \\
& - g_1 \{ C_1^2 A^2 e^{i2\omega_+ t_0} + C_2^2 B^2 e^{i2\omega_- t_0} \\
& + [C_1(\frac{F_+}{-\Omega^2 + \omega_+^2}) - C_2(\frac{F_-}{-\Omega^2 + \omega_-^2})]^2 e^{i(\omega_+ t_0 + \delta t_1)} \\
& + 2[C_1^2 A(\frac{F_+}{-\Omega^2 + \omega_+^2}) - C_1 C_2 A(\frac{F_-}{-\Omega^2 + \omega_-^2})] e^{i(\frac{3}{2}\omega_+ t_0 + \frac{1}{2}\delta t_1)} \\
& + 2[C_2^2 B(\frac{F_-}{-\Omega^2 + \omega_-^2}) - C_1 C_2 B(\frac{F_+}{-\Omega^2 + \omega_+^2})] e^{i[(\omega_- + \frac{1}{2}\omega_+) t_0 + \frac{1}{2}\delta t_1]} \\
& + 2[C_1^2 A(\frac{F_+}{-\Omega^2 + \omega_+^2}) - C_1 C_2 A(\frac{F_-}{-\Omega^2 + \omega_-^2})] e^{-i(\frac{1}{2}\omega_+ t_0 + \frac{1}{2}\delta t_1)} \\
& + 2[C_2^2 B(\frac{F_-}{-\Omega^2 + \omega_-^2}) - C_1 C_2 B(\frac{F_+}{-\Omega^2 + \omega_+^2})] e^{-i[\frac{1}{2}\delta t_1 - (\omega_- - \frac{1}{2}\omega_+) t_0]} \\
& - 2C_1 C_2 A B e^{i(\omega_+ + \omega_-) t_0} - 2C_1 C_2 A B^* e^{i(\omega_+ - \omega_-) t_0} + C_1^2 A A^* + C_2^2 B B^* \\
& + C_1^2 (\frac{F_+}{-\Omega^2 + \omega_+^2})^2 + C_2^2 (\frac{F_-}{-\Omega^2 + \omega_-^2})^2 \\
& - 2C_1 C_2 (\frac{F_+}{-\Omega^2 + \omega_+^2})(\frac{F_-}{-\Omega^2 + \omega_-^2}) \} + C.C.,
\end{aligned} \tag{2.55}$$

$$
\begin{aligned}
\frac{\partial^2 x_{-2}}{\partial t_0^2} + \omega_-^2 x_{-2} = &- 2i\omega_- \frac{\partial B}{\partial t_1} e^{i\omega_- t_0} - \mu i\omega_- B e^{i\omega_- t_0} - \mu i \frac{\Omega F_-}{-\Omega^2 + \omega_-^2} e^{i(\frac{1}{2}\omega_+ t_0 + \frac{1}{2}\delta t_1)} \\
&- g_2\{C_1^2 A^2 e^{i2\omega_+ t_0} + C_2^2 B^2 e^{i2\omega_- t_0} \\
&+ [C_1(\frac{F_+}{-\Omega^2 + \omega_+^2}) - C_2(\frac{F_-}{-\Omega^2 + \omega_-^2})]^2 e^{i(\omega_+ t_0 + \delta t_1)} \\
&+ 2[C_1^2 A(\frac{F_+}{-\Omega^2 + \omega_+^2}) - C_1 C_2 A(\frac{F_-}{-\Omega^2 + \omega_-^2})] e^{i(\frac{3}{2}\omega_+ t_0 + \frac{1}{2}\delta t_1)} \\
&+ 2[C_2^2 B(\frac{F_-}{-\Omega^2 + \omega_-^2}) - C_1 C_2 B(\frac{F_+}{-\Omega^2 + \omega_+^2})] e^{i[(\omega_- + \frac{1}{2}\omega_+) t_0 + \frac{1}{2}\delta t_1]} \\
&+ 2[C_1^2 A(\frac{F_+}{-\Omega^2 + \omega_+^2}) - C_1 C_2 A(\frac{F_-}{-\Omega^2 + \omega_-^2})] e^{-i(\frac{1}{2}\omega_+ t_0 + \frac{1}{2}\delta t_1)} \\
&+ 2[C_2^2 B(\frac{F_-}{-\Omega^2 + \omega_-^2}) - C_1 C_2 B(\frac{F_+}{-\Omega^2 + \omega_+^2})] e^{-i[\frac{1}{2}\delta t_1 - (\omega_- - \frac{1}{2}\omega_+) t_0]} \\
&- 2C_1 C_2 A B e^{i(\omega_+ + \omega_-) t_0} - 2C_1 C_2 A B^* e^{i(\omega_+ - \omega_-) t_0} + C_1^2 A A^* + C_2^2 B B^* \\
&+ C_1^2 (\frac{F_+}{-\Omega^2 + \omega_+^2})^2 + C_2^2 (\frac{F_-}{-\Omega^2 + \omega_-^2})^2 \\
&- 2C_1 C_2 (\frac{F_+}{-\Omega^2 + \omega_+^2})(\frac{F_-}{-\Omega^2 + \omega_-^2})\} + C.C.,
\end{aligned}
\tag{2.56}
$$

where we write explicitly the excitation frequency close to half of the 'plus' mode resonance frequency as $\Omega = \frac{1}{2}\omega_+ + \frac{1}{2}\epsilon\delta$ and consider the slow time $t_1 = \epsilon t_0$ and fast time $t_0 = t$. In this case, the secular term in Eq. 2.55 is the term associated with $e^{\pm i\omega_+ t_0}$ (i.e., the part oscillating at the resonance frequency of the 'plus' mode ω_+), while the secular term in Eq. 2.56 is the term associated with $e^{\pm i\omega_- t_0}$ (i.e., the part oscillating at the resonance frequency of the 'minus' mode ω_-).

However, unlike the situation in Eq. 2.33 and Eq. 2.34, it is not easy to identify the secular terms (i.e., those associated with $e^{\pm i\omega_+ t_0}$ and $e^{\pm i\omega_- t_0}$) in Eq. 2.55 and Eq. 2.56 because there are addition and subtraction calculations between fractional multiplication of ω_+ and ω_- involved which might result in additional secular components. As a representative example, the term $[2C_2^2 B(\frac{F_-}{-\Omega^2+\omega_-^2}) - 2C_1 C_2 B(\frac{F_+}{-\Omega^2+\omega_+^2})] e^{i[(\omega_- + \frac{1}{2}\omega_+) t_0 + \frac{1}{2}\delta t_1]}$ in Eq. 2.55 will become a secular component if $(\omega_- + \frac{1}{2}\omega_+) \approx \omega_+$ which is possible if the resonance frequency of the 'minus' mode is close to half of the resonance frequency of the 'plus' mode: $\omega_- \approx \frac{1}{2}\omega_+$. Similarly, the term in Eq. 2.56 $2[C_1^2 A(\frac{F_+}{-\Omega^2+\omega_+^2}) - C_1 C_2 A(\frac{F_-}{-\Omega^2+\omega_-^2})]e^{-i(\frac{1}{2}\omega_+ t_0 + \frac{1}{2}\delta t_1)}$ will become a secular component as well under this condition since now $\frac{1}{2}\omega_+$ is approximately equal to ω_-. When relationships of the sort $\omega_- \approx \frac{1}{2}\omega_+$ hold in the system, we say that the system is tuned to an internal resonance state where the 'plus' mode resonates with the 'minus' mode in the nonlinear regime. It is clear that for the present system with quadratic nonlinearities $\omega_- \approx \frac{1}{2}\omega_+$, this is the only condition that can generate new secular components. For some complex systems, the triggering of an internal resonance is not limited to just the condition of a 1:2 relationship (i.e., $\omega_- : \omega_+ \approx 1:2$), but may occur due to any fractional relationship between resonance frequencies of system modes. In this case, additional secular components can possibly trigger an internal resonance. For instance, in a system with cubic nonlinearities, a 1:3 relationship between resonance frequencies of different modes becomes a typical condition for the system to be tuned into an internal resonance state.

For the case at hand, we ignore all internal resonances and assume that the resonance frequency of the 'minus' mode is far from the 'plus' mode, i.e., $\omega_- \not\approx \frac{1}{2}\omega_+$. Under these assumptions, we can eliminate the secular terms in Eq. 2.55 and Eq. 2.56 in the following way,

$$-2i\omega_+ \frac{\partial A}{\partial t_1} - \mu i \omega_+ A - g_1[C_1(\frac{F_+}{-\Omega^2+\omega_+^2}) - C_2(\frac{F_-}{-\Omega^2+\omega_-^2})]^2 e^{i\delta t_1} = 0, \tag{2.57}$$

$$-2i\omega_- \frac{\partial B}{\partial t_1} - \mu i \omega_- B = 0. \tag{2.58}$$

These equations yield straight-forward solutions as

$$A(t_1) = \frac{g_1[C_1(\frac{F_+}{-\Omega^2+\omega_+^2}) - C_2(\frac{F_-}{-\Omega^2+\omega_-^2})]^2}{-2i\delta - \mu} e^{i\delta t_1} + C e^{-\frac{\mu}{2}t_1}, \tag{2.59}$$

$$B(t_1) = C' e^{-\frac{\mu}{2}t_1}, \tag{2.60}$$

where C and C' are again initial condition dependent constants. Using Eq. 2.59 and Eq. 2.60 in Eq. 2.51 and Eq. 2.52, solutions to the first order of approximation are

$$\begin{aligned} x_+(t_0, t_1; \epsilon) =& \frac{\epsilon F_+}{-\Omega^2 + \omega_+^2} e^{i\Omega t_0} + \epsilon \frac{g_1[C_1(\frac{F_+}{-\Omega^2+\omega_+^2}) - C_2(\frac{F_-}{-\Omega^2+\omega_-^2})]^2}{\omega_+(\mu^2 + (2\delta)^2)^{\frac{1}{2}}} e^{i[\omega_+ t_0 + \delta t_1 + arctg(\frac{\mu}{2\delta})]} \\ &+ \epsilon C e^{-\frac{\mu}{2}t_1 + i\omega_+ t_0}, \end{aligned} \tag{2.61}$$

$$x_-(t_0, t_1, \epsilon) = \frac{\epsilon F_-}{-\Omega^2 + \omega_-^2} e^{i\Omega t_0} + \epsilon C' e^{-\frac{\mu}{2}t_1 + i\omega_- t_0}. \tag{2.62}$$

Again, considering $\Omega = \frac{1}{2}\omega_+ + \frac{1}{2}\epsilon\delta$, $t_1 = \epsilon t$ and $t_0 = t$, Eq. 2.61 and Eq. 2.62 can be written in the original time scale as

$$\begin{aligned} x_+(t) =& \frac{(\epsilon F_+)}{-\Omega^2 + \omega_+^2} e^{i\Omega t} + \frac{g_1[C_1(\frac{\epsilon F_+}{-\Omega^2+\omega_+^2}) - C_2(\frac{\epsilon F_-}{-\Omega^2+\omega_-^2})]^2}{\omega_+[(\epsilon\mu)^2 + 4(2\Omega - \omega_+)^2]^{\frac{1}{2}}} e^{i[2\Omega t + arctg(\frac{\epsilon\mu}{4\Omega - 2\omega_+})]} \\ &+ \epsilon C e^{-\frac{(\epsilon\mu)}{2}t + i\omega_+ t}, \end{aligned} \tag{2.63}$$

$$x_-(t) = \frac{(\epsilon F_-)}{-\Omega^2 + \omega_-^2} e^{i\Omega t} + \epsilon C' e^{-\frac{\epsilon\mu}{2}t + i\omega_- t}, \tag{2.64}$$

where $\epsilon\mu$, ϵF_+ and ϵF_- are understood to be the damping coefficient and the external excitation amplitude in the decoupled basis. Similar to the situation where modes directly resonate with the excitation (Eq. 2.41 and Eq. 2.42, or Eq. 2.44 and Eq. 2.45), the parts oscillating at the mode resonance frequencies will normally decay at large time t leaving terms that respond only to the external excitation. However, the situation here is a bit different. As can be seen in Eq. 2.63, besides the term oscillating at exactly the external excitation frequency $\frac{(\epsilon F_+)}{-\Omega^2+\omega_+^2} e^{i\Omega t}$, there is also another term oscillating at twice the external excitation frequency

$$\frac{g_1[C_1(\frac{\epsilon F_+}{-\Omega^2+\omega_+^2}) - C_2(\frac{\epsilon F_-}{-\Omega^2+\omega_-^2})]^2}{\omega_+[(\epsilon\mu)^2 + 4(2\Omega - \omega_+)^2]^{\frac{1}{2}}} e^{i[2\Omega t + arctg(\frac{\epsilon\mu}{4\Omega - 2\omega_+})]}$$

(with a shifted phase $\theta = arctg(\frac{\epsilon\mu}{4\Omega - 2\omega_+})$). This term is a secondary response to the excitation and is called the 'super-harmonic response'. It is important to point out that the secondary response appears in the solution to the first order of approximation (instead of a higher order approximation), which means that this secondary response is not trivial. It is, in fact, at least as significant as the primary response (i.e., the term oscillating at the exact excitation frequency) and should be detectable. This significant secondary response is a direct consequence of the quadratic nonlinearities inherent in the system.

For the case where the excitation frequency is close to the resonance frequency of the 'minus' mode, the above remains the same until we reach Eq. 2.56, where the secular terms need to be eliminated. For this case, the excitation frequency can be written explicitly as $\Omega = \frac{1}{2}\omega_- + \frac{1}{2}\epsilon\delta$ with the understanding that there is no internal resonance being considered $\omega_- \not\approx \frac{1}{2}\omega_+$. The corresponding solvability conditions are

$$-2i\omega_+\frac{\partial A}{\partial t_1} - \mu i\omega_+ A = 0, \tag{2.65}$$

$$-2i\omega_-\frac{\partial B}{\partial t_1} - \mu i\omega_- B - g_2[C_1(\frac{F_+}{-\Omega^2+\omega_+^2}) - C_2(\frac{F_-}{-\Omega^2+\omega_-^2})]^2 e^{i\delta t_1} = 0, \tag{2.66}$$

with solutions

$$A(t_1) = Ce^{-\frac{\mu}{2}t_1}, \tag{2.67}$$

$$B(t_1) = \frac{g_2[C_1(\frac{F_+}{-\Omega^2+\omega_+^2}) - C_2(\frac{F_-}{-\Omega^2+\omega_-^2})]^2}{-2i\delta - \mu} e^{i\delta t_1} + C'e^{-\frac{\mu}{2}t_1}. \tag{2.68}$$

The solutions to the equations of motion Eq. 2.46 to the first order of approximation are correspondingly:

$$x_+(t) = \frac{(\epsilon F_+)}{-\Omega^2+\omega_+^2} e^{i\Omega t} + \epsilon C e^{-\frac{(\epsilon\mu)}{2}t + i\omega_+ t}, \tag{2.69}$$

$$\begin{aligned} x_-(t) =& \frac{(\epsilon F_-)}{-\Omega^2+\omega_-^2} e^{i\Omega t} + \frac{g_2[C_1(\frac{\epsilon F_+}{-\Omega^2+\omega_+^2}) - C_2(\frac{\epsilon F_-}{-\Omega^2+\omega_-^2})]^2}{\omega_-[(\epsilon\mu)^2 + 4(2\Omega-\omega_-)^2]^{\frac{1}{2}}} e^{i[2\Omega t + arctg(\frac{\epsilon\mu}{4\Omega - 2\omega_-})]} \\ &+ \epsilon C' e^{-\frac{\epsilon\mu}{2}t + i\omega_- t}, \end{aligned} \tag{2.70}$$

where $\epsilon\mu$, ϵF_+ and ϵF_- are again the damping coefficient and the amplitudes of the external excitation in the decoupled coordinates.

To summarize, in this chapter we have derived the solutions for a system of coupled driven oscillators with non-reciprocal and nonlinear (quadratic nonlinearities) interaction (Eq. 2.16). Depending on the frequency of the excitation term, the solutions take different forms, i.e., in the primary excitation region, the solutions have the form shown in Eq. 2.61 and Eq. 2.62, while in the secondary region, the solutions take the forms given in Eq. 2.69 and Eq. 2.70. These solutions will now be used to describe the response behaviors of vertically aligned dust particle pairs levitated in the plasma sheath region to reveal the intrinsic nonlinearities in this particle-particle interaction.

CHAPTER THREE

Nonlinear Non-reciprocal Grain-Grain Interactions in the Direction of Ion Flow

This chapter mainly focuses on the experimental study of nonlinear interactions between grains aligned in the direction of the ion flow. (The detailed content of measuring the nonlinear grain-grain interaction in the direction of the ion flow is published in 'Nonlinear response of vertical paired structure in complex plasma' by Ding *et. al* [43]). Compared to the grain-grain interactions in the direction perpendicular to the ion flow, the interactions along the ion flow are much more asymmetric. The obvious reason is that the upstream and downstream particles are influenced by the streaming ions to a very different extent. When passing upstream particles, streaming ions are deflected and will be re-concentrated downstream as the ion wake. This makes the downstream particles much more vulnerable to effects caused by the ion wake. In the experiment, we focused on vertically aligned dust pairs (parallel to the ion flow), which is the simplest structure that still involves grain-grain interactions.

3.1 Experimental Equipment

The experiment was conducted in a modified Gaseous Electronic Conference (GEC) RF reference cell at the Center for Astrophysics, Space Physics, and Engineering Research (CASPER) at Baylor university. A GEC RF reference cell is a type of parallel plate, capacitively-coupled, RF plasma reactor that is suitable for studies of basic discharge phenomena, investigation of industrial-type plasmas, and theoretical modeling [44]. GEC reference cells were developed in response to the problem that plasma properties are strongly affected by the geometry of the discharge camber, preventing a meaningful comparison of research from different plasma systems. As a standard reference system, data obtained from a GEC RF reference cell are comparable to each other regardless of where the experiment is conducted in the world [45].

Fig. 3.1 shows one of the modified GEC RF reference cells (Cell 1) built at CASPER. The main vacuum chamber is highlighted by the yellow box (a) in Fig. 3.1. There is an upper electrode and a lower electrode mounted inside the chamber, and several monitoring windows were created around the chamber to enable visualization of the inside of the chamber. The region enclosed by the blue box (b) is the vacuum pumping system. This allows the chamber system to be pumped to a high vacuum of 10^{-6} Torr when it is not running. The red boxes (d) highlight the gas injection system. The lowest gas pressure without loss of the plasma ignition for this system is around 10 mTorr. The illumination laser (with wavelength 660 nm) and the camera (for recording of dust particles trajectories) are highlighted by the white (c) and the green (e) boxes respectively, and they are controlled by the controller (purple box) (f).

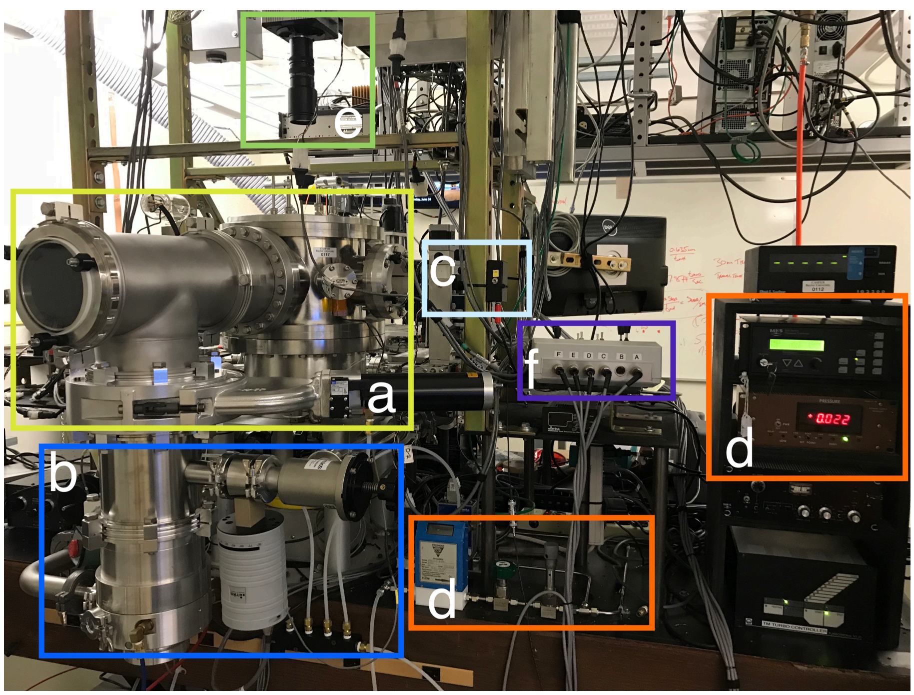

Figure 3.1: Modified GEC RF reference cell built at CASPER (the Cell 1). a) main chamber, b) vacuum pumping system, c) laser, d) gas injection system, e) camera and f) laser and camera controller.

Fig. 3.2 shows the electronic system for this modified GEC RF reference cell. The blue box (a) encloses the oscilloscopes for monitoring the forward and backward (reflected) RF signals as well as the peak to peak voltage and DC bias on the lower electrode. The purple box (b) marks the power supply for the illumination lasers. The orange box (c) indicates the RF signal generator which is used to provide RF signals to ignite gas discharge, and this generator is coupled to the power amplifier indicated by the white box (g). The green box (d) shows a regular signal function generator which can provide desired functions according to the experiment design. The yellow box (f) designates the DC power supply which controls the voltage on the DC bias. The RF power can be controlled either remotely or locally by the controller boxes (e, h).

A sketch of the main parts of the modified GEC RF reference cell is shown in Fig. 3.3.

3.2 Experiment

Melamine Formaldehyde (MF) particles with a diameter of 8.89 ± 0.09 μm were used as dust particles and were dropped into the chamber using the dust shaker mounted above the top electrode. Dust particles were directly dropped into a glass box of size of 20 mm $\times$ 18 mm $\times$ 18 mm (height $\times$ length $\times$ width) placed on the lower electrode, which provides strong horizontal confinement facilitating the formation of vertical chain (pair) structures. Initially, a dust cloud was formed and levitated in the box. However, by carefully reducing the plasma power, the dust particles can be dropped onto the lower electrode in a controlled fashion, leaving a single chain structure at low plasma power. Once there were only two particles left, i.e., a vertical dust pair structure was formed, the plasma power was raised to the desired value for the experiment. The plasma power and pressure were kept constant in each experimental trial.

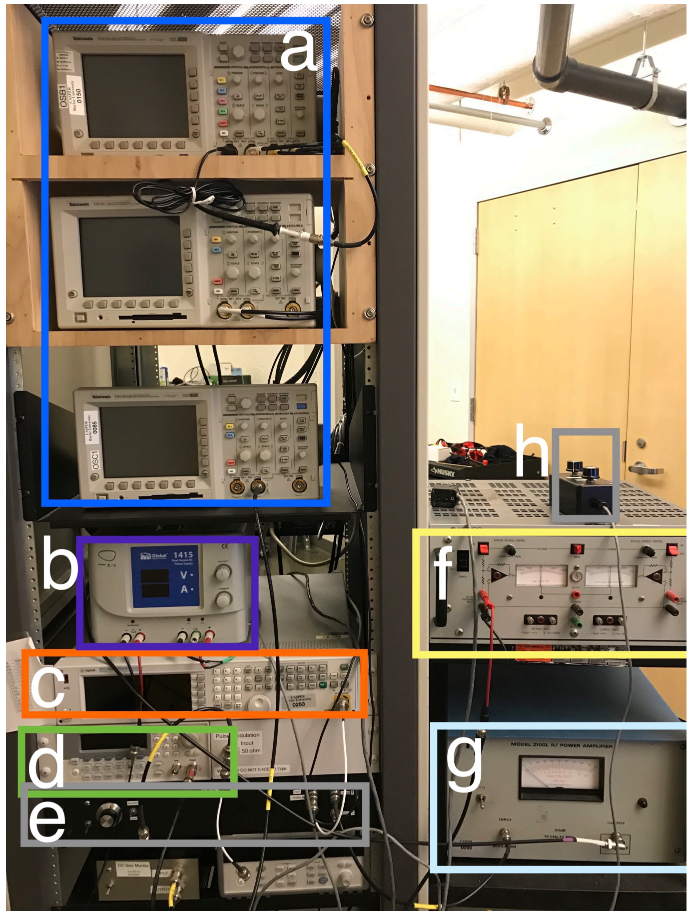

Figure 3.2: The electronic devices for the modified GEC RF reference cell built at CASPER. a) oscilloscopes, b) laser power supply, c) RF signal generator, d) signal function generator, e) variable passive attenuator, f) DC power supply, g) power amplifier and h) remote controller for the RF power.

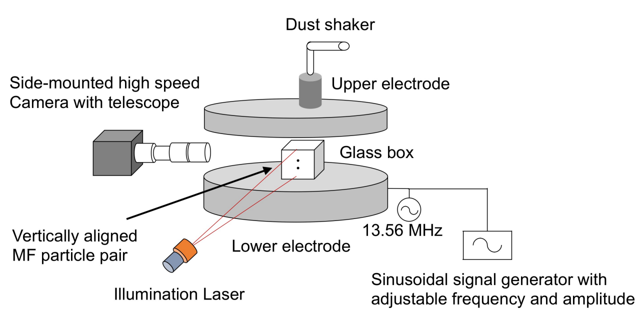

Figure 3.3. The sketch for the modified GEC RF reference cell built at CASPER.

A function generator coupled to the lower electrode through an 20 dB attenuator was employed to provide a sinusoidal driving force with adjustable frequency and amplitude to the dust pair. To study the response of the dust pair to the external excitation, a continuous frequency scan of the excitation signal was made to track the particles' motion at each excitation frequency. In order to obtain a full response curve that was useful for the purpose of studying the nonlinear grain-grain interaction, the frequency scan was designed to cover the natural resonance frequency of the sloshing and breathing modes (for measuring the primary responses) and half of the natural resonance frequency of the sloshing and breathing mode (for measuring the secondary, or super-harmonic, responses). Usually, a scan from 0 Hz to 50 Hz is enough to cover all the resonance frequencies of interest. As such, during each experimental measurement of the response curves, the excitation frequency was scanned over a desired region, but the excitation amplitude was fixed.

The motion of the particles was recorded by the side-mounted high speed camera working at a frame rate of 500 frames per second. As an example, Fig. 3.4 shows the particles' positions for a complete external excitation cycle (i.e., in one complete period T of the excitation). Depending on the external excitation frequency and the frame rate of the high speed camera, the total number of frames that can be retrieved in one excitation period is

$$N_{frames} = \frac{f_{camera}}{f_{excitation}}, \tag{3.1}$$

where f_{camera} is the frame rate of the high speed camera and $f_{excitation}$ is the frequency of the external excitation. For the example in Fig. 3.4, there are around 27 consecutive pictures taken in one excitation period at an excitation frequency of 18 Hz and a camera frame rate of 500 fps. In order to accurately retrieve information about the particles' periodic motion, this number of consecutive pictures taken in one period has to be large enough (at least 9 consecutive pictures) to provide a good resolution of the oscillating behavior. The exact position of each particle in a series of

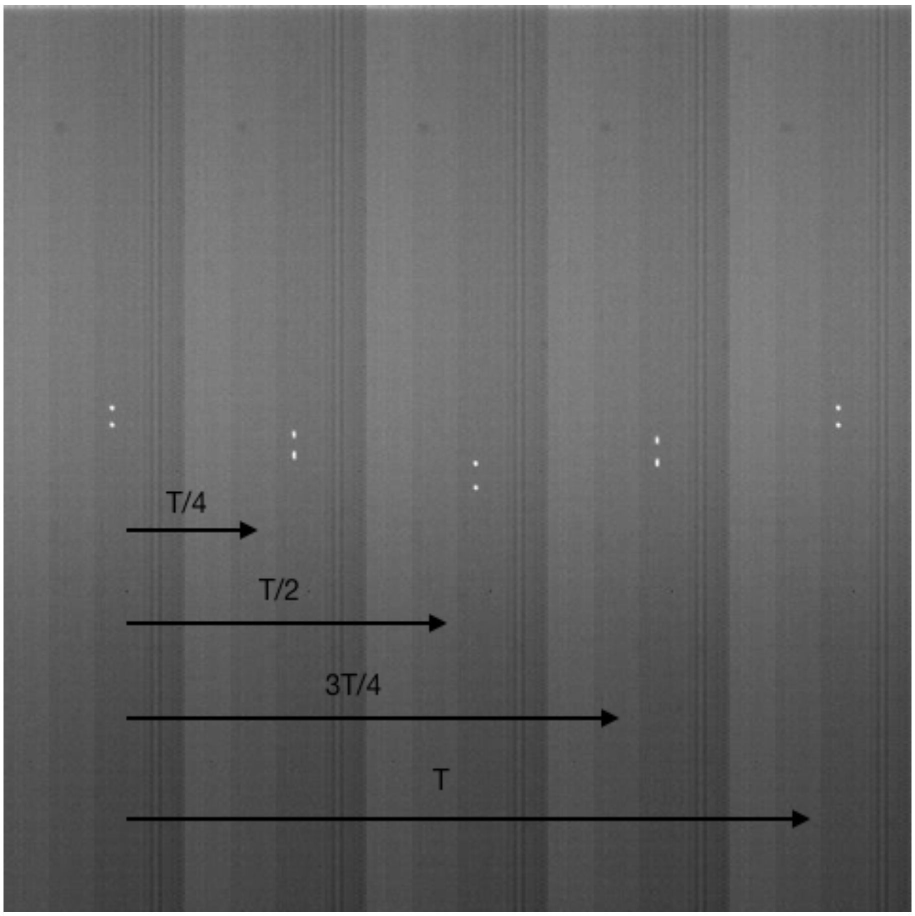

Figure 3.4: One complete period T of the motion of the externally driven dust pair. Experiment conditions: pressure at 40 mTorr, plasma power at 9.82 Watt, external sinusoidal excitation amplitude at 1 Volt and excitation frequency at 18 Hz. This excitation frequency is close to the sloshing mode resonance frequency.

consecutive pictures can be extracted using any standard particle tracking technique ('ParticleTracker' package in 'ImageJ' is used as the technique for particle tracking in our lab). As such, the particles' motion as a function of time can be retrieved for further study.

3.3 Scanning Mode Spectra

As illustrated in chapter two, this type of vertically aligned dust pair can be modeled as two coupled oscillators confined in the plasma sheath region. One direct experimental method of measuring the resonance frequency of each coupled mode is measuring the mode spectra.

In the classical normal mode spectra method [46–49], the Brownian motion of each particle around its equilibrium position is recorded as $\vec{r}_i(t)$, where i is the particle index. Based on this thermal fluctuation, each particle velocity is obtained as

$$\vec{v}_i(t) = [\vec{r}_i(t) - \vec{r}_i(t-1))] \times f_{camera}, \tag{3.2}$$

where f_{camera} is the frame rate of the high speed camera. Then the particle velocities are projected onto the normal mode vectors and are summed over the particles for each normal mode as follows,

$$v_l(t) = \sum_{i=1}^{N} \vec{v}_i(t) \cdot \vec{e}_{i,l}, \tag{3.3}$$

where l is the index of the normal vector, N is the total number of particles, and $\vec{e}_{i,l}$ is the ith component of the lth normal vector which can be theoretically derived from the Hessian matrix of the total energy of the system. Finally, the mode spectra (i.e., the spectra power density,) can be calculated as,

$$S_l(\omega) = \frac{2}{T} |\int_0^T v_l(t) e^{-i\omega t} dt|^2. \tag{3.4}$$

From the mode spectra, the energy distribution is mapped as a function of frequency for each normal mode, and the frequency with the greatest energy concentration is assumed to be the resonance frequency of the mode. This method is not limited by the number of particles in the system as long as the normal mode vectors can be exactly retrieved. This has been successfully applied to 2D dust crystal lattice with tens to hundreds of dust particles. This method heavily relies on the fact that the system yields orthogonal normal modes, so it is reasonable to apply to the 2D structure where the ion wake has a symmetric effect. However, for our vertically aligned pair structure, the particle-particle interaction is strongly perturbed by the ion wake and is non-reciprocal. Thus there are no longer orthogonal normal modes, which makes the classical normal mode spectra method unsuitable here.

To deal with the situation of non-reciprocal interactions, and more importantly to exactly measure the perturbed mode, we have extended the normal mode spectra method to accommodate the non-orthogonal mode analysis for a vertically aligned dust pair, using a method we call the 'Scanning Mode Spectra' [50].

In the 'Scanning Mode Spectra' (or SMS), we obtain the particle velocities in the same way as in the classical normal mode spectra method. But, rather than projecting the velocities onto theoretically calculated normal modes, we try all the possible modes. For example, the classical normal modes for two coupled oscillators are the antisymmetric mode (where both oscillators move in phase) and the symmetric mode (where both oscillators move 180 degrees out of phase). (Identical confinement and reciprocal interactions are assumed for simplicity.) These modes can be written generally as

$$\eta_i = \begin{bmatrix} x_1(t) \\ x_2(t) \end{bmatrix} = c \begin{bmatrix} a \\ b \end{bmatrix} e^{i\omega_i t + \phi_i}, \tag{3.5}$$

with $a = b$ for the antisymmetric mode and $a = -b$ for the symmetric mode. In the classical normal mode spectra method, we only project the particle velocities onto these two modes and obtain the spectra power density. However, in the Scanning

Mode Spectra method, we explore all the possible combination of a and b by setting

$$\begin{aligned} a &= cos(\psi), \\ b &= sin(\psi), \end{aligned} \tag{3.6}$$

where ψ is the polarization angle. By scanning ψ from 0 to π, we are able to retrieve all the possible modes, and the particle velocities are then projected onto all of these modes to get a continuous spectra power density map.

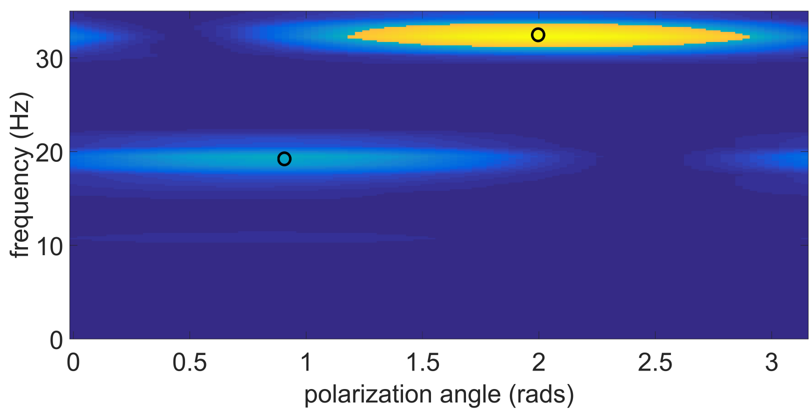

Figure 3.5: Scanning mode spectra for the particles' thermal motion.The sloshing mode frequency ω_- is approximately 18.5 Hz with polarization angle $\psi_- = 0.89$. The breathing mode frequency ω_+ is approximately 32 Hz with polarization angle $\psi_+ = 1.91$. Decoupling parameters can be determined by taking the cotangent of the polarizations, $a_- = cot(\psi_-)$ and $a_+ = cot(\psi_+)$.

As an example [43], the SMS for the vertical thermal motion of the particle pair is shown in Fig. 3.5 where the plasma power is 9.82 W, pressure 40 mTorr, and the scanning step for the polarization angle is $\Delta\psi = 0.01\pi$. Two maximum intensity spots in the SMS indicated by black circles mark the information of the exact mode found for the particle pair. From the definition of the polarization angle (Eq. 3.6), it is easy to tell that a mode is sloshing-like (particles move in phase) when the polarization angle is less than $\frac{\pi}{2}$, while it is breathing-like (particles move out of phase) when the polarization angle is greater than $\frac{\pi}{2}$. Thus, this first mode is a sloshing mode with a resonance frequency of $\omega_- = 18.5$ Hz. The polarization angle $\psi_- = 0.89$ of this mode obviously deviates from that of a classical antisymmetric mode $\psi_{antisymmetric} = \frac{\pi}{4}$. The second mode is a breathing mode with a resonance frequency of $\omega_+ = 32$ Hz and a polarization angle of $\psi_+ = 1.91$. Again, this polarization angle is different from the polarization angle for a classical symmetric mode $\psi_{symmetric} = \frac{3\pi}{4}$. With the polarization angle measured, the decoupling parameters α_- and α_+ (see Eq. 2.3) are in turned calculated to be $\alpha_- = cotan(\psi_-) = 0.81$ and $\alpha_+ = cotan(\psi_+) = -0.35$, which will be used for the later decoupling process.

Notice that, in this chapter, the study of nonlinear behavior is restricted to only the vertical direction, thus all the analysis, e.g., the SMS, are conducted by only analyzing the particle motion in the vertical direction. The SMS can be obtained in the same way for horizontal thermal motion and this will be discussed in a later chapter where the interaction between the vertical and the horizontal motion are considered.

The limitation of this method is clear in that it would become troublesome when the number of particles increases, i.e., the degrees of freedom increase. For a pair system with two degrees of freedom, the whole mode space can be easily explored in polar coordinates by the polar angle ψ. For a system with three degrees of freedom, the whole mode space can still be explored in spherical coordinates by assigning a polar angle ψ and an azimuthal angle ϕ where the displacement of each particle in the mode is $sin(\psi)cos(\phi)$, $sin(\psi)sin(\phi)$ and $cos(\psi)$, respectively. However, as the number of degrees of freedom goes beyond three, not only does the calculation of mode space become extremely complicated, but the visualization of the spectra map (more than three dimensions) becomes impossible. Thus, the SMS method has a good application for our system of two degrees of freedom, and would have a potential application for a three-particle system. For systems with higher degrees of freedom, the SMS method needs further modifications.

3.4 Decoupling Particles Motion

The particle motion is strongly coupled in that the motion of each particle contains the components of both of the modes simultaneously. Fig. 3.6 shows the typical motion of the particles with excitation in the vertical direction for both upstream and downstream particles. Fig. 3.7 shows the corresponding Fast Fourier Transformation (FFT) spectra.

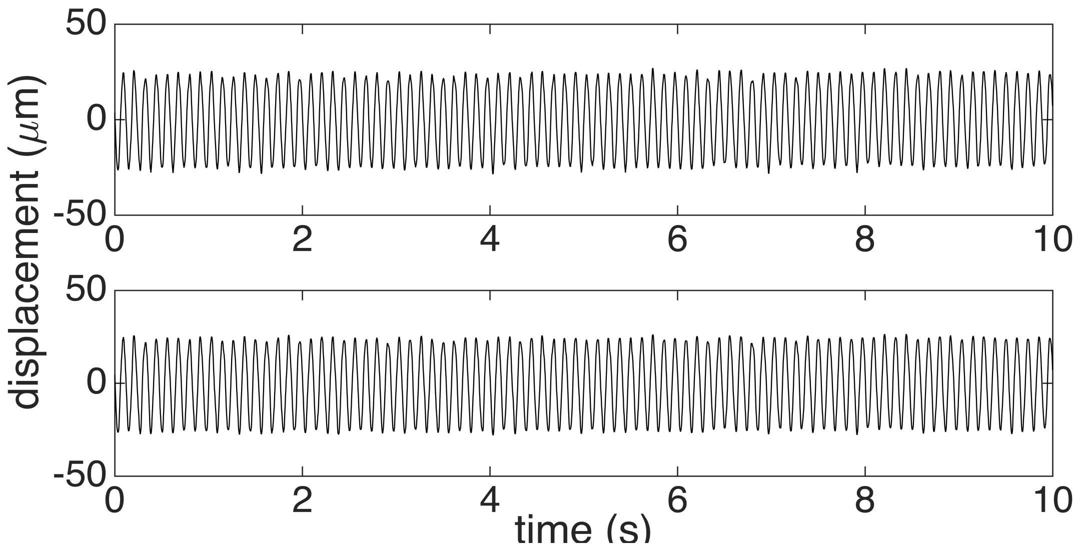

Figure 3.6: The time series of the original particles' motion in the vertical direction being driven by a 5 Hz external sinusoidal excitation. The motion of the upstream particle is shown in (a) and the motion of the downstream particle is shown in (b).

The FFT shows clearly that there is a cluster of peaks at around 18 Hz (enclosed by the red oval) and a cluster of peaks at around 32 Hz (enclosed by the green oval) corresponding to the sloshing and the breathing mode respectively. Due to this strong coupling, studying the nonlinear behavior directly in the original coordinates would be complicated.

However, as illustrated in chapter two, the particles' motion can be theoretically decoupled by conducting the transformation using Eq. 2.5. Applying the same approach, the time series of the particles' motion recorded from the experiment can also

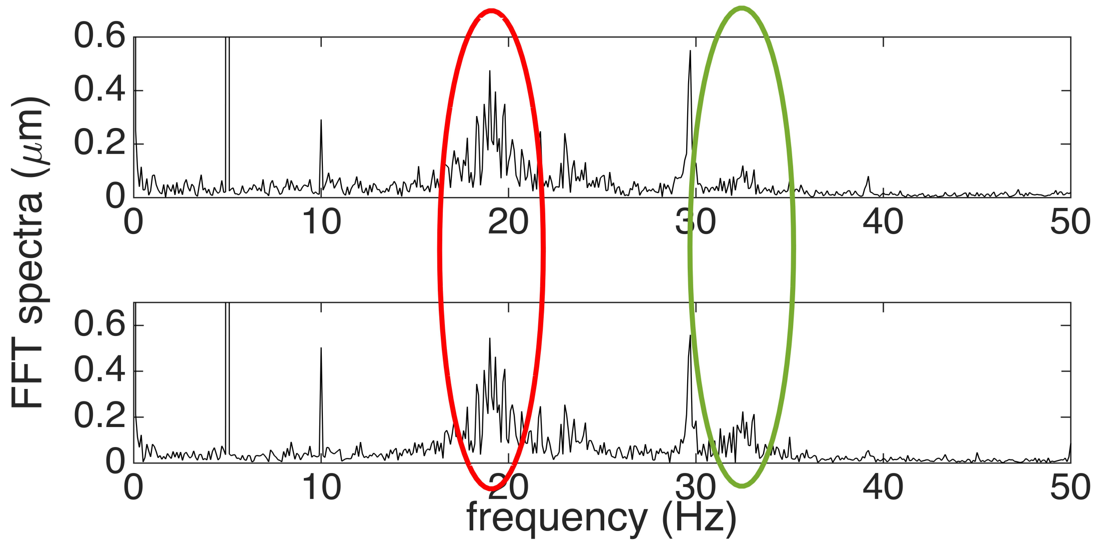

Figure 3.7: The Fast Fourier Transformation (FFT) spectra for the particles' motion in Fig. 3.6. The FFT for the upstream particle is shown in (a) and that for the downstream particle is shown in (b). The sloshing mode components are highlighted by the red oval, while the breathing mode components are highlighted by the green oval. There are also peaks appearing at 5 Hz and 10 Hz which are responses to the external excitation. The peak appearing at 30 Hz is considered as system noise that persists through the whole experiment.

be transferred into the decoupled coordinates by applying the transformation:

$$\begin{aligned} x_+(t) &= x_1(t) - \alpha_- x_2(t), \\ x_-(t) &= x_1(t) - \alpha_+ x_2(t), \end{aligned} \tag{3.7}$$

where α_- and α_+ are the decoupling parameters measured from the SMS.

Fig. 3.8 shows the particles motion transferred into the new coordinates, i.e., x_+ coordinate and x_- coordinate. To verify that the sloshing mode is indeed decoupled from the breathing mode, the FFT spectra are again measured in those two coordinates and are shown in Fig. 3.9. As shown, in the sloshing mode coordinate, i.e., the x_- coordinate (Fig. 3.9a), the breathing mode components (the cluster of peaks evident at 32 Hz) has been eliminated and only the sloshing mode components remain (the cluster of peaks at 18 Hz). Similarly, in the breathing mode coordinate, i.e., the x_+ coordinate (Fig. 3.9b), the sloshing mode component has been eliminated and the only the breathing mode components are left. The differences are highlighted by the red and green ovals. Therefore, the validity of the proposed decoupling process has been also confirmed by the experiments.

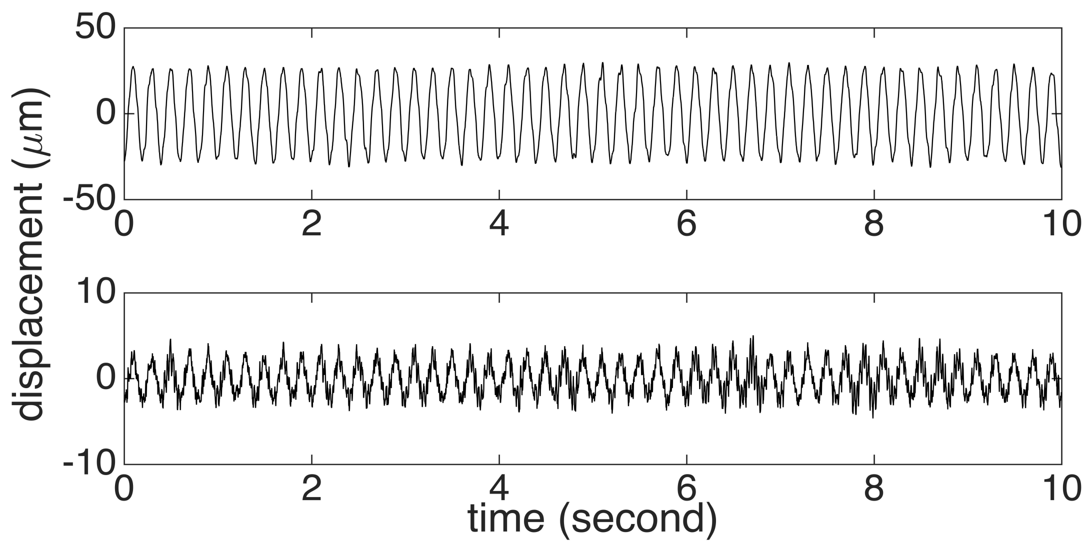

Figure 3.8: The oscillation motion in the decoupled sloshing and breathing coordinates by conducting the transformation in Eq. 3.7. The upper panel shows the motion in the sloshing mode coordinate (x_-) and the lower panel shows the motion in the breathing mode coordinate (x_+).

It is worthy to mention that traditional decoupling coordinates that have been widely used in a variety of fields are the center of mass coordinate and the relative displacement coordinate. A comparison between the proposed decoupling coordinates to these traditional decoupling coordinates is illustrated here. The traditional center of mass coordinate is $x_{com}(t) = x_1(t) + x_2(t)$, which is nothing but a perfect sloshing coordinate (a difference of a factor of $\frac{1}{2}$ is ignored) with $\alpha_+ = -1$ in Eq. 3.7. Likewise, the traditional relative coordinate is $x_{relative}(t) = x_1(t) - x_2(t)$, which is a perfect breathing coordinate (a difference of a factor of $\frac{1}{2}$ is ignored) with $\alpha_- = -1$ in Eq. 3.7. The FFT spectra of the particles' motion in these two traditional decoupling coordinates are also measured and are shown in Fig. 3.10.

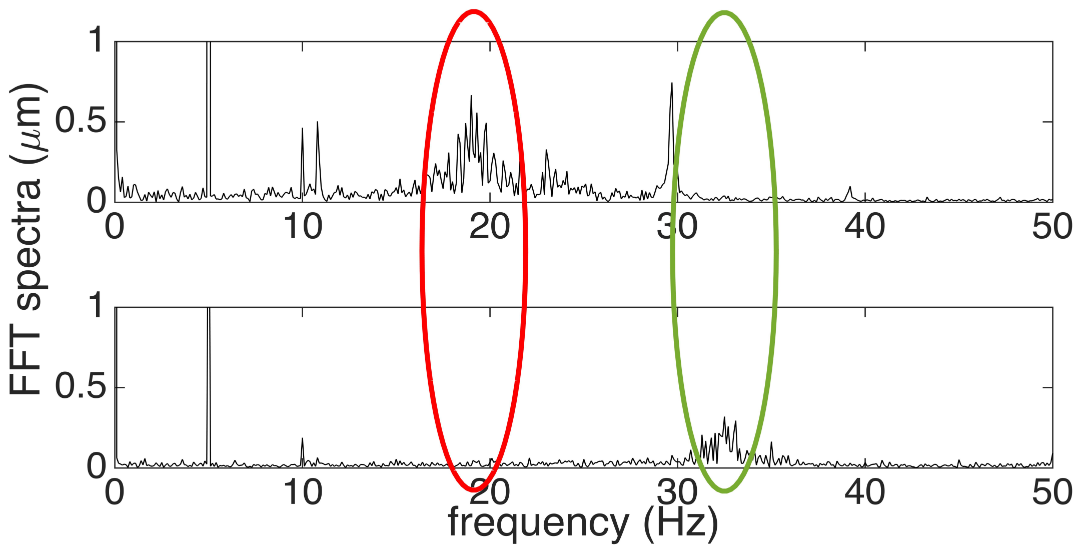

Figure 3.9: The corresponding FFTs for the oscillation motion in the decoupled coordinates in Fig. 3.8. a) the FFT for the motion in the sloshing mode coordinate. b) the FFT for the motion in the breathing mode coordinate. The sloshing and breathing mode components are highlighted by the red and green ovals, respectively.

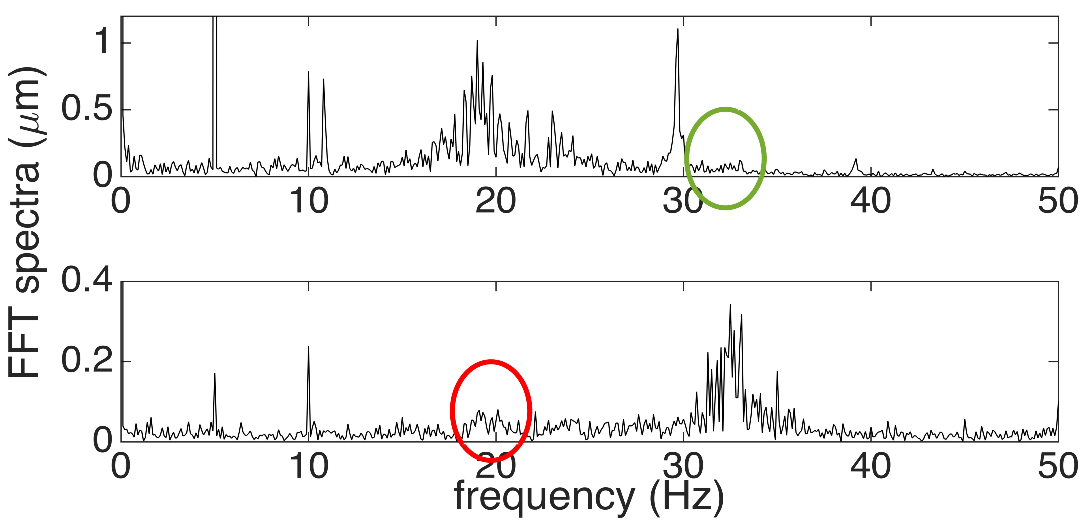

Figure 3.10: The FFTs for the traditional decoupling coordinates a) the center of mass coordinate and b) the relative coordinate. The undesired breathing mode components and sloshing mode components are highlighted by the green and red circles respectively.

Although these coordinates does an overall good job in decoupling the modes, there is still considerable response at the sloshing frequency for the relative coordinate (highlighted by the red circle), and considerable response at the breathing frequency for the center of mass coordinate (highlighted by the green circle). Since the traditional decoupling coordinates are originally designed for decoupling orthogonal normal modes with reciprocal coupling (interactions), their failure in completely decoupling non-orthogonal modes resulting from the non-reciprocal coupling is not unanticipated. As such, in order to achieve a more reliable decoupled motion for a dust pair with non-reciprocal interactions, the newly introduced sloshing and breathing coordinates are preferable.

3.5 Measuring the Amplitude-Frequency Response Curves from Experiment

One of the most fundamental methods used to study the nonlinear behavior is to analyze the amplitude-frequency response curves in response to an external excitation. The amplitude-frequency responses have already been theoretically derived in chapter two as the amplitudes of the response at desired frequencies. For example, $\frac{(\epsilon F_+)}{-\Omega^2+\omega_+^2}$ in Eq. 2.63 is the amplitude for the response at exactly the excitation frequency, which is also known as the primary response, and $\frac{g_1[C_1(\frac{\epsilon F_+}{-\Omega^2+\omega_+^2})-C_2(\frac{\epsilon F_-}{-\Omega^2+\omega_-^2})]^2}{\omega_+[(\epsilon\mu)^2+4(2\Omega-\omega_+)^2]^{\frac{1}{2}}}$ in Eq. 2.63 is the amplitude for the response at twice the excitation frequency, known as the secondary response (or more precisely, the super-harmonic response). As there should be a response at half of the excitation frequency, it will be designated as the sub-harmonic response, which we shall see in a later chapter where the interaction between the vertical and horizontal motion is considered.

In the experiment, the amplitude-frequency responses can either be directly measured in the original x_1 and x_2 coordinates, or be measured in the decoupled x_- and x_+ coordinates. Since our theoretical responses are derived in the decoupled coordinates, the experimental amplitude-response curves will also be measured in those coordinates.

To experimentally measure the amplitude-frequency responses, the particles' motion has to first be transformed into the decoupled sloshing mode coordinate and breathing mode coordinate. Then, the FFT spectra is calculated for the motion in each of these coordinates. Fig. 3.11 shows exactly the same FFT spectra as in Fig. 3.9, but on a logarithmic scale.

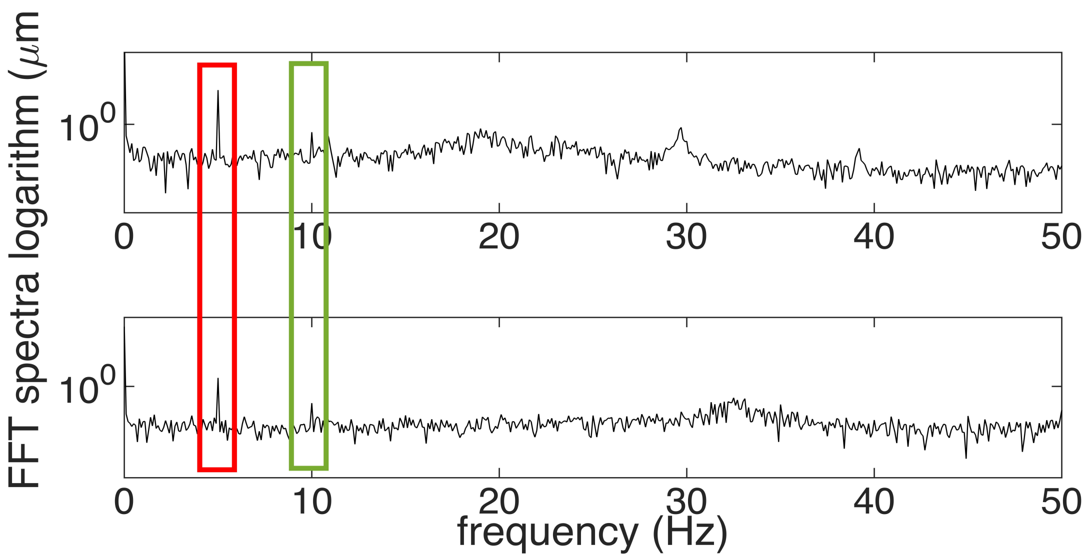

Figure 3.11: FFT spectra for oscillation motion in the decoupled coordinates with y axis in logarithm scale. The particle pair was driven by an external sinusoidal excitation at 5 Hz.

As shown by the red and green rectangles, there are strong peaks at 5 Hz and relatively weak peaks at 10 Hz. Since the frequency of the external sinusoidal excitation is 5 Hz, the height of the 5 Hz peak is measured to be the primary response amplitude and the height of the 10 Hz peak is measured to be the super-harmonic response amplitude for an excitation at 5 Hz. It is obvious in these logarithmic plots that the primary responses are larger than the super-harmonic responses by several orders of magnitude. This is because the super-harmonic responses are caused by the nonlinearities of the system, and the nonlinear effects are usually small compared to the linear effects. Small as the super-harmonic responses be, they are still detectable and can be clearly distinguished from the noise in the FFT spectra. This is promising for us to be able to study the nonlinearities in terms of the amplitude-frequency responses for dust pair in our GEC reference cell.

So far, we have showed an example of measuring responses at a specific excitation frequency. To obtain a continuous amplitude-frequency response curve, we need to drive the dust particle pair at many different excitation frequencies, and measure the corresponding response amplitude as a function of the excitation frequency.

It is important to mention here that the resolution of the FFT spectra should be greater than the resolution of the amplitude-frequency response curve,

$$\Delta f_{excitation} >= \frac{f_{camera}}{N_{frames}}, \tag{3.8}$$

where $\Delta f_{excitation}$ is the step of the scanning of the external excitation frequency, f_{camera} is the frame rate of the camera and N_{frames} is the total number of frame taken by the camera. For example, if we measure an amplitude-frequency response curve by varying the excitation frequency every 0.1 Hz with a frame rate fixed at 500 fps, then at least 5000 frames are required. Otherwise, the measurement of response from the FFT spectra would be less reliable. In addition, to ensure that the amplitude-frequency response curve covers the frequency region of interest, the frame rate of the camera has to be at least twice as large as the frequency of interest, since the FFT spectra is always 'mirrored'. For example, if we want to measure a response at 100 Hz (the height of the peak appearing at 100 Hz in the FFT spectra), the frame rate of the camera has to be larger than 200 fps.

3.6 Measuring the Coefficients of the Nonlinear Grain-Grain Interactions

(This work has been published in 'Nonlinear response of vertical paired structure in complex plasma', Ding *et al.*, Plasma Physics and Controlled Fusion [43].)

As explained in chapter two, the vertically aligned dust pair in the plasma sheath can be modeled as two coupled oscillators. If the grain-grain interaction were non-reciprocal and were considered in the nonlinear regime, the equations of motion will be described as Eq. 2.16. To better explain the model, a scheme of the model is shown in Fig. 3.12.

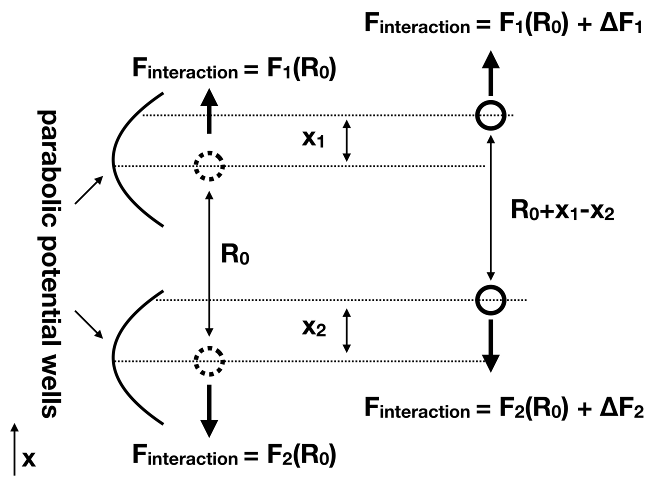

Figure 3.12: Scheme of the model for a vertically aligned dust particle pair in the plasma sheath region. The dust particles are trapped in parabolic potential wells $\phi = \frac{1}{2}m_{1(2)}\omega_{1(2)}^2 x_{1(2)}^2$. The subscripts 1 and 2 correspond to the upstream and downstream dust particle. The variation of the particle-particle interaction force due to the deviation from the equilibrium position is determined by $\Delta F_{1(2)} = -m_{1(2)}[k_{1(2)}(x_{1(2)} - x_{2(1)}) + k'_{1(2)}(x_{1(2)} - x_{2(1)})^2]$, where $k_{1(2)}$ and $k'_{1(2)}$ are related to the first and second derivative of the interaction force at the equilibrium inter-particle distance R_0 through $k_{1(2)} = F'_{1(2)}(R_0)/m_{1(2)}$ and $k'_{1(2)} = F''_{1(2)}(R_0)/2m_{1(2)}$. Here, the interaction force is not presumed to have any particular form.

The dust particles are separated by R_0 at the equilibrium positions (dashed circles) and are confined in parabolic potential wells $\phi = \frac{1}{2}m_{1(2)}\omega_{1(2)}^2 x_{1(2)}^2$ where $\omega_{1(2)}^2$ are known as the confinements due to the electrostatic forces in the plasma sheath and $x_{1(2)}$ are the displacements for the upstream and downstream dust particles. As the dust particles move away from the equilibrium positions (solid circles), the real time particle-particle spacing becomes $R = R_0 + x_1 - x_2$ where the positive x direction is upward. Since the particle-particle interaction forces are functions of particle-particle spacing, any change in the particle-particle spacing will change the interaction forces. Under the assumption that the inter-particle spacing has a small fluctuation around the equilibrium value R_0, i.e., $x_1 - x_2$ is small, which is valid in the entire experiment of scanning external excitation frequencies, the interaction forces can be Taylor expanded around the interaction forces at equilibrium $F_{1(2)}(R_0)$ as $F_{1(2)}(R_0)+\Delta F_{1(2)}$ where $\Delta F_{1(2)}$ contain the first and the second derivatives (any higher order derivatives are ignored) of the interaction force at equilibrium as:

$$\Delta F_{1(2)} = -[F'_{1(2)}(R_0)(x_{1(2)} - x_{2(1)}) + F''_{1(2)}(R_0)(x_{1(2)} - x_{2(1)})^2]. \tag{3.9}$$

Comparing Eq. 3.9 to the model Eq. 2.16, we find that k_1, k_2 and k'_1, k'_2 are nothing but the first and second derivatives of the interaction forces normalized by the particle mass as:

$$\begin{aligned} k_1 &= F'_1(R_0)/m_1, \\ k_2 &= F'_2(R_0)/m_2, \\ k'_1 &= F''_1(R_0)/2m_1, \\ k'_2 &= F''_2(R_0)/2m_2. \end{aligned} \tag{3.10}$$

As such, the quadratic nonlinear parts of the interaction forces (or the second derivatives of the interaction forces) can be determined by the measurements of k'_1 and k'_2.

To measure k'_1 and k'_2, we need first to measure the experimental primary response curves in the decoupled sloshing and breathing mode coordinates and to fit them to the theoretical responses derived in Eq. 2.41 and Eq. 2.44. To be more specific, the response curve at excitation frequencies around the resonance frequency of the breathing mode needs to be measured in the breathing mode coordinate and will be fitted to the response terms $\frac{-(\epsilon^2 F_+)}{\omega_+[(\epsilon\mu)^2+4(\Omega-\omega_+)^2)]^{\frac{1}{2}}}$ in Eq. 2.41. Likewise, for the response curve at excitation frequencies around the resonance frequency of the sloshing mode, it needs to be measured in the sloshing mode coordinate and will be fitted to the response terms $\frac{-(\epsilon^2 F_-)}{\omega_-[(\epsilon\mu)^2+4(\Omega-\omega_-)^2)]^{\frac{1}{2}}}$ in Eq. 2.44. By performing these fits, the excitation amplitudes in the decoupled coordinates $\epsilon^2 F_+$, $\epsilon^2 F_-$, the drag coefficient $\epsilon\mu$ and the resonance frequencies of each mode ω_+, ω_- can be measured.

It is noticed that even though the representation of the excitation amplitudes are different in different regions of interests, the exact value of the excitation amplitudes should be consistent over all regions. For example, in the primary breathing regions (i.e., excitation frequencies are around the resonance frequency of the breathing mode), the excitation amplitude in the breathing coordinate is represented as $\epsilon^2 F_+$ and that in the sloshing coordinate is represented as ϵF_- (see Eq. 2.21). While in the primary sloshing regions, the excitation amplitude in the breathing coordinate is represented as ϵF_+ and that in the sloshing coordinate is represented as $\epsilon^2 F_-$ (see Eq. 2.43). In spite of the difference in the representations, the excitation amplitudes in the decoupled coordinates should be consistent, i.e., the value of $\epsilon^2 F_+$ measured in the primary breathing mode coordinate is equal to the value of ϵF_+ measured in the primary sloshing mode coordinate, since the amplitude of the excitation signal is was fixed during the entire frequency scan. Similarly, the value of ϵF_- measured in the primary breathing mode coordinate is equal to the value of $\epsilon^2 F_-$ measured in the primary sloshing mode coordinate and this value is understood to be the amplitude of the excitation signal in the sloshing coordinate. Since we are fitting the breathing mode response curve in the primary breathing region and the sloshing mode response curve in the primary sloshing region, the amplitude of the excitation in the decoupled coordinates are represented by $\epsilon^2 F_+$ and $\epsilon^2 F_-$. For convenience, we introduce two new parameters F_+^* and F_-^* as the excitation amplitudes in the decoupled coordinates regardless of the region of interest for the frequency.

Fig. 3.13 shows the example fits of the experimental sloshing and breathing response curve to the theoretical ones in the primary sloshing and breathing regions, respectively, at a plasma power of 9.82 Watt and a pressure of 40 mTorr.

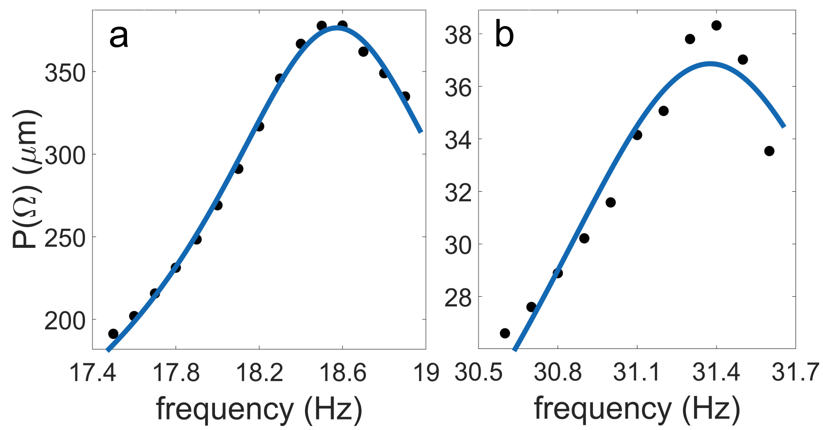

Figure 3.13: Primary response curves for (a) sloshing coordinate and (b) breathing coordinate. The points are experimental data while the lines are fits to the theoretical solution.

These fits yield a drag coefficient of $\epsilon\mu = 7.7\ s^{-1}$ within the primary sloshing region and $\epsilon\mu = 9.0\ s^{-1}$ for the primary breathing region, in agreement with the value of $\epsilon\mu = 8.5 \pm 0.9\ s^{-1}$. The resonance frequency for the breathing and the sloshing mode are 31.4 Hz and 18.5 Hz agreeing with the measurements from the Scanning Mode Spectrum Fig. 3.5. The absolute values for the amplitude in the decoupled coordinates $|F_+^*| = |\epsilon^2 f_+|$ and $|F_-^*| = |\epsilon^2 f_-|$ are determined to be $|F_+^*| = 0.67 \times 10^5 \mu m s^{-2}$ and $|F_-^*| = 3.34 \times 10^5 \mu m s^{-2}$, respectively.

Before we move forward to measuring k_1' and k_2', we need to figure out whether the excitation in the decoupled coordinates are in phase or out of phase, i.e., whether F_+^* and F_-^* are of the same sign or of different signs. The determination of the relative phase between the decoupled breathing and sloshing excitation is important not only because that we need this relative phase in the following fits for the secondary regions, but also that this can be used to determine the relative amplitude of the original excitation on the upstream and downstream dust particle.

To determine the relative phase of the excitations in the decoupled coordinates, we look at the equations of motion only in the linear regime as in Eq. 2.14

$$\begin{aligned} \ddot{x}_1 + \mu\dot{x}_1 + \omega_1^2 x_1 + k_1(x_1 - x_2) &= F_1 e^{i\Omega t} + C.C., \\ \ddot{x}_2 + \mu\dot{x}_2 + \omega_2^2 x_2 + k_2(x_2 - x_1) &= F_2 e^{i\Omega t} + C.C.. \end{aligned} \tag{3.11}$$

Instead of in the decoupled coordinates as illustrated in chapter two, these equations of motion can also be directly solved in the original x_1 and x_2 coordinates (thanks to the linearity of these equations). If we define a parameter $R = \frac{x_1}{x_2}$ as the ratio between the response amplitudes of the upstream and downstream particle, we can derive R by solving Eq. 3.11 as

$$\begin{aligned} R = &\frac{\{[F_1(-\Omega^2 + k_2 + \omega_2^2) + k_1 F_2][F_2(-\Omega^2 + k_1 + \omega_1^2) + k_2 F_1] + \mu^2\Omega^2 F_1 F_2\}}{[F_2(-\Omega^2 + k_1 + \omega_1^2) + k_2 F_1]^2 + (\mu\Omega F_2)^2} \\ &+ i\mu\Omega \frac{\{F_1[F_2(-\Omega^2 + k_1 + \omega_1^2) + k_2 F_1] - F_2[F_1(-\Omega^2 + k_2 + \omega_2^2) + k_1 F_2]\}}{[F_2(-\Omega^2 + k_1 + \omega_1^2) + k_2 F_1]^2 + (\mu\Omega F_2)^2}. \end{aligned} \tag{3.12}$$

For simplification we drop the damping terms in Eq.3.12 ($\mu = 0$). This can be justified since the damping is of the same order of magnitude as the nonlinear force contribution. Therefore, neglecting the damping does not qualitatively affect the result. By doing so, the amplitude ratio now reduces to

$$R = \frac{\eta(-\Omega^2 + k_2 + \omega_2^2) + k_1}{(-\Omega^2 + k_1 + \omega_1^2) + \eta k_2}, \tag{3.13}$$

where $\eta = \frac{F_1}{F_2}$ is the relative amplitude of the excitation amplitudes in the original coordinates. Depending on the value of η, the region of excitation frequencies where the upstream particle has a larger oscillation motion than the downstream particle has, i.e., $R > 1$ (or $x_1 > x_2$), can be very different. This theoretical excitation frequency region Ω^2 where $R > 1$ is also found to depend on the parameters ω_1, ω_2, k_1 and k_2 as

$$\eta > 1:$$

$$\Omega^2 \in (-\infty, k_1 + \omega_1^2 + \eta k_2) \cup (\frac{\omega_1^2 - \eta\omega_2^2}{1 - \eta}, +\infty), \omega_1^2 - \omega_2^2 \leq \frac{1 - \eta}{\eta}(k_1 + \eta k_2),$$
$$\Omega^2 \in (-\infty, \frac{\omega_1^2 - \eta\omega_2^2}{1 - \eta}) \cup (k_1 + \omega_1^2 + \eta k_2, +\infty), \omega_1^2 - \omega_2^2 > \frac{1 - \eta}{\eta}(k_1 + \eta k_2),$$

$$1 > \eta > 0:$$

$$\Omega^2 \in (\frac{\omega_1^2 - \eta\omega_2^2}{1-\eta}, k_1 + \eta k_2 + \omega_1^2), \omega_1^2 - \omega_2^2 \leq \frac{1-\eta}{\eta}(k_1 + \eta k_2),$$

$$\Omega^2 \in (k_1 + \eta k_2 + \omega_1^2, \frac{\omega_1^2 - \eta\omega_2^2}{1-\eta}), \omega_1^2 - \omega_2^2 > \frac{1-\eta}{\eta}(k_1 + \eta k_2),$$

$$\eta = 1:$$

$$\Omega^2 \in (-\infty, k_1 + \eta k_2 + \omega_1^2), \omega_1 - \omega_2 < 0,$$

$$\Omega^2 \in (k_1 + \eta k_2 + \omega_1^2, +\infty), \omega_1 - \omega_2 > 0.$$

The relative phase of the excitation in the decoupled coordinates can now be determined by matching the experimental frequency region where $R > 1$ to the theoretical region, such that the correct relative phase will give the right theoretical frequency region that is consistent with the experimental observation. For example, if the excitation in decoupled coordinates from Fig. 3.13 is out of phase (i.e., F_+^* and F_-^* are of opposite signs), the excitation ratio in the original coordinates $\eta = \frac{F_1}{F_2} = 0.62$ can be calculated through Eq. 2.20 since we have already found $|F_+^*| = 0.67 \times 10^5 \mu m s^{-2}$ and $|F_-^*| = 3.34 \times 10^5 \mu m s^{-2}$, and is confirmed to be less than 1. While for the in-phase decoupled excitation (i.e., F_+^* and F_-^* are of the same sign), the excitation ratio $\eta = \frac{F_1}{F_2} = 1.1$ is greater than 1. By considering the parameters ω_1, ω_2, k_1 and k_2 that can be measured from the Scanning Mode Spectra, it is found that $\omega_1^2 - \omega_2^2$ is less than $\frac{1-\eta}{\eta}(k_1 + \eta k_2)$ for the out of phase decoupled excitations, in which case the frequency region where $R > 1$ is

$$\Omega^2 \in (\frac{\omega_1^2 - \eta\omega_2^2}{1-\eta}, k_1 + \eta k_2 + \omega_1^2), \tag{3.14}$$

corresponding to $\Omega \in$ (24 Hz, 30 Hz) for the same data set in Fig. 3.13. On the other hand, for the in phase decoupled excitations, $\omega_1^2 - \omega_2^2$ is greater than $\frac{1-\eta}{\eta}(k_1 + \eta k_2)$ leading to the frequency region where $R > 1$ being given by

$$\Omega^2 \in (-\infty, \frac{\omega_1^2 - \eta\omega_2^2}{1-\eta}) \cup (k_1 + \omega_1^2 + \eta k_2, +\infty), \tag{3.15}$$

corresponding to $\Omega \in (34 \text{ Hz}, +\infty)$ since the excitation frequency is always a positive value.

To determine the correct relative phase, we need the oscillation amplitudes for both the upstream and downstream particles. Fig. 3.14 shows the oscillation amplitudes for both dust particles under the same plasma conditions as those in Fig. 3.13.

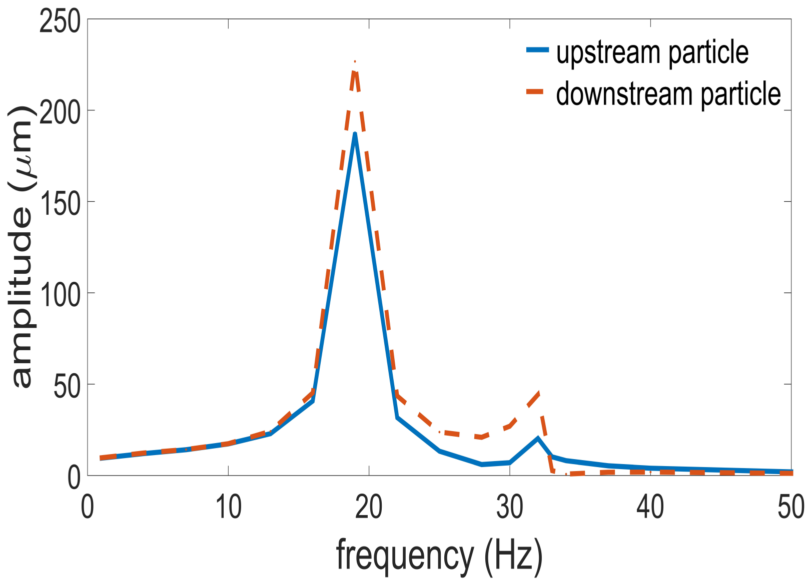

Figure 3.14: Experimental measurement of the oscillation amplitudes (primary responses) for both the upstream (blue solid line) and downstream particle (red dashed line).

It is obvious that the oscillation amplitude for the upstream particle (blue solid line) is greater than that for the downstream particle (red dashed line) when the excitation frequency is greater than 34 Hz, which is consistent with the situation that the excitations in the decoupled coordinates are in phase. Therefore, the excitations in the decoupled coordinates are found to be in phase by employing this method and excitation amplitudes in the original x_1 and x_2 coordinates are correspondingly found to be $\eta = 1.1$, indicating that the external excitation on the upstream particle is slightly greater than that of the downstream particle at a plasma power of 9.82 Watts and a pressure of 40 mTorr.

Noticed that in this method for determining the relative phase of the excitations in the decoupled coordinates, the nonlinearities are not considered and we derived the frequency region where $R > 1$ simply based on the linear mode of two coupled oscillators. This simplification is valid when the excitation amplitude is small such that the nonlinearities have little effect on the oscillation amplitudes. The maximum oscillation amplitude that appears at the sloshing resonance in this experiment is less than 250 μm, which is estimated to be approximately 2% of the total sheath width. The sheath edge is estimated to be at the plasma glow maxima. As such, the excitation amplitude can be considered as small enough that the simplification as a linear model for determining the relative phase of the decoupled excitation is valid (see the simulation section for more details).

With F_+^* and F_-^* now determined, the experimentally measured super-harmonic response curves can be fitted to the theoretically derived super-harmonic responses to measure the nonlinear coefficient for the interactions k_1' and k_2'. For example, in the secondary breathing region (i.e., the excitation frequencies are close to half of the resonance frequency of the breathing mode), the experimentally measured super-harmonic breathing response curve is fitted to $\frac{g_1[C_1(\frac{\epsilon F_+}{-\Omega^2+\omega_+^2})-C_2(\frac{\epsilon F_-}{-\Omega^2+\omega_-^2})]^2}{\omega_+[(\epsilon\mu)^2+4(2\Omega-\omega_+)^2]^{\frac{1}{2}}}$ in Eq. 2.63 where ϵF_+ and ϵF_- are understood to be the excitations in the decoupled coordinates F_+^* and F_-^* in the secondary breathing region.

Similarly, in the secondary sloshing region (i.e., the excitation frequencies are close to half of the resonance frequency of the sloshing mode) the experimentally measured super-harmonic sloshing response curve is fitted to $\frac{g_2[C_1(\frac{\epsilon F_+}{-\Omega^2+\omega_+^2})-C_2(\frac{\epsilon F_-}{-\Omega^2+\omega_-^2})]^2}{\omega_-[(\epsilon\mu)^2+4(2\Omega-\omega_-)^2]^{\frac{1}{2}}}$ in Eq. 2.70. The corresponding super-harmonic response fits are shown in Fig. 3.15.

From these fits, g_1 and g_2 can be measured and the nonlinear coefficients k_1', k_2' can be in turn determined through Eq. 2.18. For the data set used in Fig. 3.15, the corresponding nonlinear coefficients k_1', k_2' are equal to -253.4 $\mu m^{-1}s^{-2}$ and -364.6 $\mu m^{-1}s^{-2}$, respectively.

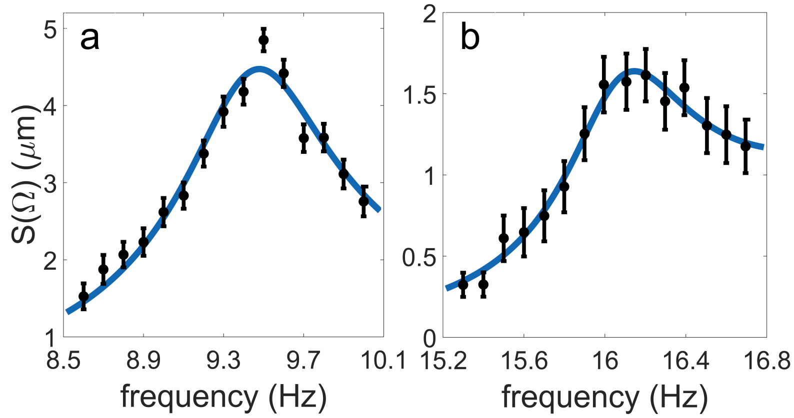

Figure 3.15: Fits for the measured secondary responses a) in the sloshing coordinate at $\frac{1}{2}\omega_-$ and b) breathing coordinate at $\frac{1}{2}\omega_+$ to the analytical response curves. The points show experimental data while the solid lines are fits using Eq. 2.63 and Eq. 2.70. The error-bars are due to the measurement uncertainty caused by the resolution of the camera which is 9 μm per pixel.

At this point, the coefficients of the nonlinear grain-grain interactions have been successfully measured. However, as can be seen in Fig. 3.15, the super-harmonic responses have the magnitudes of several micron-meters which are very small compared to the magnitudes of primary responses. As such, the reliability of this measurements on the small super-harmonic responses need to clarified and will be discussed in the next section.

3.7 Error and Linearity of the Measurement of the Super-Harmonic Responses

In the measurement of the nonlinear grain-grain interaction, the magnitude of the measured super-harmonic responses are several micrometers, which is smaller than the camera resolution (9 μm per pixel). The smallest response measured is around 0.5 μm, which is comparable to the wavelength (660 nm) of the illumination laser. As such, it is necessary to illustrate the validity and the linearity of the measurement for responses at the sub-pixel level.

A calibration was made for the measurement of secondary responses and primary responses at varying external excitation amplitudes at a plasma power of 9.82 Watts and a pressure of 40 mTorr, and is shown in Fig. 3.16 with dots as the response measurements and the blue lines as the linear fit lines.

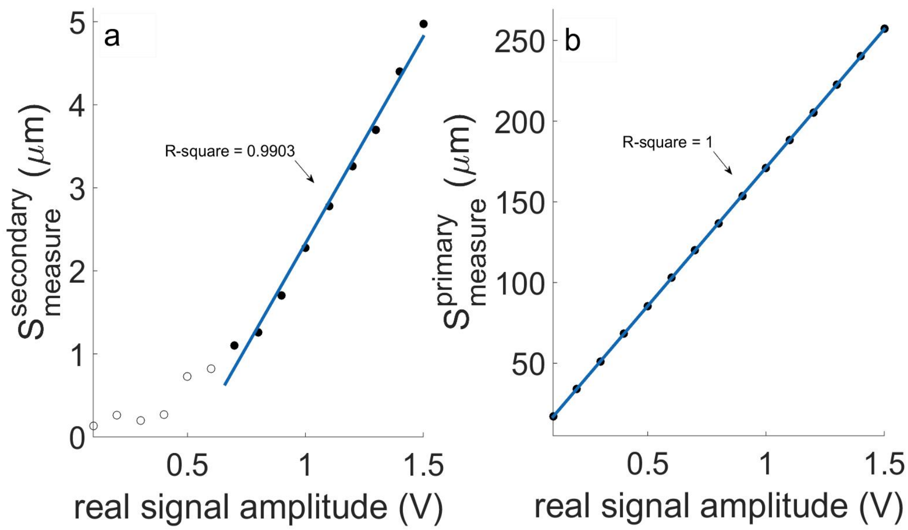

Figure 3.16: Calibration for a) the secondary response measurement and b) the primary response measurement.

As can be seen in Fig. 3.16a, for measurements greater than 1 μm (solid dots), there is a very good linear correlation ($R^2 = 0.9903$) between the measured responses and the amplitude of the external excitation signal. However, for those measurements less than 1 μm (open dots), the response become less linear with respect to the signal amplitude (especially those measurements below 0.5 μm). On the other hand, for large measurements (the primary responses in Fig. 3.16b), there is always a perfect linear correlation ($R^2 = 1$) between the response measurements and the signal amplitude. Therefore, this measurement of the responses at the sub-pixel level can be considered as a linear measurement of the true response (which is linear with respect to the amplitude of the real excitation signal) as long as the measurements are above 1 μm.

We have verified that this is a linear measurement of the true response above 1 μm, and now we need to explain why this measurement of response is not limited by the resolution of the camera and can capture the information at the sub-pixel level, which is beyond the resolution of the camera. As mentioned before, the responses are measured from the spectra of the Fourier transformation. This can be considered as a measurement of a collective oscillation pattern over a large number of periods rather than a single measurement of the exact oscillation displacement (which is of course restricted by the resolution of the camera). Notice that the frame rate here is 500 fps, corresponding to a period of 0.002 second, which is an order of magnitude less than the particle oscillation period. In this case, the overall oscillation pattern can be retrieved to a good accuracy. As long as the peaks in the FFT spectra can be clearly distinguished from the background noise, the responses can be measured beyond the resolution of the camera.

In spite of the ability to measure responses beyond the resolution of the camera, the uncertainty induced by the camera resolution needs additional attention, especially when the magnitude of the measurement is smaller than the camera resolution. The camera resolution cannot be simply used as the uncertainty of the measurement of the response since the responses are not measured in the space domain (directly from the particle oscillation displacement) but in the frequency domain (FFT spectra). In this case, we estimate the uncertainty of the measurement by conducting the following numerical experiment.

For each excitation frequency Ω, we assume that the true oscillation is represented by the summation of the measured primary response component and the measured super-harmonic response component as

$$x(t) = Psin(2\pi\Omega t) + Ssin(4\pi\Omega t). \tag{3.16}$$

The camera resolution comes in as an uncertainty by adding a random variable to Eq. 3.16 obeying a Gaussian distribution with zero mean and a standard deviation that equals to the camera resolution. In this case, the oscillation motion can be simulated at the same sampling rate as the frame rate of the camera as

$$x(t) = Psin(2\pi\Omega t) + Ssin(4\pi\Omega t) + \mathcal{N}(t), \tag{3.17}$$

where $\mathcal{N}(t) \sim \mathcal{N}(\mu, \sigma^2)$ is the Gaussian distributed random variable with $\mu = 0$ and σ equal to the camera resolution, and $t = [0 : 0.002 : 10]$ is the time span of 10 seconds in increments of 0.002 second, consistent with the frame rate of the camera (500 fps). We then measure the super-harmonic response from the simulated oscillation motion by employing the same method as for the real experimental data and record the measurement as one trial. We repeat this process 500 times and measure the standard error for the super-harmonic response for the combined 500 simulation trials. This standard error is considered as the uncertainty induced by the camera resolution for the experimentally measured super-harmonic response at an excitation frequency Ω. For the primary response, the uncertainty induced by the camera resolution is negligible since the magnitude of the response is much larger than the camera resolution.

CHAPTER FOUR

Dust Particle Pair Modeled as Two Dimensional Nonlinearly Coupled Oscillators

So far we have studied a vertically aligned dust particle pair and modeled this as coupled oscillators moving in the vertical direction. However, a more realistic model would be to allow the dust particles to move both in the vertical and horizontal directions, which will be discussed in this chapter. Due to the geometrical symmetry of the system in the horizontal direction, the preferred axis for the horizontal direction is chosen as the axis along which the dust particles actually move. As such, the dust particle comprising the pair are modeled as two dimensional coupled oscillators with four degrees of freedom (i.e., each dust particle has two degrees of freedom). In this case, the particles' vertical motion can affect their horizontal motion, and vice versa. By allowing this type of interaction (considered to be in the nonlinear regime) between the vertical and horizontal motion, interesting phenomenon can be examined, such as the internal resonance which was first observed in dusty plasmas by Ding *et al.* [51].

4.1 Theoretical Model of Two Dimensional Nonlinearly Coupled Oscillators

To establish a two dimensional model for the dust particle pair, we first need to establish the particle-particle interaction forces. We assumed the particle-particle interaction forces are pure functions of the particle-particle spacing, and the interaction force from the downstream particle to the upstream particle is not identical to that from the upstream particle to the downstream particle due to the non-reciprocity of the system. As such, the interaction force from the downstream particle to the upstream particle will be denoted as $F_{du}(d)$ (where d is the real time particle-particle spacing), while the upstream particle to the downstream particle is denoted as $F_{ud}(d)$ and $F_{du}(d) \neq F_{ud}(d)$.

Fig. 4.1 shows the scheme of the model. The horizontal deviation of the upstream (downstream) particle is $x_{1(2)}$, while the vertical deviation of the upstream (downstream) particle is $y_{1(2)}$ with R is the inter-particle spacing at equilibrium.

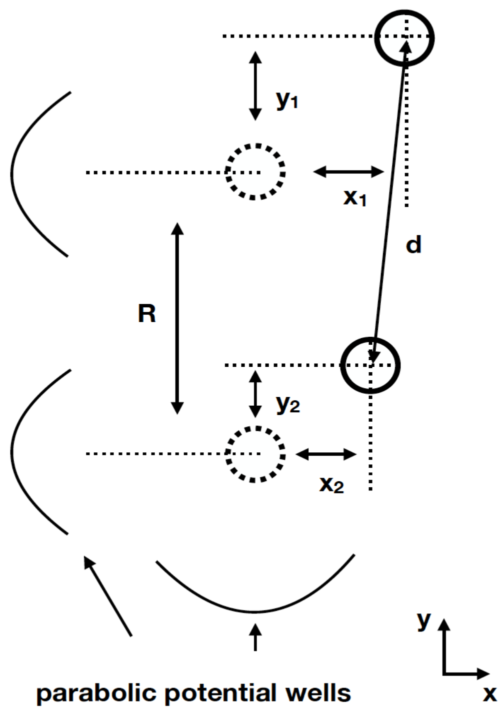

Figure 4.1. Scheme of the model for two-dimensional coupled oscillators.

We first look at the interaction force from the downstream particle to the upstream particle. By projecting this interaction force $F_{du}(d)$ onto the horizontal and vertical directions, we can write the horizontal component as $F^x_{du}(d) = F_{du}(d)\frac{x_1-x_2}{d}$ and the vertical component as $F^y_{du}(d) = F_{du}(d)\frac{R+y_1-y_2}{d}$, where the real time particle-particle spacing is $d = \sqrt{(x_1-x_2)^2+(y_1-y_2+R)^2}$. For convenience, we denote $X = x_1-x_2$ and $Y = y_1-y_2$, and the horizontal component and the vertical component take the form:

$$
\begin{aligned}
F_{du}^{x}(d) &= F_{du}(\sqrt{X^2+(R+Y)^2})\frac{X}{\sqrt{X^2+(R+Y)^2}},\\
F_{du}^{y}(d) &= F_{du}(\sqrt{X^2+(R+Y)^2})\frac{R+Y}{\sqrt{X^2+(R+Y)^2}}.
\end{aligned}
\tag{4.1}
$$

A multi-variable Taylor expansion can be conducted to expand these components to the quadratic terms at the equilibriums. The necessary derivatives that will be used in the Taylor expansion for the horizontal component F_{du}^{x} are:

$$
\begin{aligned}
\frac{\partial F_{du}^{x}}{\partial X} =& F'_{du}\frac{X^2}{[X^2+(R+Y)^2]} + F_{du}\frac{1}{[X^2+(R+Y)^2]^{\frac{1}{2}}} - F_{du}\frac{X^2}{[X^2+(R+Y)^2]^{\frac{3}{2}}},\\
\frac{\partial^2 F_{du}^{x}}{\partial X^2} =& F''_{du}\frac{X^3}{[X^2+(R+Y)^2]^{\frac{3}{2}}} + F'_{du}\{\frac{X}{[X^2+(R+Y)^2]} - \frac{3X^3}{[X^2+(R+Y)^2]^2}\}\\
&+ F_{du}\{\frac{3X^3}{[X^2+(R+Y)^2]^{\frac{5}{2}}} - \frac{3X}{[X^2+(R+Y)^2]^{\frac{3}{2}}}\},\\
\frac{\partial F_{du}^{x}}{\partial Y} =& F'_{du}\frac{X(R+Y)}{[X^2+(R+Y)^2]} - F_{du}\frac{X(R+Y)}{[X^2+(R+Y)^2]^{\frac{3}{2}}},\\
\frac{\partial^2 F_{du}^{x}}{\partial Y^2} =& F''_{du}\frac{X(R+Y)^2}{[X^2+(R+Y)^2]^{\frac{3}{2}}} + F'_{du}\{\frac{X}{[X^2+(R+Y)^2]} - \frac{3X(R+Y)^2}{[X^2+(R+Y)^2]^2}\\
&- F_{du}\{\frac{X}{[X^2+(R+Y)^2]^{\frac{3}{2}}} + \frac{3X(R+Y)^2}{[X^2+(R+Y)^2]^{\frac{5}{2}}}\}\\
,\frac{\partial^2 F_{du}^{x}}{\partial X\partial Y} =& F''_{du}\frac{X^2(R+Y)}{[X^2+(R+Y)^2]^{\frac{3}{2}}} + F'_{du}\{\frac{(R+Y)}{[X^2+(R+Y)^2]} - \frac{3X^2(R+Y)}{[X^2+(R+Y)^2]^2}\\
&+ F_{du}\{\frac{3X^2(R+Y)}{[X^2+(R+Y)^2]^{\frac{5}{2}}} - \frac{(R+Y)}{[X^2+(R+Y)^2]^{\frac{3}{2}}}\},
\end{aligned}
\tag{4.2}
$$

while those for the vertical component are:

$$
\begin{aligned}
\frac{\partial F^y_{du}}{\partial X} =& F'_{du}\frac{X(R+Y)}{[X^2+(R+Y)^2]} - F_{du}\frac{X(R+Y)}{[X^2+(R+Y)^2]^{\frac{3}{2}}},\\
\frac{\partial^2 F^y_{du}}{\partial X^2} =& F''_{du}\frac{X^2(R+Y)}{[X^2+(R+Y)^2]^{\frac{3}{2}}} + F'_{du}\{\frac{(R+Y)}{[X^2+(R+Y)^2]} - \frac{3X^2(R+Y)}{[X^2+(R+Y)^2]^2}\}\\
&+ F_{du}\{\frac{3X^2(R+Y)}{[X^2+(R+Y)^2]^{\frac{5}{2}}} - \frac{(R+Y)}{[X^2+(R+Y)^2]^{\frac{3}{2}}}\},\\
\frac{\partial F^y_{du}}{\partial Y} =& F'_{du}\frac{(R+Y)^2}{[X^2+(R+Y)^2]} + F_{du}\{\frac{1}{[X^2+(R+Y)^2]^{\frac{1}{2}}} - \frac{(R+Y)^2}{[X^2+(R+Y)^2]^{\frac{3}{2}}}\},\\
\frac{\partial^2 F^y_{du}}{\partial Y^2} =& F''_{du}\frac{(R+Y)^3}{[X^2+(R+Y)^2]^{\frac{3}{2}}} + F'_{du}\{\frac{3(R+Y)}{[X^2+(R+Y)^2]} - \frac{3(R+Y)^3}{[X^2+(R+Y)^2]^2}\\
&- F_{du}\{\frac{3(R+Y)}{[X^2+(R+Y)^2]^{\frac{3}{2}}} - \frac{3(R+Y)^3}{[X^2+(R+Y)^2]^{\frac{5}{2}}}\}\\
,\frac{\partial^2 F^y_{du}}{\partial X \partial Y} =& F''_{du}\frac{X(R+Y)^2}{[X^2+(R+Y)^2]^{\frac{3}{2}}} + F'_{du}\{\frac{X}{[X^2+(R+Y)^2]} - \frac{3X(R+Y)^2}{[X^2+(R+Y)^2]^2}\\
&+ F_{du}\{\frac{3X(R+Y)^2}{[X^2+(R+Y)^2]^{\frac{5}{2}}} - \frac{X}{[X^2+(R+Y)^2]^{\frac{3}{2}}}\},
\end{aligned}
\tag{4.3}
$$

where F'_{du} and F''_{du} are the first and second derivative of the force $F_{du}(d)$ with respect to inter-particle spacing d. The corresponding Taylor expansion at the equilibrium point that $(X = Y = 0)$ for the horizontal interaction force yields:

$$
\begin{aligned}
F^x_{du}(d) =& F^x_{du}|_{(0,0)} + \frac{\partial F^x_{du}}{\partial X}|_{(0,0)}X + \frac{\partial F^x_{du}}{\partial Y}|_{(0,0)}Y + \frac{1}{2}\frac{\partial^2 F^x_{du}}{\partial X^2}|_{(0,0)}X^2 + \frac{1}{2}\frac{\partial^2 F^x_{du}}{\partial Y^2}|_{(0,0)}Y^2\\
&+ \frac{\partial^2 F^x_{du}}{\partial X \partial Y}|_{(0,0)}XY\\
=& \frac{F_{du}(R)}{R}(x_1 - x_2) + (\frac{F'_{du}(R)}{R} - \frac{F_{du}(R)}{R^2})(x_1 - x_2)(y_1 - y_2),
\end{aligned}
\tag{4.4}
$$

while the Taylor expansion of the vertical interaction force yields:

$$\begin{aligned}F^y_{du}(d) =& F^y_{du}|_{(0,0)} + \frac{\partial F^y_{du}}{\partial X}|_{(0,0)}X + \frac{\partial F^y_{du}}{\partial Y}|_{(0,0)}Y + \frac{1}{2}\frac{\partial^2 F^y_{du}}{\partial X^2}|_{(0,0)}X^2 + \frac{1}{2}\frac{\partial^2 F^y_{du}}{\partial Y^2}|_{(0,0)}Y^2 \\ &+ \frac{\partial^2 F^y_{du}}{\partial X \partial Y}|_{(0,0)}XY \\ =& F_{du}(R) + F'_{du}(R)(y_1 - y_2) + \frac{1}{2}[\frac{F'_{du}(R)}{R} - \frac{F_{du}(R)}{R^2}](x_1 - x_2)^2 \\ &+ \frac{1}{2}F_{du}(R)''(y_1 - y_2)^2.\end{aligned} \tag{4.5}$$

As can be seen, due to the geometry of the vertical pair system, the horizontal component of the interaction force is different from the vertical component such that for the horizontal component the quadratic term is the mixed derivative $(\frac{F'_{du}(R)}{R} - \frac{F_{du}(R)}{R^2})(x_1 - x_2)(y_1 - y_2)$, while for the vertical component, the quadratic terms are the self derivatives $\frac{1}{2}[\frac{F'_{du}(R)}{R} - \frac{F_{du}(R)}{R^2}](x_1 - x_2)^2$ and $\frac{1}{2}F_{du}(R)''(y_1 - y_2)^2$.

The interaction force from the upstream particle to the downstream particle can be derived in the same way. In this case, the horizontal component of this interaction force $F^x_{ud}(d)$ takes the form

$$F^x_{ud}(d) = \frac{F_{ud}(R)}{R}(x_2 - x_1) + (\frac{F_{ud}(R)}{R^2} - \frac{F'_{ud}(R)}{R})(x_2 - x_1)(y_2 - y_1), \tag{4.6}$$

and the vertical component $F^y_{ud}(d)$ is

$$\begin{aligned}F^y_{ud}(d) =& - F_{ud}(R) + F'_{ud}(R)(y_2 - y_1) + \frac{1}{2}[\frac{F_{ud}(R)}{R^2} - \frac{F'_{ud}(R)}{R}](x_2 - x_1)^2 \\ &- \frac{1}{2}F_{ud}(R)''(y_2 - y_1)^2.\end{aligned} \tag{4.7}$$

As such, the equations of motion for two dimensional coupled oscillators under vertical excitation can be derived as

$$
\begin{aligned}
&\ddot{x}_1 + \mu\dot{x}_1 + \omega_{x1}^2 x_1 + k_{x1}(x_1 - x_2) + M_1(x_1 - x_2)(y_1 - y_2) = 0,\\
&\ddot{x}_2 + \mu\dot{x}_2 + \omega_{x2}^2 x_2 + k_{x2}(x_2 - x_1) + M_2(x_2 - x_1)(y_2 - y_1) = 0,\\
&\ddot{y}_1 + \mu\dot{y}_1 + \omega_{y1}^2 y_1 + k_{y1}(y_1 - y_2) + L_1(x_1 - x_2)^2 + G_1(y_1 - y_2)^2 = F_1 e^{i\Omega t} + C.C.,\\
&\ddot{y}_2 + \mu\dot{y}_2 + \omega_{y2}^2 y_2 + k_{y2}(y_2 - y_1) + L_2(x_2 - x_1)^2 + G_2(y_2 - y_1)^2 = F_2 e^{i\Omega t} + C.C.,
\end{aligned}
\tag{4.8}
$$

where ω_{x1}^2, ω_{x2}^2 are the horizontal confinements, ω_{y1}^2, ω_{y2}^2 are the vertical confinements and F_1, F_2 are the amplitude of the external excitation. And other parameters are connected to the particle-particle interaction forces through the following relationships:

$$
\begin{aligned}
k_{x1} =& -\frac{F_{du}(R)}{R},\\
k_{x2} =& -\frac{F_{ud}(R)}{R},\\
k_{y1} =& -F'_{du}(R),\\
k_{y2} =& -F'_{ud}(R),\\
M_1 =& \frac{F_{du}(R)}{R^2} - \frac{F'_{du}(R)}{R},\\
M_2 =& -(\frac{F_{ud}(R)}{R^2} - \frac{F'_{ud}(R)}{R}),\\
L_1 =& \frac{1}{2}[\frac{F_{du}(R)}{R^2} - \frac{F'_{du}(R)}{R}],\\
L_2 =& -\frac{1}{2}[\frac{F_{ud}(R)}{R^2} - \frac{F'_{ud}(R)}{R}],\\
G_1 =& -\frac{1}{2}F''_{du}(R),\\
G_2 =& \frac{1}{2}F''_{ud}(R).
\end{aligned}
\tag{4.9}
$$

In order to solve these equations of motion, we first transfer them into decoupled coordinates as we did before. Now, not only vertical direction but also the horizontal direction yields two modes, where we denote the polarization of the high frequency and low frequency mode in the horizontal direction α_+ and α_-, respectively. The polarization of the high frequency and low frequency mode in the vertical direction are denoted as β_+ and β_-, respectively. For now, we will avoid using sloshing or breathing modes since it is not always the case that there is a sloshing and a breathing mode, particularly for modes in the horizontal direction. Instead, we will use high frequency and low frequency modes to represent coupled modes in general. In this case, the decoupled coordinates are

$$\begin{aligned} x_+ &= x_1 - \alpha_- x_2, \\ x_- &= x_1 - \alpha_+ x_2, \\ y_+ &= y_1 - \beta_- y_2, \\ y_- &= y_1 - \beta_+ y_2. \end{aligned} \tag{4.10}$$

The corresponding equations of motion in decoupled coordinates yield:

$$\begin{aligned} &\ddot{x}_+ + \mu\dot{x}_+ + \omega_{x+}^2 x_+ + M_+(c_1x_+ + c_2x_-)(c_3y_+ + c_4y_-) = 0, \\ &\ddot{x}_- + \mu\dot{x}_- + \omega_{x-}^2 x_- + M_-(c_1x_+ + c_2x_-)(c_3y_+ + c_4y_-) = 0, \\ &\ddot{y}_+ + \mu\dot{y}_+ + \omega_{y+}^2 y_+ + L_+(c_1x_+ + c_2x_-)^2 + G_+(c_3y_+ + c_4y_-)^2 = F_+e^{i\Omega t} + C.C., \\ &\ddot{y}_- + \mu\dot{y}_- + \omega_{y-}^2 y_- + L_-(c_1x_+ + c_2x_-)^2 + G_-(c_3y_+ + c_4y_-)^2 = F_-e^{i\Omega t} + C.C., \end{aligned} \tag{4.11}$$

where ω_{x+}, ω_{x-}, ω_{y+} and ω_{y-} are the resonance frequencies of the horizontal high frequency mode, the horizontal low frequency mode, the vertical high frequency mode and the vertical low frequency mode, respectively. All other parameters in the model can be transferred through the following relationships:

$$
\begin{aligned}
M_+ =& M_1 - \alpha_- M_2, \\
M_- =& M_1 - \alpha_+ M_2, \\
L_+ =& L_1 - \beta_- L_2, \\
L_- =& L_1 - \beta_+ L_2, \\
G_+ =& G_1 - \beta_- G_2, \\
G_- =& G_1 - \beta_+ G_2, \\
F_+ =& F_1 - \beta_- F_2, \\
F_- =& F_1 - \beta_+ F_2,
\end{aligned}
\tag{4.12}
$$

and

$$
\begin{aligned}
c_1 =& \frac{\alpha_+ - 1}{\alpha_+ - \alpha_-}, \\
c_2 =& \frac{1 - \alpha_-}{\alpha_+ - \alpha_-}, \\
c_3 =& \frac{\beta_+ - 1}{\beta_+ - \beta_-}, \\
c_4 =& \frac{1 - \beta_-}{\beta_+ - \beta_-}.
\end{aligned}
\tag{4.13}
$$

With the equations of motion decoupled in the linear regime, we are now able to further attack them employing the multiple scale method. Here, we only look at the region where the external excitation is resonating at the vertical high frequency mode y_+ (i.e., the frequency of the external excitation is close to the resonance frequency of the vertical high frequency mode $\Omega \approx \omega_{y+} + \epsilon\delta_1$). As we shall see later, the internal resonance can be observed in this frequency region. Following the same approach as in chapter two, we accompany parameters with ϵ such that the excitation for the on-resonant oscillator will be appearing at the same order of ϵ as the nonlinearities and the neutral drag. As such, Eq. 4.11 can be rewritten as

$$\begin{aligned}
&\ddot{x}_+ + \epsilon\mu\dot{x}_+ + \omega_{x+}^2 x_+ + M_+(c_1x_+ + c_2x_-)(c_3y_+ + c_4y_-) = 0,\\
&\ddot{x}_- + \epsilon\mu\dot{x}_- + \omega_{x-}^2 x_- + M_-(c_1x_+ + c_2x_-)(c_3y_+ + c_4y_-) = 0,\\
&\ddot{y}_+ + \epsilon\mu\dot{y}_+ + \omega_{y+}^2 y_+ + L_+(c_1x_+ + c_2x_-)^2 + G_+(c_3y_+ + c_4y_-)^2 = \epsilon^2 F_+ e^{i\Omega t} + C.C.,\\
&\ddot{y}_- + \epsilon\mu\dot{y}_- + \omega_{y-}^2 y_- + L_-(c_1x_+ + c_2x_-)^2 + G_-(c_3y_+ + c_4y_-)^2 = \epsilon F_- e^{i\Omega t} + C.C.,
\end{aligned} \tag{4.14}$$

where $\epsilon\mu$ is understood to be the drag coefficient and $\epsilon^2 F_+$, ϵF_- are understood to be the amplitudes in the high frequency and low frequency decoupled coordinates, respectively. Notice that this ordering is valid only when the excitation frequency is close to the resonance frequency of the high frequency mode in the vertical direction, i.e., $\Omega \approx \omega_{y+} + \epsilon\delta_1$. The complex conjugate $C.C.$ will be hidden from now on for convenience.

As before, we introduce test solutions of the form

$$\begin{aligned}
x_+(t_0, t_1; \epsilon) &= \epsilon x_{+1}(t_0, t_1) + \epsilon^2 x_{+2}(t_0, t_1) + ...,\\
x_-(t_0, t_1; \epsilon) &= \epsilon x_{-1}(t_0, t_1) + \epsilon^2 x_{-2}(t_0, t_1) + ...,\\
y_+(t_0, t_1; \epsilon) &= \epsilon y_{+1}(t_0, t_1) + \epsilon^2 y_{+2}(t_0, t_1) + ...,\\
y_-(t_0, t_1; \epsilon) &= \epsilon y_{-1}(t_0, t_1) + \epsilon^2 y_{-2}(t_0, t_1) + ...,
\end{aligned} \tag{4.15}$$

where $t_0 = t$ and $t_1 = \epsilon t$. Substituting Eq. 4.15 into Eq. 4.14 and keeping only terms to second order of ϵ, yields

$$\begin{aligned}
&\epsilon\frac{\partial^2 x_{+1}}{\partial t_0^2} + \epsilon^2\frac{\partial^2 x_{+2}}{\partial t_0^2} + 2\epsilon^2\frac{\partial^2 x_{+1}}{\partial t_0 \partial t_1} + \epsilon^2\mu\frac{\partial x_{+1}}{\partial t_0} + \epsilon\omega_{x+}^2 x_{+1} + \epsilon^2\omega_{x+}^2 x_{+2}\\
&+ \epsilon^2 M_+[(c_1x_{+1} + c_2x_{-1})(c_3y_{+1} + c_4y_{-1})] = 0,
\end{aligned} \tag{4.16}$$

$$\begin{aligned}
&\epsilon\frac{\partial^2 x_{-1}}{\partial t_0^2} + \epsilon^2\frac{\partial^2 x_{-2}}{\partial t_0^2} + 2\epsilon^2\frac{\partial^2 x_{-1}}{\partial t_0 \partial t_1} + \epsilon^2\mu\frac{\partial x_{-1}}{\partial t_0} + \epsilon\omega_{x-}^2 x_{-1} + \epsilon^2\omega_{x-}^2 x_{-2}\\
&+ \epsilon^2 M_-[(c_1x_{+1} + c_2x_{-1})(c_3y_{+1} + c_4y_{-1})] = 0,
\end{aligned} \tag{4.17}$$

$$\epsilon\frac{\partial^2 y_{+1}}{\partial t_0^2}+\epsilon^2\frac{\partial^2 y_{+2}}{\partial t_0^2}+2\epsilon^2\frac{\partial^2 y_{+1}}{\partial t_0\partial t_1}+\epsilon^2\mu\frac{\partial y_{+1}}{\partial t_0}+\epsilon\omega_{y+}^2 y_{+1}+\epsilon^2\omega_{y+}^2 y_{+2}$$
$$+\epsilon^2 L_+(c_1x_{+1}+c_2x_{-1})^2+\epsilon^2 G_+(c_3y_{+1}+c_4y_{-1})^2=\epsilon^2F_+e^{i\Omega t}, \tag{4.18}$$

$$\begin{aligned}&\epsilon\frac{\partial^2 y_{-1}}{\partial t_0^2}+\epsilon^2\frac{\partial^2 y_{-2}}{\partial t_0^2}+2\epsilon^2\frac{\partial^2 y_{-1}}{\partial t_0\partial t_1}+\epsilon^2\mu\frac{\partial y_{-1}}{\partial t_0}+\epsilon\omega_{y-}^2 y_{-1}+\epsilon^2\omega_{y-}^2 y_{-2}\\&+\epsilon^2 L_-(c_1x_{+1}+c_2x_{-1})^2+\epsilon^2 G_-(c_3y_{+1}+c_4y_{-1})^2=\epsilon F_-e^{i\Omega t}.\end{aligned} \tag{4.19}$$

By equating Eq. 4.16 at the order of ϵ, we derive the equations of motion to first order of approximation as

$$\begin{aligned}&\frac{\partial^2 x_{+1}}{\partial t_0^2}+\omega_{x+}^2x_{+1}=0,\\&\frac{\partial^2 x_{-1}}{\partial t_0^2}+\omega_{x-}^2x_{-1}=0,\\&\frac{\partial^2 y_{+1}}{\partial t_0^2}+\omega_{y+}^2y_{+1}=0,\\&\frac{\partial^2 y_{-1}}{\partial t_0^2}+\omega_{y-}^2y_{-1}=F_-e^{i\Omega t},\end{aligned} \tag{4.20}$$

with the solution to first order of approximation being

$$\begin{aligned}&x_{+1}(t_0,t_1)=A_1(t_1)e^{i\omega_{x+}t_0},\\&x_{-1}(t_0,t_1)=A_2(t_1)e^{i\omega_{x-}t_0},\\&y_{+1}(t_0,t_1)=A_3(t_1)e^{i\omega_{y+}t_0},\\&y_{-1}(t_0,t_1)=A_4(t_1)e^{i\omega_{y-}t_0}+(\frac{F_-}{-\Omega^2+\omega_{y-}^2})e^{i\Omega t_0},\end{aligned} \tag{4.21}$$

where $A_1(t_1)$, $A_2(t_1)$, $A_3(t_1)$ and $A_4(t_1)$ are functions of slow time t_1, that will be solved using the solvability conditions.

The equations of motion to second order of ϵ yield

$$
\begin{aligned}
\frac{\partial^2 x_{+2}}{\partial t_0^2} + \omega_{x+}^2 x_{+2} =& -2\frac{\partial^2 x_{+1}}{\partial t_0 \partial t_1} - \mu\frac{\partial x_{+1}}{\partial t_0} - M_+[(c_1x_{+1}+c_2x_{-1})(c_3y_{+1}+c_4y_{-1})],\\
\frac{\partial^2 x_{-2}}{\partial t_0^2} + \omega_{x-}^2 x_{-2} =& -2\frac{\partial^2 x_{-1}}{\partial t_0 \partial t_1} - \mu\frac{\partial x_{-1}}{\partial t_0} - M_-[(c_1x_{+1}+c_2x_{-1})(c_3y_{+1}+c_4y_{-1})],\\
\frac{\partial^2 y_{+2}}{\partial t_0^2} + \omega_{y+}^2 y_{+2} =& -2\frac{\partial^2 y_{+1}}{\partial t_0 \partial t_1} - \mu\frac{\partial y_{+1}}{\partial t_0} - L_+(c_1x_{+1}+c_2x_{-1})^2 - G_+(c_3y_{+1}+c_4y_{-1})^2\\
&+ F_+e^{i\Omega t},\\
\frac{\partial^2 y_{-2}}{\partial t_0^2} + \omega_{y-}^2 y_{-2} =& -2\frac{\partial^2 y_{-1}}{\partial t_0 \partial t_1} - \mu\frac{\partial y_{-1}}{\partial t_0} - L_-(c_1x_{+1}+c_2x_{-1})^2 - G_-(c_3y_{+1}+c_4y_{-1})^2.
\end{aligned}
\tag{4.22}
$$

Inserting Eq. 4.18 into Eq. 4.19, we achieve

$$
\begin{aligned}
\frac{\partial^2 x_{+2}}{\partial t_0^2} + \omega_{x+}^2 x_{+2} =& -2i\omega_{x+}\frac{\partial A_1}{\partial t_1}e^{i\omega_{x+}t_0} - \mu i\omega_{x+}A_1e^{i\omega_{x+}t_0} - M_+[c_1c_3A_1A_3e^{i(\omega_{x+}+\omega_{y+})t_0}\\
&+ c_1c_4A_1A_4e^{i(\omega_{x+}+\omega_{y-})t_0} + c_2c_3A_2A_3e^{i(\omega_{x-}+\omega_{y+})t_0}\\
&+ c_2c_4A_2A_4e^{i(\omega_{x-}+\omega_{y-})t_0} + c_1c_3A_1\bar{A}_3e^{i(\omega_{x+}-\omega_{y+})t_0}\\
&+ c_1c_4A_1\bar{A}_4e^{i(\omega_{x+}-\omega_{y-})t_0} + c_2c_3A_2\bar{A}_3e^{i(\omega_{x-}-\omega_{y+})t_0}\\
&+ c_2c_4A_2\bar{A}_4e^{i(\omega_{x-}-\omega_{y-})t_0} + c_1c_4A_1Be^{i(\omega_{x+}-\Omega)t_0}\\
&+ c_2c_4A_2Be^{i(\omega_{x-}+\Omega)t_0} + c_1c_4\bar{A}_1Be^{i(-\omega_{x+}+\Omega)t_0}\\
&+ c_2c_4\bar{A}_2Be^{-\omega_{x-}+\Omega}t_0],
\end{aligned}
\tag{4.23}
$$

$$
\begin{aligned}
\frac{\partial^2 x_{-2}}{\partial t_0^2} + \omega_{x-}^2 x_{-2} = & -2i\omega_{x-}\frac{\partial A_2}{\partial t_1}e^{i\omega_{x-}t_0} - \mu i\omega_{x-}A_2 e^{i\omega_{x-}t_0} - M_-[c_1c_3A_1A_3e^{i(\omega_{x+}+\omega_{y+})t_0} \\
& + c_1c_4A_1A_4e^{i(\omega_{x+}+\omega_{y-})t_0} + c_2c_3A_2A_3e^{i(\omega_{x-}+\omega_{y+})t_0} \\
& + c_2c_4A_2A_4e^{i(\omega_{x-}+\omega_{y-})t_0} + c_1c_3A_1\bar{A}_3e^{i(\omega_{x+}-\omega_{y+})t_0} \\
& + c_1c_4A_1\bar{A}_4e^{i(\omega_{x+}-\omega_{y-})t_0} + c_2c_3A_2\bar{A}_3e^{i(\omega_{x-}-\omega_{y+})t_0} \\
& + c_2c_4A_2\bar{A}_4e^{i(\omega_{x-}-\omega_{y-})t_0} + c_1c_4A_1Be^{i(\omega_{x+}-\Omega)t_0} \\
& + c_2c_4A_2Be^{i(\omega_{x-}+\Omega)t_0} + c_1c_4\bar{A}_1Be^{i(-\omega_{x+}+\Omega)t_0} \\
& + c_2c_4\bar{A}_2Be^{-\omega_{x-}+\Omega}t_0],
\end{aligned}
\tag{4.24}
$$

$$
\begin{aligned}
\frac{\partial^2 y_{+2}}{\partial t_0^2} + \omega_{y+}^2 y_{+2} = & -2i\omega_{y+}\frac{\partial A_3}{\partial t_1}e^{i\omega_{y+}t_0} - \mu i\omega_{y+}A_3 e^{i\omega_{y+}t_0} - L_+[c_1^2A_1^2e^{2i\omega_{x+}t_0} \\
& + 2c_1c_2A_1A_2e^{i(\omega_{x+}+\omega_{x-})t_0} + 2c_1c_2A_1\bar{A}_2e^{i(\omega_{x+}-\omega_{x-})t_0} + c_2^2A_2^2e^{2i\omega_{x-}t_0} \\
& + c_1^2A_1\bar{A}_1 + c_2^2A_2\bar{A}_2] - G_+[c_3^2A_3^2e^{2i\omega_{y+}t_0} + 2c_3c_4A_3A_4e^{i(\omega_{y+}-\omega_{y-})t_0} \\
& + 2c_3c_4A_3\bar{A}_4e^{i(\omega_{y+}-\omega_{y-})t_0} + 2c_3c_4A_3Be^{i(\omega_{y+}+\Omega)t_0} \\
& + 2c_3c_4A_3\bar{B}e^{i(\omega_{y+}-\Omega)t_0} + c_4^2A_4^2e^{2i\omega_{y-}t_0} + 2c_4^2A_4Be^{i(\omega_{y-}+\Omega)t_0} \\
& + 2c_4^2A_4\bar{B}e^{i(\omega_{y-}-\Omega)t_0} + c_4^2B^2e^{2i\Omega t_0} + c_3^2A_3\bar{A}_3 + c_4^2A_4\bar{A}_4 + c_4^2B\bar{B}],
\end{aligned}
\tag{4.25}
$$

$$
\begin{aligned}
\frac{\partial^2 y_{-2}}{\partial t_0^2} + \omega_{y-}^2 y_{-2} = & - 2i\omega_{y-}\frac{\partial A_4}{\partial t_1}e^{i\omega_{y-}t_0} - \mu i\omega_{y-}A_4e^{i\omega_{y-}t_0} - L_-[c_1^2A_1^2e^{2i\omega_{x+}t_0} \\
& + 2c_1c_2A_1A_2e^{i(\omega_{x+}+\omega_{x-})t_0} + 2c_1c_2A_1\bar{A}_2e^{i(\omega_{x+}-\omega_{x-})t_0} + c_2^2A_2^2e^{2i\omega_{x-}t_0} \\
& + c_1^2A_1\bar{A}_1 + c_2^2A_2\bar{A}_2] - G_-[c_3^2A_3^2e^{2i\omega_{y+}t_0} + 2c_3c_4A_3A_4e^{i(\omega_{y+}-\omega_{y-})t_0} \\
& + 2c_3c_4A_3\bar{A}_4e^{i(\omega_{y+}-\omega_{y-})t_0} + 2c_3c_4A_3Be^{i(\omega_{y+}+\Omega)t_0} \\
& + 2c_3c_4A_3\bar{B}e^{i(\omega_{y+}-\Omega)t_0} + c_4^2A_4^2e^{2i\omega_{y-}t_0} + 2c_4^2A_4Be^{i(\omega_{y-}+\Omega)t_0} \\
& + 2c_4^2A_4\bar{B}e^{i(\omega_{y-}-\Omega)t_0} + c_4^2B^2e^{2i\Omega t_0} + c_3^2A_3\bar{A}_3 + c_4^2A_4\bar{A}_4 + c_4^2B\bar{B}],
\end{aligned}
\tag{4.26}
$$

where $B = (\frac{F_-}{-\Omega^2+\omega_{y-}^2})$ (see Eq. 4.21). At this point, we consider a possible commensurable relationship (i.e., when the resonance frequency of one mode is multiple times the resonance frequency of the other mode) between the high frequency modes in both directions as $\omega_{y+} = 2\omega_{x+} - \epsilon\delta_2$, which means that the resonance frequency of the high frequency mode in the vertical direction is close to twice the resonance frequency of the high frequency mode in the horizontal direction. The primary reason we consider this commensurable relationship is to derive a theoretical guideline for investigation of the possible internal resonance. Assuming $\omega_{y+} = 2\omega_{x+} - \epsilon\delta_2$, we are able to eliminate the secular terms in Eq. 4.23-4.26. Eliminating these secular terms, we arrive at

$$
-2i\omega_{x+}\frac{\partial A_1}{\partial t_1} - \mu i\omega_{x+}A_1 - M_+[c_1c_3\bar{A}_1A_3e^{-i\delta_2t_1} + c_1c_4\bar{A}_1Be^{i(\delta_1-\delta_2)t_1}] = 0, \tag{4.27}
$$

$$
-2i\omega_{x-}\frac{\partial A_2}{\partial t_1} - \mu i\omega_{x-}A_2 = 0, \tag{4.28}
$$

$$
-2i\omega_{y+}\frac{\partial A_3}{\partial t_1} - \mu i\omega_{y+}A_3 - L_+c_1^2A_1^2e^{i\delta_2t_1} + F_+e^{i\delta_1t_1} = 0, \tag{4.29}
$$

$$
-2i\omega_{y-}\frac{\partial A_4}{\partial t_1} - \mu i\omega_{y-}A_4 = 0. \tag{4.30}
$$

It is obvious that Eq. 4.28 and Eq. 4.30 are isolated (i.e., there are no coupling terms) and are of simple form yielding decay solutions

$$\begin{aligned} A_2 &= Ce^{-\frac{\mu}{2}t_1}, \\ A_4 &= C'e^{-\frac{\mu}{2}t_1}, \end{aligned} \tag{4.31}$$

where C and C' are constants determined by initial conditions.

On the other side, the existence of couplings makes it complicated to solve Eq. 4.27 and Eq. 4.29. Here, we introduce test solutions

$$\begin{aligned} A_1 &= a_1(t_1)e^{i\theta_1(t_1)}, \\ A_3 &= a_3(t_1)e^{i\theta_3(t_1)}, \end{aligned} \tag{4.32}$$

where a_1, a_3, θ_1 and θ_3 are all functions of slow time t_1. By plugging Eq. 4.32 into Eq. 4.27 and Eq. 4.29, we have

$$\begin{aligned} 0 =& - 2i\omega_{x+}(\frac{\partial a_1}{\partial t_1} + i\frac{\partial \theta_1}{\partial t_1}a_1) - \mu i\omega_{x+}a_1 - (M_+c_1c_3)a_1a_3e^{i(\theta_3-2\theta_1-\delta_2 t_1)} \\ & - (M_+c_1c_4)a_1Be^{i(\delta_1t_1-\delta_2t_1-2\theta_1)}, \end{aligned} \tag{4.33}$$

and

$$0 = - 2i\omega_{y+}(\frac{\partial a_3}{\partial t_1} + i\frac{\partial \theta_3}{\partial t_1}a_3) - \mu i\omega_{y+}a_3 - (L_+c_1^2)a_1^2e^{i(2\theta_1-\theta_3+\delta_2t_1)} + F_+e^{i(\delta_1t_1-\theta_3)}. \tag{4.34}$$

Separating the real and imaginary parts, we have

$$\begin{aligned} 0 =& 2\omega_{x+}\frac{\partial \theta_1}{\partial t_1}a_1 - (M_+c_1c_3)a_1a_3cos(\theta_3 - 2\theta_1 - \delta_2t_1) \\ & - (M_+c_1c_4)a_1Bcos(\delta_1t_1 - \delta_2t_1 - 2\theta_1), \\ 0 =& - 2\omega_{x+}\frac{\partial a_1}{\partial t_1} - \mu\omega_{x+}a_1 - (M_+c_1c_3)a_1a_3sin(\theta_3 - 2\theta_1 - \delta_2t_1) \\ & - (M_+c_1c_4)a_1Bsin(\delta_1t_1 - \delta_2t_1 - 2\theta_1), \end{aligned} \tag{4.35}$$

and

$$
\begin{aligned}
0 =& 2\omega_{y+}\frac{\partial\theta_3}{\partial t_1}a_3 - (L_+c_1^2)a_1^2cos(2\theta_1 - \theta_3 + \delta_2 t_1) \\
& + F_+cos(\delta_1 t_1 - \theta_3), \\
0 =& -2\omega_{y+}\frac{\partial a_3}{\partial t_1} - \mu\omega_{y+}a_3 - (L_+c_1^2)a_1^2sin(2\theta_1 - \theta_3 + \delta_2 t_1) \\
& + F_+sin(\delta_1 t_1 - \theta_3).
\end{aligned} \tag{4.36}
$$

We can solve Eq. 4.35 and Eq. 4.36 for steady state solutions by introducing two new parameters

$$
\begin{aligned}
\lambda_1 &= \theta_3 - 2\theta_1 - \delta_2 t_1, \\
\lambda_2 &= \delta_1 t_1 - \delta_2 t_1 - 2\theta_1.
\end{aligned} \tag{4.37}
$$

In order to obtain steady state solutions to Eq. 4.35 and Eq. 4.36, the derivatives of the parameters with respect to slow time t_1 need to be zero

$$
\begin{aligned}
\frac{\partial\lambda_1}{\partial t_1} &= 0, \\
\frac{\partial\lambda_2}{\partial t_1} &= 0, \\
\frac{\partial a_1}{\partial t_1} &= 0, \\
\frac{\partial a_3}{\partial t_1} &= 0.
\end{aligned} \tag{4.38}
$$

As such, Eq. 4.35 and Eq. 4.36 now become

$$
\begin{aligned}
0 =& \omega_{x+}(\delta_1 - \delta_2)a_1 - (M_+c_1c_3)a_1a_3cos(\lambda_1) - (M_+c_1c_4)a_1Bcos(\lambda_2), \\
0 =& -\mu\omega_{x+}a_1 - (M_+c_1c_3)a_1a_3sin(\lambda_1) - (M_+c_1c_4)a_1Bsin(\lambda_2),
\end{aligned} \tag{4.39}
$$

and

$$
\begin{aligned}
0 =& 2\omega_{y+}\delta_1 a_3 - (L_+c_1^2)a_1^2cos(\lambda_1) + F_+cos(\lambda_2 - \lambda_1), \\
0 =& -\mu\omega_{y+}a_3 + (L_+c_1^2)a_1^2sin(\lambda_1) + F_+sin(\lambda_2 - \lambda_1).
\end{aligned} \tag{4.40}
$$

The solutions to Eq. 4.39 and Eq. 4.40 can be divided into two categories, depending on whether a_1 is zero or not ($a_1 = 0$ or $a_1 \neq 0$).

When a_1 is zero ($a_1 = 0$), Eq. 4.40 will be reduced to

$$\begin{aligned} 0 =& 2\omega_{y+}\delta_1 a_3 + F_+ cos(\lambda_2 - \lambda_1), \\ 0 =& -\mu\omega_{y+} a_3 + F_+ sin(\lambda_2 - \lambda_1), \end{aligned} \tag{4.41}$$

in which case, the solutions of the steady state responses (a_1 and a_3) yield

$$\begin{aligned} a_1 =& 0, \\ a_3 =& (\frac{F_+}{4\omega_{y+}^2\delta_1^2 + \mu^2\omega_{y+}^2})^{\frac{1}{2}}. \end{aligned} \tag{4.42}$$

On the other hand, when a_1 is not equal to zero ($a_1 \neq 0$), the steady state responses (a_1 and a_3) are described by the following set of equations

$$\begin{aligned} 0 =& \omega_{x+}(\delta_1 - \delta_2) - (M_+ c_1 c_3) a_3 cos(\lambda_1) - (M_+ c_1 c_4) B cos(\lambda_2), \\ 0 =& -\mu\omega_{x+} - (M_+ c_1 c_3) a_3 sin(\lambda_1) - (M_+ c_1 c_4) B sin(\lambda_2), \\ 0 =& 2\omega_{y+}\delta_1 a_3 - (L_+ c_1^2) a_1^2 cos(\lambda_1) + F_+ cos(\lambda_2 - \lambda_1), \\ 0 =& -\mu\omega_{y+} a_3 + (L_+ c_1^2) a_1^2 sin(\lambda_1) + F_+ sin(\lambda_2 - \lambda_1). \end{aligned} \tag{4.43}$$

The solutions to the set of equations above are not in simple closed analytical form. Thus, the steady state responses a_1 and a_3 in Eq. 4.43 have to be solved using numerical methods. When the commensurable relationship is considered, the steady state responses under internal resonance switch between the solutions given in Eq. 4.42 and the solution governed by the set of equations shown in Eq. 4.43. It is also important to note that in Eq. 4.21, $A_1(t_1)$ is the response at ω_{x+} which is the resonance frequency of the horizontal high frequency mode. In this case, the response a_1 is understood to be the 'sub-harmonic' response since the excitation is around twice the resonance frequency of the horizontal high frequency mode, i.e., $\Omega \approx 2\omega_{x+}$.

4.2 Internal Resonances as a Phenomena of Nonlinear Dynamics

With these theoretical results in hands, we are now able to study the internal resonance phenomena first reported in dusty plasmas by Ding *et al.* [51].

Internal resonance as a phenomena of nonlinear dynamics, is a type of resonance created by nonlinear mode coupling in systems having multiple degrees of freedom. There is a wide application of internal resonance in various fields, such as mechanical energy harvesters [52–54], frequency stabilization [55], and nanomechanical systems [56, 57]. A system exhibits internal resonance whenever the natural frequency of any two modes satisfies a commensurable relation. In this case, there is a specific ratio (1:2, 1:3, etc) between the frequencies of the coupled modes, or there are specific equality relations among the resonance frequencies of more than two modes, e.g., the resonance frequency of one mode equals the sum of the resonance frequencies of two other modes [58]. Internal resonance can exist for cases with and without external excitations. In the presence of external excitations, the energy in the primary mode that is driven externally increases with increasing excitation amplitude until a saturation point is reached. Beyond this point, any additional energy is channeled to the secondary mode which is commensurate with the excited mode [59]. In the absence of external excitations, the energy oscillates between the two commensurate modes (with dissipation occuring in the presence of damping), resulting in a system that is continuously switching between the two modes.

4.3 Internal Resonances Observed in Dusty Plasma

(Portion of this work have been published in 'Nonlinear mode coupling and internal resonance observed in a dusty plasma', Ding *et al.*, New Journal of Physics [51].)

Internal resonance for a vertically aligned dust pair system has been observed employing the same experimental setup as the one described in chapter three, Fig. 3.1 and Fig. 3.2. The only differences is that in addition to the side mounted high speed camera, there is a second camera mounted on the top of the cell in order to track the horizontal motion of the dust particles (Fig. 4.2).

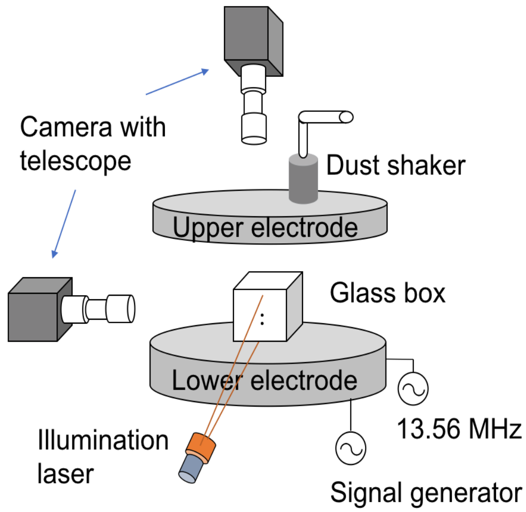

Figure 4.2: Sketch of the modified GEC RF reference cell with an additional high speed camera mounted on the top.

For a vertically aligned dust particle pair in plasma, the particle-particle interaction is non-reciprocal as discussed before. This non-reciprocity in the particle-particle interaction drives modes occurring in the horizontal direction to become two sloshing modes, while modes occurring in the vertically direction remain as both the sloshing and breathing type. For convenience, we will call the high frequency and low frequency mode in the horizontal direction, the S2 mode and the S1 mode, and the high frequency and low frequency mode in the vertical direction the B mode and the S mode.

To trigger the internal resonance in this pair system, a commensurable relation must be satisfied between the different modes, i.e., mode resonance frequencies have to be of a specific ratio. In order to determine this, we measured the resonance frequencies of each of the S1, S2, S and B mode under different plasma conditions. Fig. 4.3 shows the measured frequency for each of these modes at varying plasma powers and operating pressures.

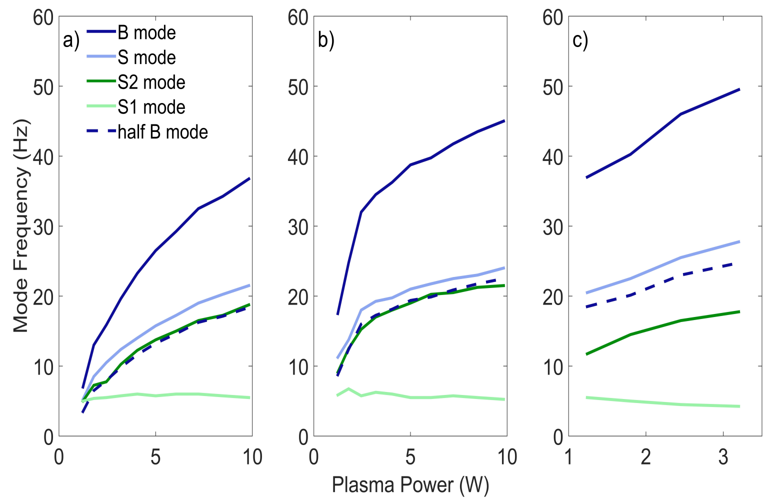

Figure 4.3: Mode frequencies as functions of plasma power at varying pressures a) 40 mTorr, b) 80 mTorr, c) 120 mTorr. Dark blue and light blue lines represent the vertical B and S modes, while dark green and light green lines show the horizontal S2 and S1 modes, respectively. The dashed blue line indicates $\frac{1}{2}$ of the frequency of the vertical B mode.

As shown in Fig. 4.3a and Fig. 4.3b, the frequency of the horizontal S2 mode (dark green line) is approximately equal to half that observed for the vertical breathing mode (dashed line) for low pressures (i.e., typically lower than 100 mTorr). At higher pressures (Fig. 4.3c), the S2 mode frequency is significantly less than half that of the breathing mode frequency. This indicates that a 1: 2 commensurable relationship between the horizontal S2 mode and the vertical B mode frequency exists for low pressures.

In order to examine the nonlinear mode coupling and internal resonance, an external sinusoidal voltage of varying amplitude and frequency was applied to the lower electrode providing a vertical excitation to the particle pair.

Fig. 4.4a-c shows the particles' horizontal motion (side view) under excitation (amplitude of 1.5 V) at frequencies of 13.8 Hz, 14.0 Hz and 15.2 Hz (which are close to the B mode resonance frequency), under a plasma power of 2.45 W and pressure of 40 mTorr. The corresponding side-view and top-view trajectories of the upstream particle are shown in Fig. 4.4d-f and Fig. 4.4g-i, respectively.

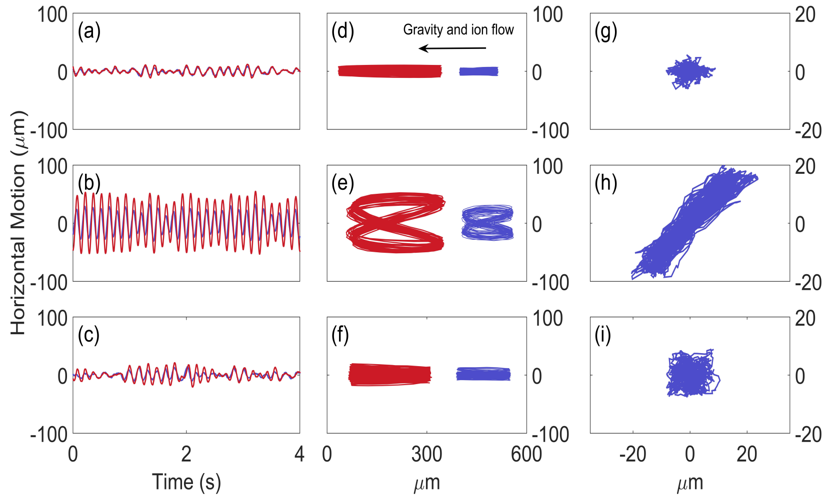

Figure 4.4: Particles' horizontal motion (side view) under a 1.5 V external sinusoidal excitation at a) 13.8 Hz, b)14.0 Hz and c) 15.2 Hz with the blue line for the upstream particle and red line for the downstream particle. d-f) Corresponding trajectories of both particles recorded from the side view camera. g-i) Corresponding trajectories of the upstream particle recorded from the top view camera.

As shown, the particles exhibit primarily random thermal fluctuations at 13.8 Hz and 15.2 Hz (Fig. 4.4a and Fig. 4.4c). However, at a driving frequency of 14.0 Hz, a sloshing type horizontal motion having an amplitude of approximately 20 μm and 40 μm was excited for the upstream and downstream particle, respectively (Fig. 4.4b). This clearly shows that the horizontal motion observed is created through vertical excitation as a result of the onset of an internal resonance at a frequency of 14.0 Hz, which is equal to the frequency of the B mode and twice that of the S2 mode at this pressure and power as shown in Fig. 4.3a.

To illustrate the energy distribution and determine the coupling modes, the Power Spectra Density (PSD) averaged for the horizontal motion over the two particles is shown in Fig. 4.5. As can be seen, at an excitation frequency of 14.0 Hz (dark blue line) a significant energy boost is observed centered around 7.1 Hz, the frequency of the S2 mode, with no significant increase in the vicinity of the S1 mode frequency ($\sim$5.0 Hz). This indicates that energy has been transferred into the S2 mode which is coupled to the B mode through the 1:2 commensurable relationship. It is important to note that this mode coupling between the S2 and the B mode is not in the linear regime. This is a typical nonlinear mode coupling since the resonance frequencies of the modes are not identical.

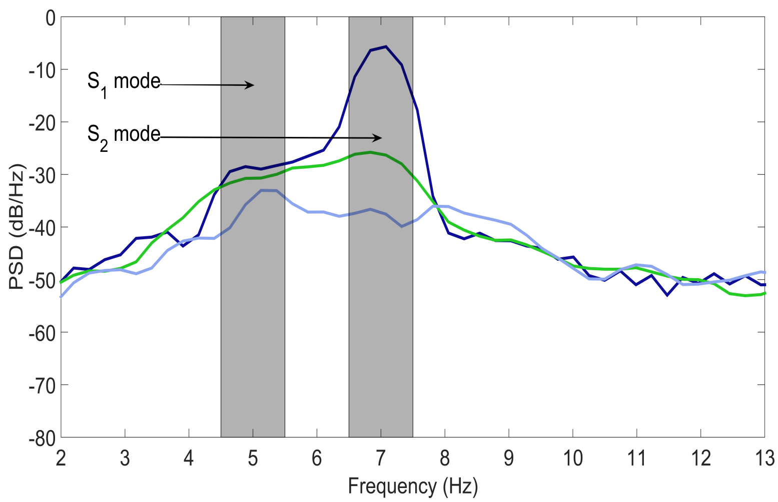

Figure 4.5: The Power Spectra Density (PSD) averaged for the horizontal motion over two dust particles. The dark blue line shows the PSD for a saturated excitation (1.5 V) at a frequency of 14 Hz. The light blue line shows the unsaturated excitation (0.8 V) at the same frequency. The PSD of a saturated excitation (1.5 V) at an off-resonance excitation frequency of 13.8 Hz is shown by the green line.

Such an energy transfer can only be triggered under an external excitation with a large enough amplitude (i.e., saturated excitation). The light blue line in Fig. 4.5 shows the averaged PSD for the same experimental conditions but at a driving voltage of 0.8 V. With this unsaturated excitation, no energy boost is observed in the S2 mode.

The excitation saturation can be illustrated by experimentally measuring the amplitude-frequency response following the method described in chapter three. In this method, particle motions are transferred into the coordinate of each mode employing linear combinations of the original particle trajectories.

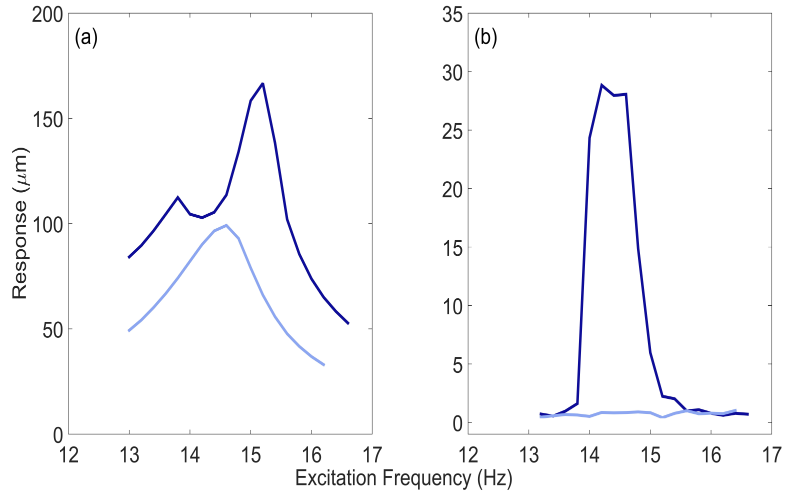

Figure 4.6: Experimentally measured frequency response curves for a) primary B mode and b) sub-harmonic S2 mode. The dark line indicates saturated excitation at 1.5 V, while the light line shows the unsaturated response at 0.8 V.

A Fourier transformation is then implemented on the time series of motion in the new coordinates corresponding to each mode. Primary responses for the B mode are then measured from the amplitude of the FFT spectrum (of the motion in B mode coordinate) at the excitation frequency, while sub-harmonic responses for the S2 mode are determined using the amplitude of the FFT spectrum (of the motion in the S2 mode coordinate) at half the excitation frequency.

The experimentally measured amplitude-frequency responses of the primary B mode and the sub-harmonic S2 mode under a plasma power of 2.45 W and a pressure of 40 mTorr are shown in Fig. 4.6. As can be seen, at an unsaturated excitation amplitude of 0.8 V (light lines), the primary breathing response curve is smooth, showing a single peak unperturbed by internal resonances. Correspondingly, the sub-harmonic S2 mode does not show any excitation. For a saturated excitation (1.5 V, dark lines), internal resonance is triggered. Due to this internal resonance, the primary breathing response (dark line in Fig. 4.6a) decreases while the sub-harmonic S2 response (light line in Fig. 4.6b) increases over the frequency range from approximately 13.8 Hz to 15.2 Hz, indicating an energy transfer from the B to the

S2 mode. As predicted, there is no sign of such an energy transfer channel existing between the horizontal S2 mode and the vertical B mode for pressures higher than 120 mTorr, where the 1:2 commensurable relation is no longer satisfied.

These experimentally measured amplitude-frequency responses are consistent with the theoretically predicted responses in the presence of the 1:2 commensurable relation (internal resonance triggered) as derived in Eqs. 4.43, where the steady state a_1 and a_3 are respectively the secondary response of the S2 mode and the primary response of the B mode. On the other hand, the theoretically predicted responses without the presence of internal resonance have the same form as Eqs. 4.42 with Fig. 4.7 showing the theoretically predicted amplitude-frequency response curves. The numerical solutions of Eqs. 4.43, in which the S2 and B modes are assumed to be commensurable, are shown by the solid lines for both saturated response (dark lines) and unsaturated response for a lower excitation amplitude of 0.8 V (light lines). As shown, the energy transfer from the B to the S2 mode is observed over the same frequency range as experimentally (Fig. 4.6). The excitation of the S2 mode and the depression of the B mode are also successfully predicted. Without the assumption of the commensurate relationship, the solution to Eqs. 4.42, shown in red, shows no energy transfer from the B to the S2 mode.

In this chapter, we studied the internal resonance for dust particle pairs in plasmas. Under low plasma pressures, these two modes can become 1:2 commensurable, in which case the horizontal S2 mode is found to be excited by vertical driving at sufficiently large driving amplitude for frequencies at the resonance frequency of the B mode. Both the PSD and the amplitude-frequency response curves obtained experimentally from particle motion show clear energy transfer from the B mode to the S2 mode. The 1:2 internal resonance was theoretically illustrated by solving the model employing a multiple scale perturbation method. The theoretical response curves were then calculated for the onset of internal resonance and show excellent agree-

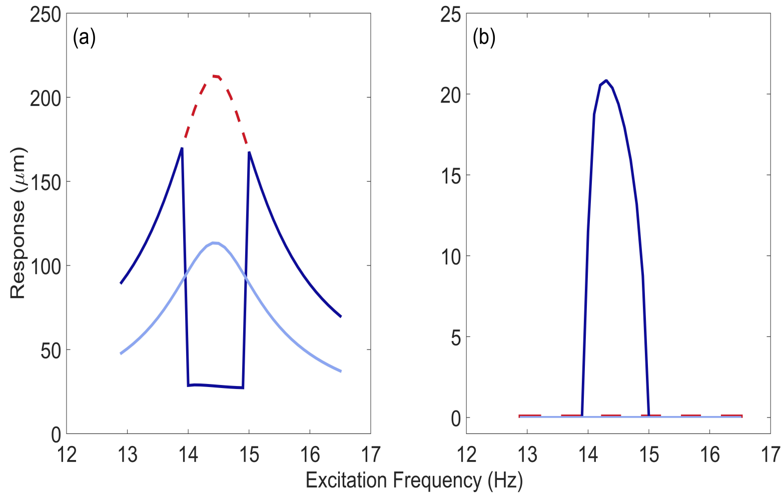

Figure 4.7: The theoretical response curves for a) the primary B mode, and b) the subharmonic S2 mode. The dark blue lines and red dashed lines show the responses under a saturated excitation with and without the assumption that the S2 and the B mode are 1:2 commensurable. The light blue lines are the response curves under an unsaturated excitation.

ment with experimental results. This observation of internal resonance as a result of nonlinear mode coupling reveals the intrinsic nonlinearities of the interaction of dust particles in plasmas. This result also shows the capability for dusty plasmas to act as platforms for the study of the nonlinear dynamics of liquids and solids at a fully resolved kinetic level.

CHAPTER FIVE

An Automatic Response Analysis Method Based on Bayesian Optimization

This chapter presents a novel method for analyzing the amplitude frquency response. The main advantage of this method is that no prior knowledge of the plasma environment is needed to solve the equations of motion for the dust particle embedded in the plasma. As a simple example, the method is applied to a single dust particle levitated in the plasma sheath in a modified GEC rf reference cell.

5.1 Simulation of the Amplitude-Frequency Response

The motion of a single dust particle levitated in the plasma sheath under a vertical sinusoidal excitation can be modeled as a confined forced oscillator (see chapter two),

$$\ddot{x} + \mu\dot{x} + \omega^2 x + \alpha x^2 + \beta x^3 = Fexp(i\Omega t) + c.c., \tag{5.1}$$

where again μ is the neutral drag coefficient, Ω is the frequency of the sinusoidal excitation, F is the amplitude (in units of acceleration) of the excitation, and c.c. stands for the complex conjugate. Usually, the effective restoring force experienced by a particle (from the equilibrium position) is approximated as linear in displacement $-\omega^2 x$ (where ω is considered to be the natural resonance frequency) under the assumption that the particle is levitating in a region with a perfect parabolic sheath potential. However, this linear approximation is invalid given realistic situations, such as charge fluctuations, or oscillations of the dust particle large enough that the sheath potential is intrinsically no longer parabolic. In this case, the restoring force must be extended to the nonlinear regime as $-\omega^2 x - \alpha x^2 - \beta x^3$ where terms higher than $O(x^3)$ are ignored for simplicity. Different from the case of two coupled dust particles, there is no coupled motion in this equation of motion. Thus, the nonlinearities in this equation of motion are completely due to the characteristics of the restoring force (i.e., determined by the electric field of the sheath and the charge of the dust particle) as experienced by the dust particle in the levitation position.

If all the parameters characterizing the particle's motion in Eq. 5.1 are known, an amplitude-frequency response can be simulated by numerically solving this equation of motion. Given a set of parameters $\{\mu, \omega, \alpha, \beta, F\}$ and an excitation frequency Ω, the particle's motion $x(t)$ as a function of time can be simulated by employing the velocity Verlet algorithm. The particle displacement is first updated based on its displacement, velocity, and acceleration at the current time step as

$$x(t+dt) = x(t) + v(t)dt + \frac{a(t)}{2}(dt)^2, \tag{5.2}$$

and the velocity then updated as

$$v(t+dt) = v(t) + \frac{a(t+dt) + a(t)}{2}dt, \tag{5.3}$$

where dt is the time step of the simulation, $v(t)$ is the velocity at time t and $a(t)$ is the acceleration normalized by the particle mass at time t which is determined by Eq. 5.1 as

$$a(t) = -\mu v(t) - \omega^2 x(t) - \alpha x^2(t) - \beta x^3(t) + 2Fcos(\Omega t). \tag{5.4}$$

With the correct parameters $\{\mu, \omega, \alpha, \beta, F\}$, the simulated particle's motion $x(t)$ will converge to a consistent oscillating motion governed by the excitation frequency Ω. Following the same approach as we did for the experimental data (see chapter three), the primary and secondary responses can then be simulated by conducting an FFT analysis of the simulated particle's motion $x(t)$ and ensuring the corresponding primary and secondary peaks. Finally, by conducting the simlation under a series of consecutive excitation frequencies Ω, complete amplitude-frequency response curves (either primary or secondary) can be simulated according to the given parameters $\{\mu, \omega, \alpha, \beta, F\}$.

By matching these simulated response curves to those directly measured from experiment, we can easily identify the parameters $\{\mu^*, \omega^*, \alpha^*, \beta^*, F^*\}$. These parameters correctly characterize the plasma and the environmental properties in the position where the dust particle levitates. In order to find parameters that result in simulated response curves matching the experimental ones, the parameter space $\{\mu, \omega, \alpha, \beta, F\}$ has to be searched. For each combination of parameters, an entire response curve needs to be simulated which involves the process of numerically solving the equation of motion Eq. 5.1 hundreds of times (depending on the frequency range of interest). In this case, a random search of the parameter space requires tremendous computational power, which is extremely inefficient, if not infeasible. The alternative presented here employs a Bayesian optimization-based method of searching the parameter space for the correct parameters characterizing the plasma properties.

However, before moving on to the Bayesian optimization, we must first define a measure quantifing the distance between the simulated response curves and the experimentally measured ones, i.e., dtermining the similarity between a simulated response curve and an experimentally measured curve. We define this measure to be a function $L : \theta = \{\mu, \omega, \alpha, \beta, F\} \mapsto \mathbb{R}$ measuring the L2 norm between the simulated and the experimentally measured response curves (normalized by the experimentally measured responses) as

$$L(\theta) = \sum_{i=1}^{N} (\frac{r_e(\Omega_i) - r_s(\Omega_i, \theta)}{r_e(\Omega_i)})^2, \tag{5.5}$$

where $r_e(\Omega_i)$ and $r_s(\Omega_i)$ are the experimentally measured and the simulated response at the excitation frequency Ω_i respectively, and the summation is conducted over the range of excitation frequencies. Notice that $L(\theta)$ is not unique. Any function that measures the distance between the simulated and the experimentally measured repsonse curves should serve the purpose. However, it is important to note that different forms of the function $L(\theta)$ may result in different performance metrics during the process of optimization.

With the difference function $L(\theta)$ defined, the problem can now be specified as: Find $\theta^* = \{\mu^*, \omega^*, a^*, b^*, F^*\}$ subject to

$$\{\mu^*, \omega^*, a^*, b^*, F^*\} = \underset{\{\mu,\omega,\alpha,\beta,F\}}{\operatorname{argmin}} (L(\{\mu, \omega, a, b, F\})), \tag{5.6}$$

$$(\theta^* = \underset{\theta}{\operatorname{argmin}}(L(\theta))). \tag{5.7}$$

Notice that it is possible that the simulation of the particle's motion $x(t)$ may not converge under some combinations of the parameters. Those parameter combinations correspond to situations where either the parameters have no physical meaning or are not suitable for describing the environment in the plasma sheath. In these cases, the distance function $L(\theta)$ should be set to some large value (e.g., 1×10^5) in order to allow the optimization process to be continued.

5.2 Bayesian Optimization

As discussed before, a random search of the parameter space to find the optimal parameters that minimize the distance function is extremely expensive. Thus, the distance function is minimized here by searching the parameter space in a Bayesian manner (also known as Bayesian optimization, which has been applied in machine learning, especially in deep learning, for fine tuning neural networks). First, we introduce a surrogate function f modeling the distribution of the value of the distance function L at each parameter combination θ. This surrogate function can be understood to be an approximation of the real distance function L, where this approximation will be continuously updated becoming more accurate as more information about the distance function is observed (i.e., more simulations of the distance function have been conducted). We shall see later that an efficient minimization of the distance function can be achieved by searching the parameter space (with a guide of which parameter to simulate next) to maximize the expected improvement defined on the surrogate function.

There are different ways of modeling the surrogate function. Here, we use a generative model, the Tree-structured Parzen Estimator (TPE) [60] to characterize the surrogate function, i.e., to model the distribution of the values of the surrogate function at a specific parameter combination $\theta = \{\mu, \omega, a, b, F\}$ conditioned on all observed data

$$\mathcal{D}_{1:t} = \{\theta_{1:t}, L(\theta_{1:t})\}, \tag{5.8}$$

where each of the data points consists of a pair of a parameter combination θ and the corresponding distance function $L(\theta)$ from the simulation. Each time a new data point is observed (simulated), it is stored to a data pool $\mathcal{D}_{1:t}$ that contains all the data observed (simulated) up to time t. According to the Bayes rule, the distribution of the values of the surrogate function at θ conditioned on $\mathcal{D}_{1:t}$ yields

$$p(f|\theta; \mathcal{D}_{1:t}) = \frac{p(\theta|f; \mathcal{D}_{1:t})p(f; \mathcal{D}_{1:t})}{p(\theta; \mathcal{D}_{1:t})}, \tag{5.9}$$

where the likelihood $p(\theta|f; \mathcal{D}_{1:t})$ is modeled by the Parzen density estimators as

$$p(\theta|f; \mathcal{D}_{1:t}) = \begin{cases} l(\theta), \text{if } f < f^* \\ g(\theta), \text{if } f \geq f^*. \end{cases} \tag{5.10}$$

The likelihood function has two parts. If the value of the surrogate function is less than a threshold f^*, the likelihood will be governed by the Parzen density estimator $l(\theta)$, otherwise the likelihood will be governed by $g(\theta)$. Here, the Parzen density estimators $l(\theta)$ and $g(\theta)$ are nonparametric estimators that employ a Gaussian Mixture centered at each data point from the subset of the data pool with $f < f^*$ and $f \geq f^*$, respectively. They can be quantified as

$$l(\theta) = C_1 \Sigma_{i \in \{f < f^*\}} e^{-\frac{1}{2}(\theta - \theta_i)^T \Sigma^{-1} (\theta - \theta_i)}, \tag{5.11}$$

$$g(\theta) = C_2 \Sigma_{i \in \{f \geq f^*\}} e^{-\frac{1}{2}(\theta - \theta_i)^T \Sigma^{-1} (\theta - \theta_i)}, \tag{5.12}$$

where C_1, C_2 are normalization factors and Σ is a uniformly assigned covariance matrix.

Once the likelihood is modeled, the corresponding marginal distribution at θ given the observed data set $\mathcal{D}_{1:t}$ (the denominator of Eq. 5.9) can be calculated as the expectation of the likelihood function

$$\begin{aligned} p(\theta;\mathcal{D}_{1:t}) =& \int_{-\infty}^{\infty} p(\theta|f;\mathcal{D}_{1:t})p(f;\mathcal{D}_{1:t})df \\ =&(l(\theta)-g(\theta))\int_{-\infty}^{f^*} p(f;\mathcal{D}_{1:t})df + g(\theta). \end{aligned} \tag{5.13}$$

As such, we can derive the posterior distribution of the surrogate function in terms of the Parzen density estimators by substituting Eq. 5.10 and Eq. 5.13 into Eq. 5.9, which yields

$$p(f|\theta;\mathcal{D}_{1:t}) = \begin{cases} \frac{l(\theta)p(f;\mathcal{D}_{1:t})}{(l(\theta)-g(\theta))\int_{-\infty}^{f^*} p(f;\mathcal{D}_{1:t})df+g(\theta)}, \text{if } f < f^* \\ \frac{g(\theta)p(f;\mathcal{D}_{1:t})}{(l(\theta)-g(\theta))\int_{-\infty}^{f^*} p(f;\mathcal{D}_{1:t})df+g(\theta)}, \text{if } f \geq f^*, \end{cases} \tag{5.14}$$

where the prior distribution of the surrogate function $p(f;\mathcal{D}_{1:t})$ is still undetermined. However, as shown later, the exact form of this prior distribution is irrelavant in the process of maximizing the expected improvement in order to find the next simulation.

Although the distribution of f is assumed to approximate the real distance function L up to observed data $\mathcal{D}_{1:t}$, it is still not known how well this approximation of the surrogate function correlates to the real distance function L. The idea of Bayesian inference is that the posterior distribution of f becomes closer to the real distance function L if it is updated when more information about the distance function is revealed. Specifically, information about the distance function is revealed in terms of the data (paired as $\{\theta, L(\theta)\}$) from simulation. As new data points $\{\theta_{t+1}, L(\theta_{t+1})\}$ are simulated, they are added to the observed data pool, which is updated to $\mathcal{D}_{1:t+1}$. The posterior distribution is then updated accordingly based on $\mathcal{D}_{1:t+1}$ and eventually resembles the behavior of the real distance function. An exterme argument for this Bayesian inference would be that if every point on the distance function were simulated (although this is impossible for a continuous function) and after updating the posterior distribution with the last simulated point, the posterior distribution function should be identical to the distance function itself.

One big difference between the Bayesian optimization and the random search of the parameter space is the manner in which each explores the parameter space, i.e., chooses the next parameter combination to simulate. Unlike the random search, the Bayesian optimization chooses the next parameter combination with the goal that it will maximize the expected improvement [61] defined as

$$EI(\theta) = \mathbb{E}[max(f_t^* - f, 0)], \tag{5.15}$$

where f_t^* (which is also the threshold in Eq. 5.10) defines the best optimization (the lowest value) of the distance function L with the observation of data $\mathcal{D}_{1:t}$. As such, the next parameter combination to be simulated is

$$\begin{aligned} \theta_{t+1} =& \underset{\theta}{\text{argmax}} \int_{-\infty}^{\infty} \max(f^* - f, 0) p(f|\theta; \mathcal{D}_{1:t}) df \\ =& \underset{\theta}{\text{argmax}} \frac{\int_{-\infty}^{f^*} (f^* - f) p(f; \mathcal{D}_{1:t}) df}{\frac{g(\theta)}{l(\theta)} (1 - \int_{-\infty}^{f^*} p(f; \mathcal{D}_{1:t}) df) + \int_{-\infty}^{f^*} p(f; \mathcal{D}_{1:t}) df} \\ =& \underset{\theta}{\text{argmax}} \frac{l(\theta)}{g(\theta)}, \end{aligned} \tag{5.16}$$

where the second equation is derived by substituting the posterior Eq. 5.14. Examining the results, it becomes clear that the exact form of the prior distribution of the surrogate function is irrelevant. As long as the cumulative distribution of the prior $\int_{-\infty}^{f^*} p(f; \mathcal{D}_{1:t}) df$ is strictly less than 1 (which is indeed the case since the prior is a probability measure), the expected improvement is maximized where $\frac{l(\theta)}{g(\theta)}$ is maximized, which does not depend on the form of the prior distribution of the surrogate function $p(f; \mathcal{D}_{1:t})$. This is also the reason that the third equation holds in Eq. 5.16. Therefore, the next parameter combination is chosen such that it maximize the quotient of the Parzen density estimators $\frac{l(\theta)}{g(\theta)}$.

Using Bayeisan optimization, the parameter combination that minimizes the distance between the simulated response curves and the experimentally measured response curves (i.e., minimizes the distance function L) for a dust particle levitated in the plasma sheath can be found efficiently, despite the expensive computational cost of each simulation.

5.3 Response Analysis Based On Bayesian Optimization

There is still one problem which needs to be solved before a Bayesian optimization can be successfully conducted. As discussed in previous chapters, the primary response is mainly (but not exclusively) governed by the linear parts of Eq. 5.1 while the secondary response is mainly (but not exclusively) governed by the nonlinear parts of Eq. 5.1. In other words, the secondary response (as a nonlinear response) is very sensitive to the higher order nonlinear terms, i.e., αx^2 and βx^3, while the primary response is more sensitive to the linear terms. In this case, the correct parameter combination that reveals the true plasma condition must be determined employing both the primary and secondary responses. As such, it is necessary to minimize the distance functions for both the primary and secondary responses simultaneously. A simple way of achieving this is to minimize a weighted sum of these two difference functions. Here, we use a weight sum

$$L_t = L_p(\theta) + 0.05 L_s(\theta), \tag{5.17}$$

where $L_p(\theta)$ and $L_s(\theta)$ are the distance functions for the primary and the secondary responses, respectively. This weighted sum is designed in such a way that the distance function for the secondary response is less weighted by considering the fact that the match of the simulated primary (linear) response curve to the experimentally measured one is more important than that of a secondary (nonlinear) response. The Bayesian optimization is conducted for this weighted sum of the distance functions. Fig. 5.1 shows the Bayesian optimized simulated response curves for a single particle levitated in the plasma sheath in a GEC rf reference cell at a plasma power of 1.68 Watts and a pressure of 40 mTorr, with Fig. 5.1a showing the primary response and Fig. 5.1b the secondary response. The particle motion is excited using a driving amplitude of 1 V and 1.5 V and is plotted in solid and dashed curves, respectively. As shown, the optimized response curves (red curves showing the simulated response according to the model Eq. 5.1) closely resemble the experimentally measured responses curves (black) in both the primary and secondary region.

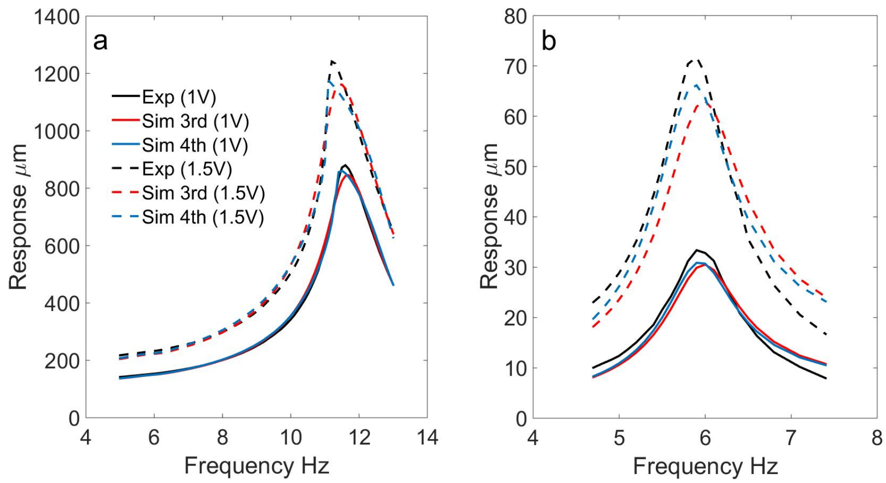

Figure 5.1: a) The primary experimentally measured response curve (in black), the primary Bayesian optimized response curve (in red) and the primary Bayesian optimized response curve based on model Eq. 5.34 (in blue). b) The secondary (super-harmonic) experimentally measured response curve (in black), the secondary (super-harmonic) Bayesian optimized response curve (in red) and the secondary (super-harmonic) Bayesian optimized response curve based on model Eq. 5.34 (in blue).

The corresponding optimized parameters are calculated as the average of the optimized parameters for five different trials and shown in Table. 5.1 with the coefficients of variation shown in parentheses. Notice that the sign of the coefficient of the quadratic nonlinearity α determines only the particle's shift direction, which has no effect on the measurement of the response curves. Despite the randomness involved in the parameter search, this optimization converges to a consistent result as evidenced by the low coefficients of variance. The relatively high coefficient of variance observed for the parameter β (the coefficient of the cubic nonlinearity) is due to the fact that the response curves are less sensitive to the nonlinearities of higher order which results in a higher fluctuation of the measurement of the coefficient of the cubic nonlinearity β.

Fig. 5.2 shows the loss value (the value of the difference function) as a function of the number of iterations for the single dust particle excited at both 1 V (a) and 1.5 V (b) excitations, each of which has five independent trails. As shown, the loss values show a rapid drop after the first several iterations and converge after a few hundreds of iterations. This indicates the high efficiency of the presented Bayesian optimization method in exploitating the parameter space for the correct parameter combination. (However, in order to boost the accuracy and ensure a wide exploration of the parameter space, a large number of iterations are conducted.) The higher convergency loss value observed for the single dust particle under the 1.5 V excitation ($\approx 4.3 \times 10^{-3}$) than under the 1 V excitation ($\approx 2.2 \times 10^{-3}$) can be attributed to an increase in the difficulty of (exactly) capturing the spring softening phenomenon (i.e., the nonlinear phenomenon that causes the primary resonance peak to be 'bent' in the low frequency direction) as the excitation amplitude becomes larger (see Fig. 5.1a).

For comparison, these parameters were also measured by analytically solving the equation of motion given in Eq. 5.1 employing the multiple-scale perturbation method [42] and then fitting the experimentally measured response curves to these approximation solutions.

We first consider the situation in which the excitation frequency is approximately equal to the resonance frequency, i.e., $\Omega \approx \omega$ and re-order each term in Eq. 5.1 using a dimensionless small value ϵ as described in chapter two. In this case, the equation of motion Eq. 5.1 becomes

$$\ddot{x} + \epsilon^2 \mu \dot{x} + \omega^2 x + \alpha x^2 + \beta x^3 = \epsilon^3 F exp(i\Omega t) + c.c., \tag{5.18}$$

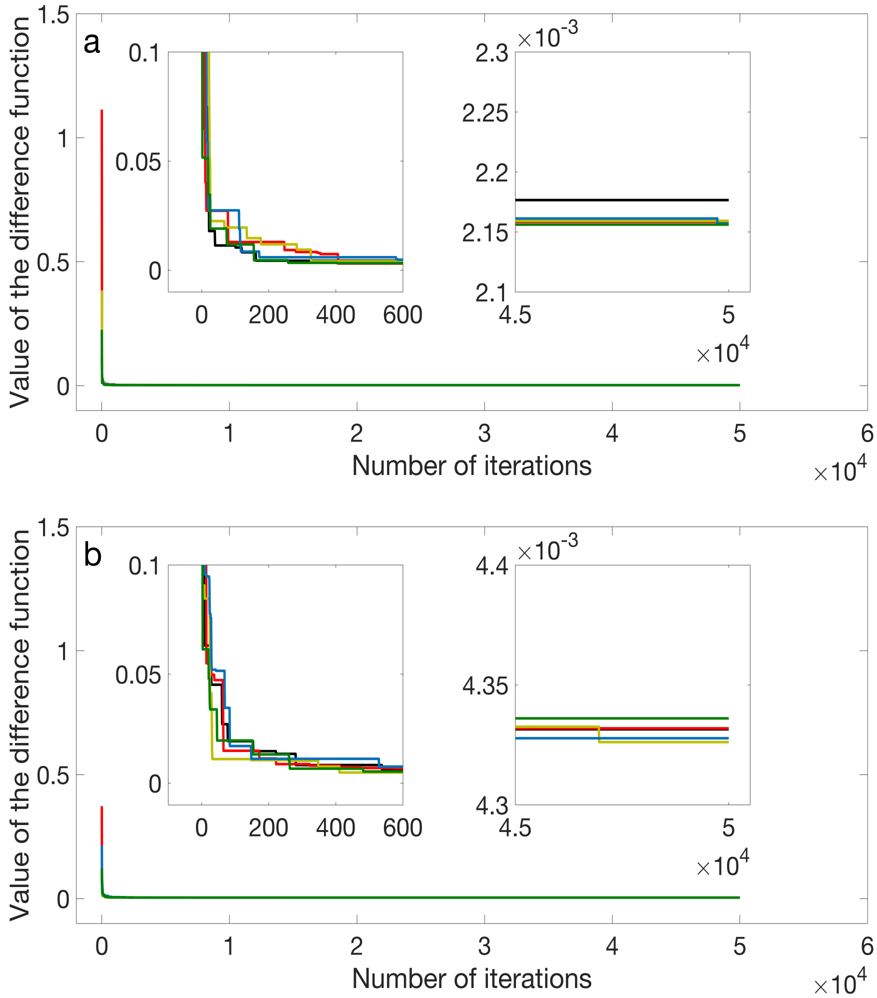

Figure 5.2: The loss (value of the difference function) as a function of the number of iterations for a dust particle excited under an excitation amplitude of a) 1 V and b) 1.5 V. Colors denote the five independent trials.

with an excitation frequency $\Omega = \omega + \epsilon^2\delta$. A test solution is introduced

$$x(t_0, t_1, t_2; \epsilon) = \epsilon x_0(t_0, t_1, t_2) + \epsilon^2 x_1(t_0, t_1, t_2) + \epsilon^3 x_2(t_0, t_1, t_2), \tag{5.19}$$

where $t_1 = \epsilon t_0$ and $t_2 = \epsilon^2 t_0$ are the 'slow' times. Different from previous cases where only one 'slow' time is introduced, here two 'slow' times are used due to the cubic nonlinearities involved in Eq. 5.1 (as compared to Eq. 2.21 and Eq. 4.8 where the highest nonlinearities are quadratic in nature).

Substitution of the test solution in Eq. 5.34 and decomposing the equations of motion according to order of approximation, the equation of motion to first order of ϵ is now given by

$$\frac{\partial^2 x_0}{\partial t_0^2} + \omega^2 x_0 = 0, \tag{5.20}$$

with the solution

$$x_0(t_0, t_1, t_2) = A(t_1, t_2)e^{i\omega t_0} + C.C., \tag{5.21}$$

where the amplitude $A(t_1, t_2)$ is dependent on the 'slow' times t_1 and t_2. The equation of motion to second order of ϵ yields

$$\frac{\partial^2 x_1}{\partial t_0^2} + \omega^2 x_1 = -2\frac{\partial^2 x_0}{\partial t_0 \partial t_1} - \alpha x_0^2. \tag{5.22}$$

Substitution of this into the solution for the first order of approximation (Eq. 5.21), the secular term in this order can now be eliminated by setting $\frac{\partial^2 x_0}{\partial t_0 \partial t_1} = 0$, indicating that the amplitude $A(t_1, t_2)$ is actually independent of the 'slow' time t_1. Thus, the solution to first order of approximation is

$$x_0(t_0, t_1, t_2) = A(t_2)e^{i\omega t_0} + C.C.. \tag{5.23}$$

Consequently, the solution to second order of approximation can be derived as

$$x_1(t_1, t_2) = \frac{\alpha}{3\omega^2}[A(t_2)^2 e^{2i\omega t_0} + \bar{A}(t_2)e^{-2i\omega t_1} - 3A(t_2)\bar{A}(t_2)] + C.C.. \tag{5.24}$$

This order of approximation still does not produce a solution for the amplitude $A(t_2)$, requiring investigation of the next higher order. The equation of motion to third order of approximation in ϵ has the form

$$\begin{aligned}\frac{\partial^2 x_2}{\partial t_0^2} + \omega^2 x_2 = &- 2\frac{\partial^2 x_1}{\partial t_0 \partial t_1} - 2\frac{\partial^2 x_0}{\partial t_0 \partial t_2} - \frac{\partial^2 x_0}{\partial t_1^2} - \mu\frac{\partial x_0}{\partial t_0} - 2\alpha x_0 x_1 - \beta x_0^3 \\ &+ Fe^{i(\omega t_0 + \delta t_2)} + C.C..\end{aligned} \tag{5.25}$$

Substituting Eq. 5.23 and Eq. 5.24 into Eq. 5.25 and eliminating the secular term, the amplitude $A(t_2)$ can now be derived with the result found to satisfy the relationship

$$2i\omega\frac{\partial A(t_2)}{\partial t_2} + \mu A(t_2) + (3\beta - \frac{10\alpha}{3\omega^2})A(t_2)^2\bar{A}(t_2) - \frac{1}{2}Fe^{i\delta t_2} = 0. \tag{5.26}$$

Solving Eq. 5.26, the steady state solution for the amplitude A can now be determined as

$$\frac{F^2}{4\omega^2} = (\frac{A\mu}{2})^2 + [(\frac{9\beta\omega^2 - 10\alpha^2}{24\omega^3})A^3 - (\Omega - \omega)A]^2. \tag{5.27}$$

Fitting the experimentally measured primary response curve to this relationship, $9\beta\omega^2 - 10\alpha^2$ can be measured and if either α or β can be determined, the other can be calculated.

The secondary responses can be examined to determine α. Considering an excitation frequency approximately half that of the resonance frequency $2\Omega = \omega + \epsilon\delta$, the equations of motion can be decomposed into different orders of ϵ in a similar manner. The equation of motion to first order of ϵ yields

$$\frac{\partial^2 x_0}{\partial t_0^2} + \omega^2 x_0 = Fe^{i\Omega t_0} + C.C., \tag{5.28}$$

with a solution to first order of approximation of

$$x_0(t_0, t_1) = B(t_1)e^{i\omega t_0} + \frac{F}{2(\omega^2 - \Omega^2)}e^{i\Omega t_0} + C.C., \tag{5.29}$$

where the amplitude $B(t_1)$ depends on the 'slow' time t_1 and will be determined by eliminating the secular term in the equation of motion to second order of approximation. The equation of motion to the second order of approximation has the form

$$\frac{\partial^2 x_1}{\partial t_0^2} + \omega^2 x_1 = -2\frac{\partial^2 x_0}{\partial t_0 \partial t_1} - 2\mu\frac{\partial x_0}{\partial t_0}\alpha x_0^2. \tag{5.30}$$

Substituting Eq. 5.29 into Eq. 5.30 and eliminating the secular term, yields

$$2i\omega\frac{\partial B(t_1)}{\partial t_1} + i\omega\mu B(t_1) + \alpha[\frac{F}{2(\omega^2-\Omega^2)}]^2 e^{i\delta t_1} = 0. \tag{5.31}$$

Consequently the amplitude $B(t_1)$ can be found as

$$B(t_1) = ce^{-\mu t_1} + \frac{i\alpha[\frac{F}{2(\omega^2-\Omega^2)}]^2}{\omega(\mu+2i\delta)}e^{i\delta t_1}, \tag{5.32}$$

where the first part decays after a long time. Thus, the steady state solution to first order of approximation for an excitation close to half the resonance frequency has the form

$$x(t_0) = \frac{F}{\omega^2-\Omega^2}cos(\Omega t_0) - \frac{\alpha F^2}{4\omega(\omega^2-\Omega^2)^2[\frac{\mu}{4}^2+(2\Omega-\omega)^2]^{\frac{1}{2}}}sin(2\Omega t_0-\phi), \tag{5.33}$$

where $\phi = actg(\frac{4\Omega-2\omega}{\mu})$ is a shifted phase which is dependent on the excitation frequency. The experimentally measured secondary response curve can now be fitted to the term $\frac{\alpha F^2}{4\omega(\omega^2-\Omega^2)^2[\frac{\mu}{4}^2+(2\Omega-\omega)^2]^{\frac{1}{2}}}$ to measure the parameter denoting the quadratic nonlinearities α, and the parameter characterizing the cubic nonlinearities can be determined accordingly from Eq. 5.27.

The parameters measured using the multiple-scale approximation are shown in Table. 5.1. As shown, the parameters measured using the Bayesian optimization are consistent with those measured from the multiple-scale perturbation with low percent differences (less than 10 %), except for the value of β under 1.5 V excitation (with 57.6 % difference).

Due to the limitation of the perturbation method, extending the model (Eq. 5.1) to higher order of nonlinearities and deriving the corresponding approximation solutions is tedious. However, in the Bayesian optimization method, this would be quite simple. As a representative example, the model is extended here to an additional nonlinearity of higher order,

$$\ddot{x} + \mu\dot{x} + \omega^2 x + \alpha x^2 + \beta x^3 + \gamma x^4 = Fexp(i\Omega t) + C.C.. \tag{5.34}$$

By applying the Bayesian method, the optimized parameters are determined (Model 2 in Table. 5.1) with the corresponding response curves shown in Fig. 5.1 (blue curves). Fig. 5.3 shows the loss value (the value of the distance) as a function of the number of iterations for the single dust particle excited at both 1 V (a) and 1.5 V (b) based on the new model (Eq. 5.34). Again, each of the Bayesian optimizations has five independent trials.

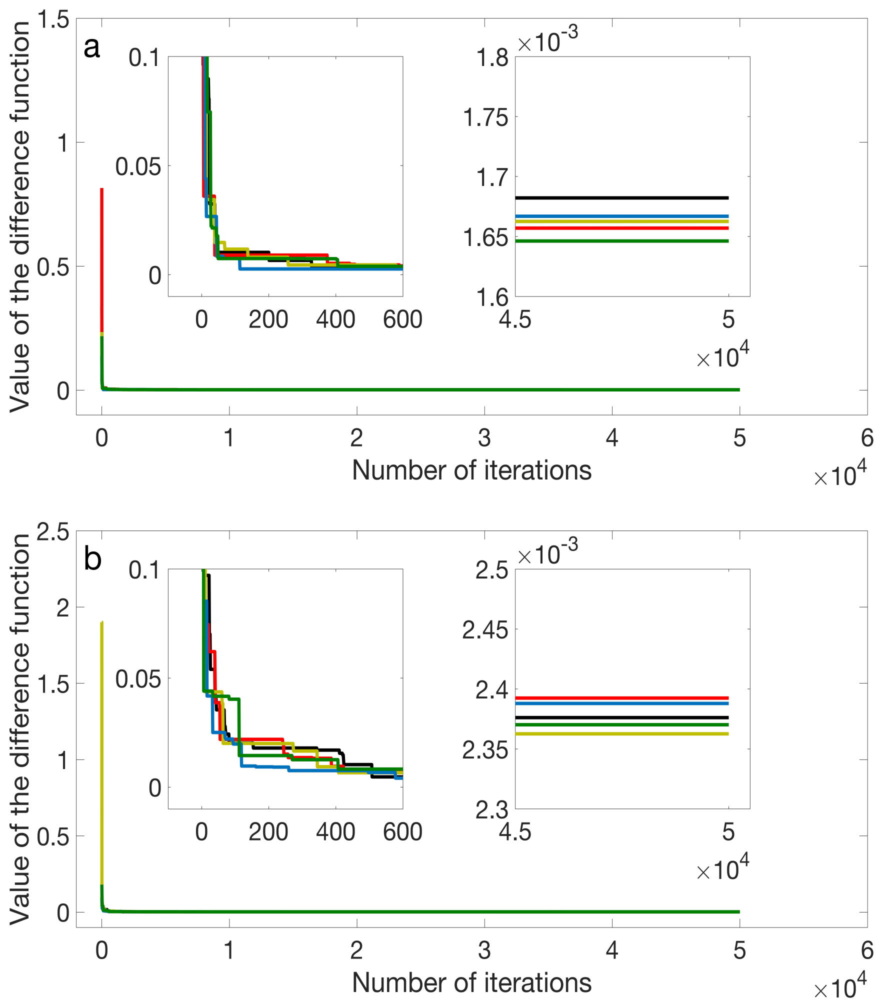

Figure 5.3: The loss (value of the difference function) as a function of the number of iterations for a dust particle excited under an excitation amplitude of a) 1 V and b) 1.5 V based on the model provided in Eq. 5.34. Color denotes the five independent trials.

By considering nonlinearities to the fourth order, the value of the difference function can be further reduced (Fig. 5.3), i.e., the difference function reaches 1.6×10^{-3}

for 1 V excitation and 2.3×10^{-3} for 1.5 V excitation, indicating a better match between the simulated response curves and the experimentally measured ones. This can be seen in Fig. 5.1a, where the primary response curves for a model considering nonlinearities to fourth order (blue curves) more accurately reproduces the spring softening behavior. By introducing nonlinearities to the fourth order, the measured drag coefficient μ, excitation amplitude F and the coefficient of the quadratic nonlinearity α also become closer to the values calculated employing the perturbation approach. However, the coefficient of the cubic nonlinearities β has a large deviation as can be seen in table. 5.1. Considering the condition characterizing the spring softening effect (seen from Eq. 5.27)

$$9\beta\omega^2 - 10\alpha^2 < 0, \tag{5.35}$$

the critical value of β for the existence of the spring softening phenomenon can be derived as $\beta < \beta_c \approx 8.1 \times 10^{-4}$, as the measured values for the coefficient of the quadratic nonlinearity α are consistent in both models (Eq. 5.1 and Eq. 5.34). Notice that the condition Eq. 5.35 is derived only to the first order of approximation. The existence of the spring softening phenomenon with a value of β violating this condition indicates that in order to correctly determine the coefficient of the cubic nonlinearities, modification of higher order nonlinearities (at least one order higher) should not be ignored.

Table 5.1: The parameter space measured for Model 1 (Eq. 5.22) from the Bayesian optimization method and the multiple-scale perturbation method, and for Model 2 (Eq. 5.34) from the Bayesian optimization method are shown in this table. For the Bayesian optimization method, the measurments are averages of five independent experimental trials, with the corresponding coefficients of variance shown in parentheses.

Methods	μ (s^{-1})	ω (Hz)	$\|\alpha\|$ ($\mu m^{-1} \cdot s^{-2}$)	β ($\mu m^{-2} \cdot s^{-2}$)	F ($\mu m^{-1} \cdot s^{-2}$)	$\|\gamma\|$ ($\mu m^{-3} \cdot s^{-2}$)
Excitation 1.0 V:						
Model 1	10.1 (0.6%)	11.9 (0.1%)	2.1 (0.9%)	3.9×10^{-4} (5.7%)	6.3×10^{5} (0.4%)	
Multiple-scale	9.6	11.9	2.0	3.5×10^{-4}	6.2×10^{5}	
Model 2	9.7 (1.5%)	11.8 (0.3%)	2.0 (1.2%)	14.2×10^{-4} (7.3%)	6.2×10^{5} (0.4%)	1.8×10^{-6} (6.6%)
Excitation 1.5 V:						
Model 1	10.9 (0.1%)	11.9 (0.0%)	2.1 (0.8%)	3.8×10^{-4} (4.0%)	9.4×10^{5} (0.2%)	
Multiple-scale	10.2	11.9	1.9	2.1×10^{-4}	9.1×10^{5}	
Model 2	10.3 (1.3%)	11.7 (0.2%)	2.0 (1.2%)	15.5×10^{-4} (3.5%)	9.0×10^{5} (0.6%)	1.2×10^{-6} (5.6%)

CHAPTER SIX

A Quick Method to Determine the Dust Charge based on Vertical Pair Interaction

6.1 New Method for Estimating Charge

A quick but naive method of measuring the charge of dust particles levitated in the plasma sheath region is to measure and to compare the levitation position of the upstream dust particle in a vertical pair structure and a single particle structure, respectively.

In the experiment, we first form a vertical dust pair at a desired plasma condition (e.g., plasma pressure and plasma power) at which we want to estimate the charge of the dust particle. As an example, the left picture in Fig. 6.1 shows the side-view picture of a dust pair at a plasma pressure of 40 mTorr and a plasma power of 9.8 Watts. Then we kick off the downstream particle by a verti-laser pulse. The single remaining particle is shown in the picture on the right in Fig. 6.1.

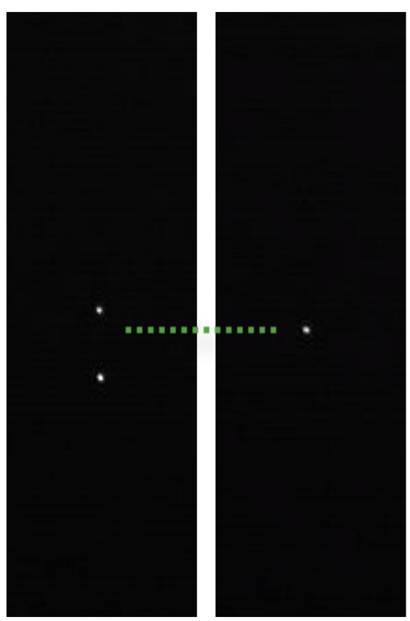

Figure 6.1: A particle pair structure and a single particle levitated in the plasma sheath at a plasma pressure of 40 mTorr and a plasma power of 9.8 Watts.

As shown, when the downstream particle is kicked off by a laser pulse, the upstream particle moves down due to the loss of the repulsive interaction force from the downstream particle. Based on this observation, we can roughly but very quickly estimate the charge on the dust particle by measuring the distance d that the upstream particle moves down after removing the downstream particle, the inter-particle spacing R and the vertical restoring confinement ω_0 at the position where the single particle levitates.

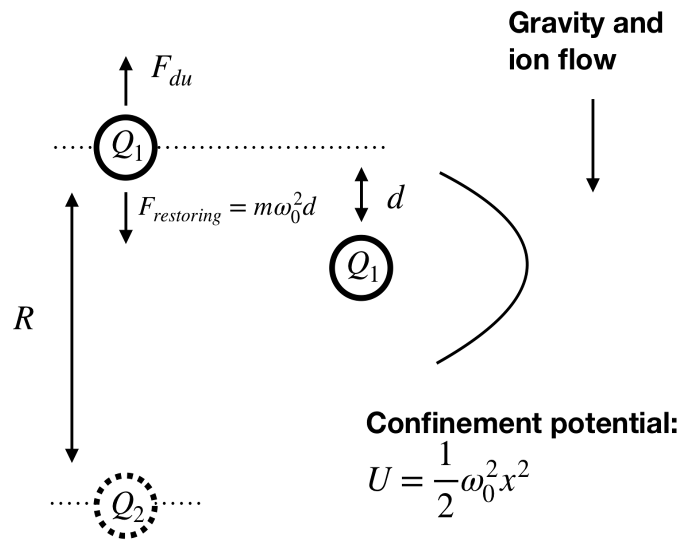

Figure 6.2: Sketch of the transition from a vertical paired structure to a single particle structure.

Considering a small displacement of the upstream particle d and ignoring any non-linear parts of the restoring potential, the repulsive interaction from the downstream particle to the upstream particle is equal to the restoring force component induced by the displacement of the upstream particle as shown in Fig. 6.2, yielding

$$F_{du} = m\omega_0^2 d, \tag{5.1}$$

where the F_{du} is the interaction force from downstream particle to the upstream particle, and the mass of the dust particle $m = \frac{4}{3}\pi r_{MF}^3 \rho_{MF}$ where the radius of the

Melamine Formaldehyde (MF) particle is $r_{MF} = 8.89 \pm 0.09\ \mu m$ and the mass density of the MF particle is $\rho_{MF} = 1.51\ g/cm^3$. If we assume that the interaction force from the downstream particle to the upstream particle has the form of Coulomb force (since the upstream particle are barely affected the ion wake) the force balance in Eq. 5.1 becomes

$$\frac{Q_1 Q_2}{4\pi\epsilon_0 R^2} = m\omega_0^2 d, \tag{5.2}$$

where Q_1 and Q_2 are the charge of the upstream and downstream particle respectively, and ϵ_0 is the vacuum electric permittivity. Usually, the charge of the downstream particle is reduced due to the effect of the ion wake. In this case, the charge of the downstream particle can be written as $Q_2 = \xi Q_1$ where ξ is the de-charging factor, and the charge of the upstream particle Q_1 can be derived as

$$Q_1 = \sqrt{\frac{4\pi\epsilon_0 m d}{\xi}}\omega_0 R. \tag{5.3}$$

Note that this interaction force from the downstream particle to the upstream particle F_{du} is not necessarily in the form of a Coulomb interaction. It can also be approximated by other forms, for example the Yukawa interaction force. As long the as the Debye length of the Yukawa interaction is known, the dust charge can be calculated in the same manner.

Here we measure the levitation positions for both the dust pair and the single particle (by removing the downstream particle) at different plasma powers (from 4.5 W to 9.8 W) at a plasma pressure of 40 mTorr. The results are shown in Fig. 6.3.

As shown, the levitation positions decrease as plasma power increases (for plasma powers higher than 4.5 W), and the drop in position of the upstream particle after the removal of the downstream particle is consistent for all the plasma powers and is clearly observed.

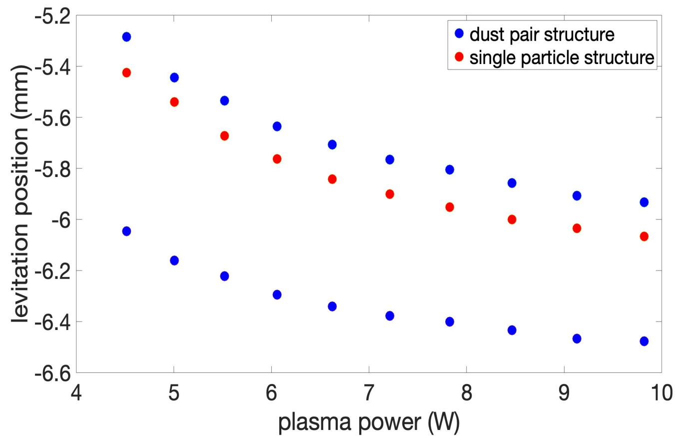

Figure 6.3: The levitation position of the dust pair and the corresponding upstream particle (with the removal of the downstream particle) at varying plasma powers at 40 mTorr.

Based on this measurement of levitation positions, the inter-particle spacing R and the displacement of the upstream particle d can be in turn measured for varying plasma powers and are shown in Fig. 6.4.

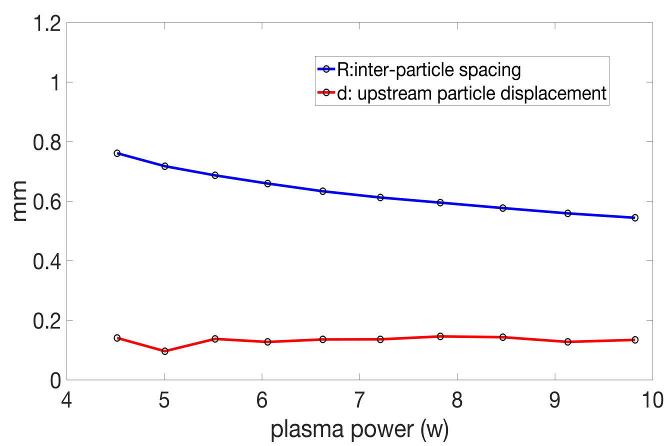

Figure 6.4: The inter-particle spacing (blue line) and the displacement of the upstream particle (after a laser is used to kick out the downstream particle, red line) at a plasma pressure of 40 mTorr.

The corresponding vertical restoring confinement is shown in Fig. 6.5. As the plasma power increases, the inter-particle spacing decreases while there is no clear displacement change for the upstream particle observed. The vertical restoring confinement at the position where the single particle structure levitates increases with the increase in plasma power.

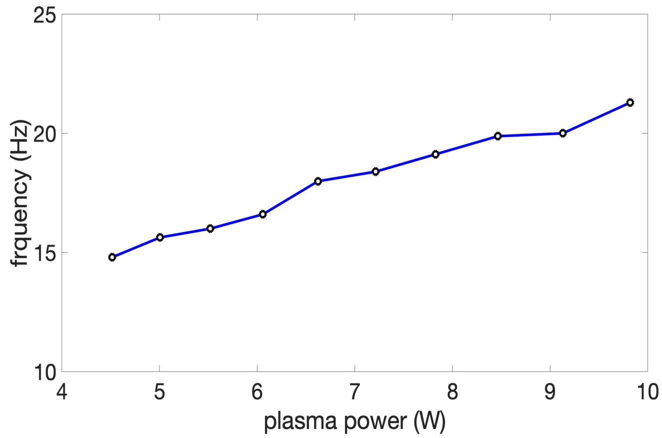

Figure 6.5: The vertical restoring confinement measured at the levitation position of the single particle structure at a plasma pressure of 40 mTorr.

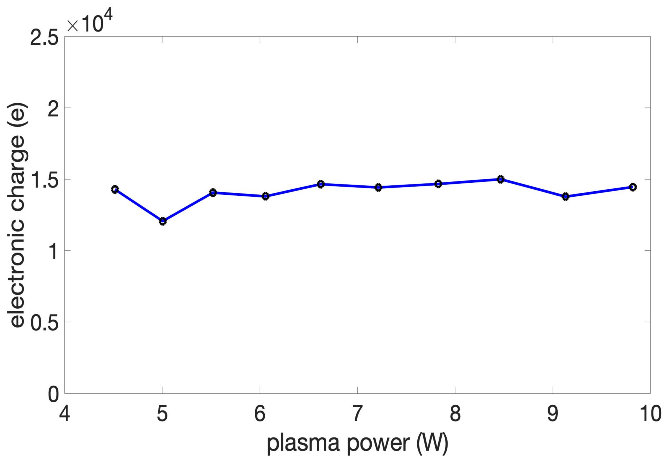

Figure 6.6: The charge of the dust particle calculated from Eq. 5.3 with the de-charging effect ignored.

Based on these measurement, the charge of the dust particle can be calculated by employing Eq. 5.3 and the results are shown in Fig. 6.6. Notice that in this calculation the de-charging effect is ignored for simplicity, i.e., $\xi = 1$ in Eq. 5.3. As shown in Fig. 6.6, the charge on the dust particle changes little with the increase of the plasma power. The averaged charge calculated at a plasma pressure of 40 mTorr is around $1.34 \times 10^4\ e^-$ with a fluctuation of less than 10%.

6.2 Validation of Charge Measuring Method

To validate the charge measured by this new method, the calculated charge is compared to the charge measured by a different method, the mode spectra method.

In the mode spectra method, a three-particle triangular structure needs to be formed in a single plane (single layer structure). As an example, Fig. 6.7 shows this single layer structure recorded from a top-view camera at a plasma pressure at 40 mTorr and a plasma power at 9.8 W.

Figure 6.7. Top-view of the three particles structure in a single layer.

There is one major difference between the single layer structure and the vertical chain structures, which is one focus of this dissertation: for vertical chain structures, due to the effect of the ion wake, there is a strong non-reciprocity in the particle-particle interactions, i.e., the upstream and downstream interaction are not symmetric. However, this non-reciprocal property of the particle-particle interaction becomes less important for dust particles in a single layer (particles levitate at the same height in the plasma sheath). Especially for a triangle structure in a single layer, the in-plane particle-particle interaction can be regarded as reciprocal due to the geometric symmetry of this structure. In this case, the theoretical normal modes can be derived as the eigen-modes of the dynamic matrix

$$M_{\alpha\beta,ij} = \frac{\partial^2 E}{\partial r_{\alpha,i} \partial r_{\beta,j}}, \tag{5.4}$$

where α, β are the coordinates subscripts (i.e., x and y coordinates) and i, j are subscripts indicating the particle. E is the total energy of the system and is defined as (considering an Yukawa type in-plane particle-particle interaction)

$$E = \frac{1}{2}\omega_{x0}^2 \sum_{i=1}^{N=3} x_i^2 + \frac{1}{2}\omega_{y0}^2 \sum_{i=1}^{N=3} y_i^2 + \frac{Q^2}{4\pi\epsilon_0} \sum_{j>i}^{N=3} \frac{1}{R_{ij}} e^{-\frac{R_{ij}}{\lambda_D}}, \tag{5.5}$$

where ω_{x0}, ω_{y0} are the in-plane restoring confinement in the x and y direction, respectively. Q is the charge of the dust particle, λ_D is the Debye length and R_{ij} is the inter-particle spacing between particles i and j.

The charge of the dust particle Q and the Debye length λ_D can be simultaneously determined by matching the theoretical mode spectra to the experimental one, which can be obtained from the top-view trajectories of the thermal motion of this three-particle structure in a manner similar to that described in chapter three. A match of the theoretical and experimental mode spectra is plotted in Fig. 6.8 where the red dots are the the theoretical normal modes and the yellow stripes are the experimentally measured mode spectra.

The charge of the dust particle is measured to be 1.22×10^4 e and the Debye length is measured to be 306 μm. The charge estimated from the new quick determination method differs by less than 9% from the charge measured from the traditional mode spectra method, which is acceptable considering the possible slight variance of the experimental conditions in these two sets of experiment.

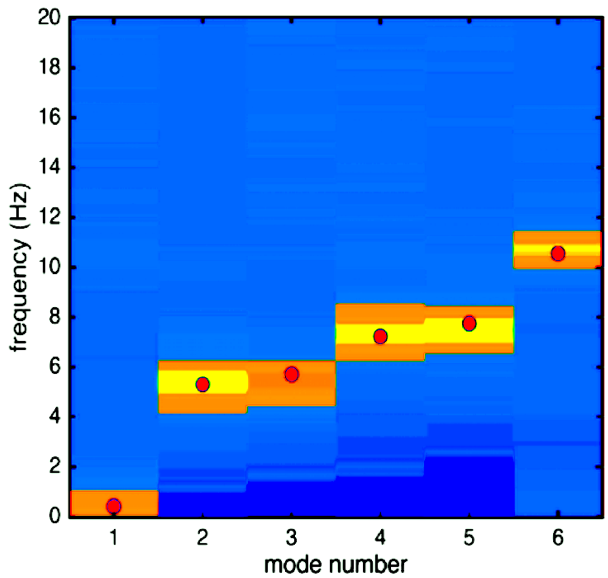

Figure 6.8: A match of the theoretical normal modes (red dots) to the experimental mode spectra (yellow stripes) using a dust charge of 1.22×10^4 e and a Debye length of 306 μm. The plasma pressure is 40 mTorr and the plasma power is 9.8 W.

CHAPTER SEVEN

Summary

In this dissertation, the grain-grain interaction were examined in the nonlinear regime by applying nonlinear amplitude-frequency response analysis.

In chapter one, a brief introduction of dusty plasmas was given, including the dust grain charging process, the formation and the properties of the plasma sheath, as well as the grain-grain interactions inside the plasma sheath.

In chapter two, the oscillation model for describing coupled dust pair motions with the consideration of non-reciporcal grain-grain interactions due to the existence of the ion wake was established. Also, a multiple-scale perturbation solution to the nonlinear coupled equations of motion is provided by first decoupling all the linear components.

In chapter three, the experiment equipment (the modified GEC reference cell) was introduced and all the details for measuring the nonlinear amplitude-frequency responses from the experiment were explained. Combined with the theoretical guidance derived from chapter two, the nonlinear part of the grain-grain interaction has been characterized.

In chapter four, the coupled oscillator model was extended to include all the horizontal degree of freedoms, and the corresponding multiple-scale perturbation solutions were derived. An nonlinear phenomenon, internal resonance, has been reported for the first time in dusty plasma, which is well explained by the extended theoretical model.

In chapter five, a noval machine-learning based framework for solving nonlinear amplitude-frequency response analysis in dusty plasma was proposed. The proposed Bayesian optimization framework can be applied to more general case of physics problems where physics quantities can be determined by optimizing simulations (especially computational expensive simulations) to the experimental results in an efficient manner.

In chapter six, a noval method to estimate the dust charge was proposed by measuring the levitation position changes for upstream dust particles with and without downstream particles. The estimation consists with the results measured from the mode spectrum method.

In the future, the current nonlinear repsonse analysis can be extended to fit a more general topological structure of dust particles (e.g., long chains, monolayers, crystal balls). This can be done by exploring the analytical solution to the corresponding dynamic equations of motion. To simplify the derivation of the analytical solution, a new coordinate basis that decouples the linear parts of the corresponding equations needs to be defined. In addition, the proposed machine learning framework of nonlinear response analysis in chapter five can be easily extended to investigate long particle chains. This will allow a measurement of the grain-grain interaction at different positions within the chain, which helps characterize the downstream ion wake.

[1] V.E. Fortov, A.V. Ivlev, S.A. Khrapak, A.G. Khrapak, and G.E. Morfill. Complex (dusty) plasmas: Current status, open issues, perspectives. *Physics Reports*, 421(1):1 – 103, 2005.

[2] K U Riemann. The bohm criterion and sheath formation. *Journal of Physics D: Applied Physics*, 24(4):493–518, apr 1991.

[3] Martin Lampe, Glenn Joyce, Gurudas Ganguli, and Valeriy Gavrishchaka. Interactions between dust grains in a dusty plasma. *Physics of Plasmas*, 7(10):3851–3861, 2000.

[4] Andre Melzer. Physics of dusty plasmas: an introduction. June 2019.

[5] H. Thomas, G. E. Morfill, V. Demmel, J. Goree, B. Feuerbacher, and D. Möhlmann. Plasma crystal: Coulomb crystallization in a dusty plasma. *Phys. Rev. Lett.*, 73:652–655, Aug 1994.

[6] J. H. Chu and Lin I. Direct observation of coulomb crystals and liquids in strongly coupled rf dusty plasmas. *Phys. Rev. Lett.*, 72:4009–4012, Jun 1994.

[7] Pierre de and Jacques Prost. The physics of liquid crystal. *Physics Today - PHYS TODAY*, 2, 01 1993.

[8] Gregor E. Morfill and Alexei V. Ivlev. Complex plasmas: An interdisciplinary research field. *Rev. Mod. Phys.*, 81:1353–1404, Oct 2009.

[9] Talbot L. Touryan K.J. Chung, P.M. Electric probes in stationary and flowing plasmas: theory and application. 1975.

[10] J E Allen. Probe theory - the orbital motion approach. *Physica Scripta*, 45(5):497–503, may 1992.

[11] J Goree. Charging of particles in a plasma. *Plasma Sources Science and Technology*, 3(3):400–406, aug 1994.

[12] MARTIN LAMPE. Limits of validity for orbital-motion-limited theory for a small floating collector. *Journal of Plasma Physics*, 65(3):171?180, 2001.

[13] M. Rosenberg and D. A. Mendis. Uv-induced coulomb crystallization in a dusty gas. *IEEE Transactions on Plasma Science*, 23(2):177–179, April 1995.

[14] M. Rosenberg, D. A. Mendis, and D. P. Sheehan. Uv-induced coulomb crystallization of dust grains in high-pressure gas. *IEEE Transactions on Plasma Science*, 24(6):1422–1430, Dec 1996.

[15] M. Rosenberg, D. A. Mendis, and D. P. Sheehan. Positively charged dust crystals induced by radiative heating. *IEEE Transactions on Plasma Science*, 27(1):239–242, Feb 1999.

[16] A. A. Sickafoose, J. E. Colwell, M. Horányi, and S. Robertson. Photoelectric charging of dust particles in vacuum. *Phys. Rev. Lett.*, 84:6034–6037, Jun 2000.

[17] Bob Walch, Mihály Horányi, and Scott Robertson. Charging of dust grains in plasma with energetic electrons. *Phys. Rev. Lett.*, 75:838–841, Jul 1995.

[18] Elden C Whipple. Potentials of surfaces in space. *Rep.Prog.Phys*, 44, Nov 1981.

[19] S. Guh M.S. Sodha. Physics of colloidal plasmas. *Advances in plasma physics*, 4, Nov 1971.

[20] D. Bohm and E. P. Gross. Theory of plasma oscillations. a. origin of medium-like behavior. *Phys. Rev.*, 75:1851–1864, Jun 1949.

[21] Pung Nien Hu and Sigi Ziering. Collisionless theory of a plasma sheath near an electrode. *The Physics of Fluids*, 9(11):2168–2179, 1966.

[22] W. J. Miloch, J. Trulsen, and H. L. Pécseli. Numerical studies of ion focusing behind macroscopic obstacles in a supersonic plasma flow. *Phys. Rev. E*, 77:056408, May 2008.

[23] Mitsuhiro Nambu, Sergey V. Vladimirov, and Padma K. Shukla. Attractive forces between charged particulates in plasmas. *Physics Letters A*, 203(1):40 – 42, 1995.

[24] V. A. Schweigert. Dielectric permittivity of a plasma in an external electric field. *Plasma Physics Reports*, 27(11):997–999, Nov 2001.

[25] A. V. Ivlev, S. K. Zhdanov, S. A. Khrapak, and G. E. Morfill. Kinetic approach for the ion drag force in a collisional plasma. *Phys. Rev. E*, 71:016405, Jan 2005.

[26] R. Kompaneets, U. Konopka, A. V. Ivlev, V. Tsytovich, and G. Morfill. Potential around a charged dust particle in a collisional sheath. *Physics of Plasmas*, 14(5):052108, 2007.

[27] V. A. Schweigert, I. V. Schweigert, A. Melzer, A. Homann, and A. Piel. Alignment and instability of dust crystals in plasmas. *Phys. Rev. E*, 54:4155–4166, Oct 1996.

[28] Jan Carstensen, Franko Greiner, Dietmar Block, Jan Schablinski, Wojciech J. Miloch, and Alexander Piel. Charging and coupling of a vertically aligned particle pair in the plasma sheath. *Physics of Plasmas*, 19(3):033702, 2012.

[29] Hendrik Jung, Franko Greiner, Oguz Han Asnaz, Jan Carstensen, and Alexander Piel. Exploring the wake of a dust particle by a continuously approaching test grain. *Physics of Plasmas*, 22(5):053702, 2015.

[30] Irving Langmuir. The interaction of electron and positive ion space charges in cathode sheaths. *Phys. Rev.*, 33:954–989, Jun 1929.

[31] Lewi Tonks and Irving Langmuir. A general theory of the plasma of an arc. *Phys. Rev.*, 34:876–922, Sep 1929.

[32] Lewi Tonks and Irving Langmuir. Oscillations in ionized gases. *Phys. Rev.*, 33:195–210, Feb 1929.

[33] E. B. Tomme, D. A. Law, B. M. Annaratone, and J. E. Allen. Parabolic plasma sheath potentials and their implications for the charge on levitated dust particles. *Phys. Rev. Lett.*, 85:2518–2521, Sep 2000.

[34] A. Melzer, V. A. Schweigert, I. V. Schweigert, A. Homann, S. Peters, and A. Piel. Structure and stability of the plasma crystal. *Phys. Rev. E*, 54:R46–R49, Jul 1996.

[35] V. A. Schweigert, I. V. Schweigert, A. Melzer, A. Homann, and A. Piel. Plasma crystal melting: A nonequilibrium phase transition. *Phys. Rev. Lett.*, 80:5345–5348, Jun 1998.

[36] A. Melzer, V. A. Schweigert, and A. Piel. Transition from attractive to repulsive forces between dust molecules in a plasma sheath. *Phys. Rev. Lett.*, 83:3194–3197, Oct 1999.

[37] A Melzer, V A Schweigert, and A Piel. Measurement of the wakefield attraction for “dust plasma molecules”. *Physica Scripta*, 61(4):494–501, apr 2000.

[38] A. A. Samarian, S. V. Vladimirov, and B. W. James. Dust particle alignments and confinement in a radio frequency sheath. *Physics of Plasmas*, 12(2):022103, 2005.

[39] A. V. Ivlev, R. Sütterlin, V. Steinberg, M. Zuzic, and G. Morfill. Nonlinear vertical oscillations of a particle in a sheath of a rf discharge. *Phys. Rev. Lett.*, 85:4060–4063, Nov 2000.

[40] C. Zafiu, A. Melzer, and A. Piel. Nonlinear resonances of particles in a dusty plasma sheath. *Phys. Rev. E*, 63:066403, May 2001.

[41] You-Nian Wang, Lu-Jing Hou, and Xiaogang Wang. Self-consistent nonlinear resonance and hysteresis of a charged microparticle in a rf sheath. *Phys. Rev. Lett.*, 89:155001, Sep 2002.

[42] Ali H Nayfeh and D. T. Mook. Nonlinear oscillations. *Nonlinear Oscillations*, 1979.

[43] Zhiyue Ding, Ke Qiao, Jie Kong, Lorin Matthews, and Truell Hyde. Nonlinear response of vertical paired structure in complex plasma. *Plasma Physics and Controlled Fusion*, 02 2019.

[44] J K Olthoff and K E Greenberg. *Journal of research of the National Institute of Standards and Technology*, 100(4):327–339, Jul-Aug 1995.

[45] P. J. Hargis, K. E. Greenberg, P. A. Miller, J. B. Gerardo, J. R. Torczynski, M. E. Riley, G. A. Hebner, J. R. Roberts, J. K. Olthoff, J. R. Whetstone, R. J. Van Brunt, M. A. Sobolewski, H. M. Anderson, M. P. Splichal, J. L. Mock, P. Bletzinger, A. Garscadden, R. A. Gottscho, G. Selwyn, M. Dalvie, J. E. Heidenreich, Jeffery W. Butterbaugh, M. L. Brake, M. L. Passow, J. Pender, A. Lujan, M. E. Elta, D. B. Graves, H. H. Sawin, M. J. Kushner, J. T. Verdeyen, R. Horwath, and T. R. Turner. The gaseous electronics conference radiofrequency reference cell: A defined parallelplate radiofrequency system for experimental and theoretical studies of plasmaprocessing discharges. *Review of Scientific Instruments*, 65(1):140–154, 1994.

[46] S. Nunomura, J. Goree, S. Hu, X. Wang, A. Bhattacharjee, and K. Avinash. Phonon spectrum in a plasma crystal. *Phys. Rev. Lett.*, 89:035001, Jun 2002.

[47] A. Melzer, M. Klindworth, and A. Piel. Normal modes of 2d finite clusters in complex plasmas. *Phys. Rev. Lett.*, 87:115002, Aug 2001.

[48] A. Melzer. Mode spectra of thermally excited two-dimensional dust coulomb clusters. *Phys. Rev. E*, 67:016411, Jan 2003.

[49] Yuriy Ivanov and André Melzer. Modes of three-dimensional dust crystals in dusty plasmas. *Phys. Rev. E*, 79:036402, Mar 2009.

[50] K Qiao, Z Ding, J Kong, M Chen, L. S Matthews, and T. W Hyde. Determination of interaction between a dust particle pair in complex plasmas. *arXiv*, 2017.

[51] Zhiyue Ding, Ke Qiao, Nicholas Ernst, Jie Kong, Mudi Chen, Lorin S Matthews, and Truell W Hyde. Nonlinear mode coupling and internal resonance observed in a dusty plasma. *New Journal of Physics*, 21(10):103051, oct 2019.

[52] F. Cottone, H. Vocca, and L. Gammaitoni. Nonlinear energy harvesting. *Phys. Rev. Lett.*, 102:080601, Feb 2009.

[53] J. Xu and J. Tang. Multi-directional energy harvesting by piezoelectric cantilever-pendulum with internal resonance. *Applied Physics Letters*, 107(21):213902, 2015.

[54] Liuyang Xiong, Lihua Tang, and Brian R. Mace. Internal resonance with commensurability induced by an auxiliary oscillator for broadband energy harvesting. *Applied Physics Letters*, 108(20):203901, 2016.

[55] Dario Antonio, Damián H. Zanette, and Daniel López. Frequency stabilization in nonlinear micromechanical oscillators. *Nature Communications*, 3:806 EP –, 05 2012.

[56] C. Samanta, P. R. Yasasvi Gangavarapu, and A. K. Naik. Nonlinear mode coupling and internal resonances in mos2 nanoelectromechanical system. *Applied Physics Letters*, 107(17):173110, 2015.

[57] Changyao Chen, Damián H. Zanette, David A. Czaplewski, Steven Shaw, and Daniel López. Direct observation of coherent energy transfer in nonlinear micromechanical oscillators. *Nature Communications*, 8:15523 EP, 05 2017.

[58] P. R. Sethna and A. K. Bajaj. Bifurcations in dynamical systems with internal resonance. *Journal of Applied Mechanics*, 45(4):895–902, 1978.

[59] M. Sayed and M. Kamel. 1:2 and 1:3 internal resonance active absorber for non-linear vibrating system. *Applied Mathematical Modelling*, 36(1):310 – 332, 2012.

[60] James S. Bergstra, Rémi Bardenet, Yoshua Bengio, and Balázs Kégl. Algorithms for hyper-parameter optimization. pages 2546–2554, 2011.

[61] Donald R. Jones, Matthias Schonlau, and William J. Welch. Efficient global optimization of expensive black-box functions. *Journal of Global Optimization*, 13(4):455–492, 1998.